國 立 中 央 大 學

大 氣 科 學 學 系

碩 士 論 文

應用四維變分資料同化系統探討 2022 年 TAHOPE IOP#1 期間長生命期準靜止中尺度對流系統之多重尺度影響

On the Multi-Scale Factors Contributing to the Evolution of a Long-Lived Quasi-Stationary Mesoscale Convective System During the 2022 TAHOPE IOP#1 Revealed by a 4DVar Data Assimilation System

研 究 生：黃皓宇 (Hao-Yu Huang)

指導教授：廖宇慶 博士 (Dr. Yu-Chieng Liou)

中 華 民 國　　一一四　　年　　九　　月

國立中央大學圖書館學位論文授權書

填單日期：2025 / 9 / 17　　2025.9 版

授權人姓名	黃皓宇	學 號	112621005
系所名稱	大氣科學系大氣物理所碩士班	學位類別	☑碩士 □博士
論文名稱	應用四維變分資料同化系統探討 2022 年 TAHOPE IOP#1 期間長生命期準靜止中尺度對流系統之多重尺度影響	指導教授	廖宇慶

學位論文網路公開授權

本人同意學位論文全文電子檔公開方式如下：

・在「國立中央大學圖書館博碩士論文系統」.

(✓)同意立即網路公開

(　)同意 於西元＿＿＿年＿＿＿月＿＿＿日網路公開

・在國家圖書館「臺灣博碩士論文知識加值系統」

(✓)同意立即網路公開

(　)同意 於西元＿＿＿年＿＿＿月＿＿＿日網路公開

依著作權法規定，非專屬、無償授權國立中央大學、台灣聯合大學系統與國家圖書館，不限地域、時間與次數，以文件、錄影帶、錄音帶、光碟、微縮、數位化或其他方式將上列授權標的基於非營利目的進行重製。

學位論文紙本延後公開申請 (紙本學位論文立即公開者此欄免填)

本人撰寫之學位論文紙本因以下原因將延後公開

・延後原因

(　)已申請專利並檢附證明，專利申請案號：

(　)涉國家機密

(　)依法不得提供，請說明：＿＿＿＿＿＿＿＿

・公開日期：西元＿＿＿＿年＿＿＿＿月＿＿＿＿日

※繳交教務處註冊組之紙本論文(送繳國家圖書館)若不立即公開，請加填「國家圖書館學位論文延後公開申請書」

研究生簽名：黃皓宇　　指導教授簽名：廖宇慶

*本授權書請完整填寫並親筆簽名後，裝訂於論文封面之次頁。

國立中央大學碩士班研究生
論 文 指 導 教 授 推 薦 書

大氣科學學系大氣物理碩士班 學系/研究所 黃皓宇 研究生
所提之論文 應用四維變分資料同化系統探討2022年TAHOPE IOP#1期間長生命期準靜止中尺度對流系統之多重尺度影響
係由本人指導撰述，同意提付審查。

指導教授 廖宇慶 (簽章)

114 年 7 月 2 日

1140702

國立中央大學碩士班研究生
論文口試委員審定書

大氣科學學系大氣物理碩士班 學系/研究所 黃皓宇 研究生所提之論文 應用四維變分資料同化系統探討2022年TAHOPE IOP#1期間長生命期準靜止中尺度對流系統之多重尺度影響 經由委員會審議，認定符合碩士資格標準。

學位考試委員會召集人 楊明仁

委　　員 廖宇慶

王重傑

鍾高陞

中　華　民　國　114 年　7 月　2 日

1140702

Chinese abstract

每年 5 月底至 6 月，臺灣經常受到滯留的梅雨鋒面影響，有利於大雨事件發生。臺灣區域豪雨觀測與預報實驗（TAHOPE）於 2022 年 5 月至 8 月期間進行，旨在提升對極端降雨事件的瞭解與預報能力。本研究使用快速更新的四維變分分析系統（IBM_VDRAS）探討於 TAHOPE 第一次密集觀測期間（IOP#1），2022 年 5 月 26 日造成臺灣中部數小時極端降雨的中尺度對流系統（MCS）。透過同化臺灣西部七部雷達的觀測資料，該系統產生了高時空解析度的分析場，幾乎涵蓋整個 MCS 事件。當梅雨鋒面位於臺灣北方海面上，伴隨鋒前臺灣中部上空強勁的低層噴流（LLJ）輸送豐沛水氣，促使 MCS 持續發展與增強。隨著西南氣流減弱與水氣減少，梅雨鋒面逐步南移至臺灣上空，局地條件轉趨不利，導致 MCS 向南移動並規模縮小。此長時間 MCS 事件中，對流胞多次在不同但相近的上游位置被觸發，向下游傳播並與先前的對流胞合併，呈現典型的後造型對流特徵。本研究進一步探討影響 MCS 的多重尺度因素。結果顯示，西南氣流受南部山脈阻擋產生向北的水平氣壓梯度力，驅動低層噴流（LLJ）。此外，北邊的梅雨鋒面與東邊的地形阻擋 MCS 的移動，使之長時間滯留在中部地區。

English abstract

From late May to June, Taiwan is frequently affected by the quasi-stationary Mei-Yu front, which provides favorable conditions for torrential rainfall. The Taiwan-Area Heavy Rain Observation and Prediction Experiment (TAHOPE) was conducted from May to August 2022 to enhance the understanding and forecasting of extreme rainfall events in Taiwan. A mesoscale convective system (MCS) was investigated, which produced extreme rainfall over central Taiwan (CT) for several hours on 26 May during Intensive Observation Period #1 (IOP#1) of the TAHOPE, using a rapid-update 4DVar analysis system (IBM_VDRAS). High-spatiotemporal analysis fields were generated by assimilating observed data from seven radars across western Taiwan, covering the entire MCS event. When the Mei-Yu front was positioned to the north and a strong southwesterly low-level jet (LLJ) over CT transported abundant moisture, it was supportive for the widespread convective development and sustaining the MCS. As the southwesterly flow weakened with reduced moisture, the Mei-Yu front began moving southward and the local conditions became unfavorable, thereby shifting the MCS southward and causing it to become smaller in scale. Several convective cells were repeatedly triggered at nearby upstream locations, propagated downstream over the same area, and merged with preceding ones downstream, suggesting a back-building system. Multi-scale factors influencing the MCS are further examined. Our results reveal that the LLJ was driven by a local northward horizontal pressure gradient force generated as the southwesterly flow impinged upon the southern mountain range. Meanwhile, the MCS was blocked by both the Mei-Yu front to the north and the mountainous terrain to the east, causing it to remain quasi-stationary over CT for an extended period.

Acknowledgements

從大學一路讀到碩士，我在中央大學的求學旅程已邁入第六年。猶記得大學入學前的暑假，打工空檔中常常思索著大學生活會是什麼模樣，心中交織著對未知的恐懼與對未來的憧憬與期待。

四年的大學生涯豐富了我的人生經歷。這段時間不僅讓我累積了書本知識，更學會了許多人生智慧。大三暑假期間，我申請參加中央氣象局的暑期實習，透過實習的經驗，更加確定自己想深入鑽研大氣領域的專業知識，特別是在資料同化這一領域。大四時，順利加入廖宇慶老師的研究團隊，開始投入四維變分資料同化系統的研究。

碩士班與大學部生活最大的不同，在於前者的核心是「研究」。身為研究生，如何獨立解決科學問題成為重要課題。廖老師嚴謹務實的指導，重視我們對研究問題的思辨能力與自主解決問題的歷程，並在適當的時機給予關鍵性的引導，使我始終朝著正確方向前進。找尋答案的過程往往需要極大的耐心，有時也伴隨著挫折與困難。碩一時，我剛學會使用 RAKIT 工具對雷達資料進行品質控制（QC）。在處理 S-POL 資料時，一開始進展順利，結果令人滿意，但當進入 TEAM-R 資料的 QC 時，卻發現 RAKIT 無法有效處理該資料。前後一個多月的時間，最終才得到較好的結果。碩一下，為了提升 IBM_VDRAS 中雨水混合比的表現，花了近兩個月不斷嘗試調整各項設定，甚至寄信向系統原作者請教，最終改用適合台灣地區的 Z/KDP-Qr 關係式，才有明顯改善表現。

誠摯感謝擔任本次口試委員的楊明仁老師、鍾高陞老師，以及王重傑老師的不吝指教，所給予的寶貴建議讓我的論文更加完整與充實。感謝碩士班期間曾經指導與協助我的所有師長及學長姊，雷達實驗室的同屆的夥伴們， Ruel、覃廉翔、楊世楷、林芸安、蘇琦竣，以及吳倚彤，感謝兩年的陪伴與支持。感謝小那學姊在碩班這兩年幫忙每一次的參訪、實驗室活動以及許多的行政事務；感謝 Haidy 學姊在我研究初期，耐心教導雷達資料品質控制與訊號雜訊比（SNR）處理方法；也謝謝廖老師實驗室的柏謙、詠霖、子睿、孟杰學長，以及佳靜學姊，在研究過程中提供我許多寶貴的建議與鼓勵，使我能持續向前；感謝同屆的碩士班同學們，彼此扶持、共同努力，還規畫多次的旅行，在研

究的路上增添許多溫暖與動力；感謝雷達實驗室的張偉裕老師和鍾高陞老師，每一次報告完都不吝指教，給予我很多的建議和指導。特別感謝我的指導老師——廖宇慶老師，這兩年來不僅在研究上給予我空間與引導，也在人生方向上予我深刻的啟發與支持，讓我在碩士生涯中受益良多。感謝我的家人們，始終尊重我的選擇，從未設限我的人生道路，並在背後默默支持與陪伴，讓我無後顧之憂地走過每一段旅程。最後，感謝所有在我生命中出現、陪伴我走過低潮的好朋友們，特別感謝這兩年庭愷、心靖、致龍、孝儒、家甄，以及允龍，在我迷惘或疲憊之際，總能適時地給予鼓勵與力量，是你們的存在讓我有勇氣面對每一個挑戰。

最後，願以《聖經》中的一句我深愛的話語，為這段碩士旅程畫下句點：

「Those who sow in tears will reap with songs of joy.」流淚撒種的，必歡呼收割。

Table of contents

List of tables

List of figures

Chapter 1 Introduction

During Mei-Yu season (typically spanning from May to June), Taiwan frequently experiences the passage of Mei-Yu frontal systems (Kuo and Chen, 1990; Wang et al., 2022). These systems (termed the Baiu front in Japan and the Changma front in Korea) form along the boundary where the maritime Tropical (mT) warm air mass extends westward and interacts with the weakening continental Polar (cP) air mass over East Asia. These frontal boundaries initially form in southern China in May and subsequently migrate northward gradually with the seasonal intensification of the mT warm air mass, sequentially impacting the weather patterns across Taiwan, Korea, and Japan (Kuo and Chen, 1990; Yang et al., 2024).

As the Mei-Yu frontal systems, which typically initiate with a low-pressure system over the southern vicinity of China, extend eastward across the Taiwan Strait, and terminate with another low-pressure system near southern Japan (visible on surface weather maps), approach Taiwan, a significant subset exhibits retarded progression and may remain quasi-stationary for a couple of days over the island (Kuo and Chen, 1990; Ke et al., 2019). Taiwan is frequently influenced by low-level jets (LLJs) during this quasi-stationary front period (Tai-Jen Chen and Yu, 1988; Chen et al., 1994; Chen et al., 1997; Chen et al., 2005; Tu et al., 2019; Tu et al., 2022). According to Chen et al. (2022), LLJs can be categorized into three types: the synoptic-system-related low-level jets (SLLJs), marine boundary layer jets (MBLJs), and the barrier jets (BJs). Specifically, the SLLJs are positioned at the 700 to 850 hPa levels southeast of a Mei-Yu frontal cyclone along the large-scale Mei-Yu trough; the MBLJs, associated with the southwesterly monsoonal flow over the northern part of the South China Sea, are located at approximately 925 hPa level; and the BJs are situated at roughly 1-km height above the surface, with maximum wind speed of approximately 14 ms^{-1} at about 1 km. Notably, all these LLJs could co-exist over Taiwan and play a pronounced role in low-level moisture transport, thereby leading to a

high probability of heavy rainfall event occurrence.

Over Taiwan during the Mei-Yu season, mesoscale convective systems (MCSs) often develop under the interplay of multi-scale factors, including monsoonal southwesterly flow, Mei-Yu fronts, LLJs, complex topography of Taiwan, and convection (Wang et al., 2016; Ke et al., 2019; Yang et al., 2024). Some MCSs demonstrate long-lived lifespans and produce torrential precipitation, thereby contributing to high-impact weather events. In particular, the interplay of ample low-level moist warm air transported by LLJs, and the convergence embedded within the Mei-Yu fronts and generated on windwards of mountains establishes a conducive environment for the initiation and sustenance of heavy-rainfall-producing MCSs. Nevertheless, owing to highly variable nature of these complicated interactions and intricate orographic effects, accurately forecasting the initiation, propagation, and rainfall distribution of the MCSs remains significantly challenging.

Compared to isolated or scattered convective cells, organized MCSs, particularly linear types, are capable of producing heavy rainfall and causing flash flooding (Houze et al., 1990; Doswell et al., 1996). Parker and Johnson (2000, 2004) analyzed and classified linear MCSs from the central plains in the United States into three types, involving the trailing (TS), leading (LS), and parallel (PS) stratiform precipitation. Among these types, the TS was found to be the dominant mode for linear MCSs. Beyond these linear MCSs, high-impact back-building MCSs have received considerable attention due to their capacity to produce extreme and prolonged precipitation over a localized region. When such systems impact populated areas, intense and persistent precipitation can result in hazardous consequences. Schumacher and Johnson (2005) highlighted that that back-building MCSs rely more on mesoscale and storm-scale processes than on large-scale ones. They often initiate along the mesoscale boundaries and appear to be sustained by storm-generated outflows. These systems are characterized by repeatedly triggered new convective cells that form upstream at nearly the same location and subsequently propagate

downstream over the same area. As dissipating convective cells advance downstream, they are replaced by the new cells reaching maturity. This process is referred to as echo training, creating a nearly stationary high-reflectivity area on radar and this quasi-stationary behavior can be explained as the result of a cancellation between propagation and cell motion vectors, as indicated by Chappell (1986).

Although cold pools are generally considered crucial for organizing and maintaining linear convective systems, previous studies have demonstrated that some back-building MCSs develop in environments with abundant low-level moisture, which tends to inhibit the formation of strong cold pools. This phenomenon suggests that alternative mechanisms may contribute to the initiation and maintenance of the back-building process in the absence of robust cold pools (Schumacher and Johnson, 2008; Schumacher, 2009; Schumacher and Johnson, 2009; Wang et al., 2016; Ito et al., 2021). Schumacher and Johnson (2008) examined a quasi-stationary back-building MCS that developed near a preexisting mesoscale convective vortex (MCV) within a moist environment characterized by a strong low-level jet, with no discernible surface boundary present prior to convection initiation. They found that the quasi-linear convective line, characterized by convective cells continuously propagating eastward, was formed by the low-level gravity waves rather than the cold pools. Additionally, the quasi-stationary nature of the MCS resulted from the cancellation between southward-propagating gravity waves and the strong southerly flow. These findings suggest that the formation and development of back-building MCSs can occur through diverse and complex physical mechanisms.

When the back-building MCSs form during the Mei-Yu season near Taiwan, the synoptic conditions are typically favorable for convective development. However, the extent to which localized factors, including convergence zones, pre-frontal LLJs with abundant moisture, and terrain influences, contribute to the formation of the back-building MCSs remains a critical question. These localized characteristics pose significant challenges for accurately predicting

such systems using numerical weather models, especially in regions with complex topography such as Taiwan. Therefore, to improve the understanding and enhance the predictability of mesoscale severe weather events associated with Mei-Yu fronts and typhoons, Taiwan-Area Heavy rain Observation and Prediction Experiment (TAHOPE) observation field campaign was conducted during late May to mid-August in 2022, providing comprehensive information through multiple observation platforms. This campaign aimed to investigate large-scale environment impacts, mesoscale convective systems, and microscale physical processes. During the TAHOPE, a total of 11 Intensive Observation Periods (IOPs) and 8 Special Observation Periods (SOPs) were conducted. These observational periods targeted the rainfall events associated with Mei-Yu fronts, typhoons, low-pressure systems, tropical depressions, as well as afternoon thunderstorms.

Over the past few decades, substantial efforts have been made to improve numerical weather model simulations and forecasts. Among these, data assimilation has emerged as a key technique for enhancing the quality of numerical weather prediction by optimally integrating observations into model initial conditions, thereby enabling more accurate forecasts of atmospheric states. The Variational Doppler Radar Analysis System (VDRAS) was originally developed at National Center for Atmospheric Research (Sun and Crook, 1997, 1998). Through assimilating observations into VDRAS using 4DVar data assimilation method, VDRAS is capable of producing high spatiotemporal-resolution analysis fields. This analysis system has been widely applied in various studies to investigate mesoscale and storm-scale processes (Crook and Sun, 2002, 2004; Sun, 2005; Sun and Zhang, 2008; Tai et al., 2011; Zhang, F. et al., 2021; Zhang, L. et al., 2021; Wu et al., 2021; Xiao et al., 2022; Sun et al., 2023). The version of VDRAS used in this study incorporates a simple ice-phase microphysical scheme (Chang et al., 2016) and terrain-resolving capability (Tai et al., 2017). This enhanced version is hereafter referred to as IBM_VDRAS.

Using the convection-allowing terrain-resolving IBM_VDRAS that assimilated observed radar data, a quasi-stationary back-building MCS that occurred during IOP #1 of the TAHOPE was investigated in this study. This MCS produced significant rainfall in central Taiwan, with 8-hour accumulated precipitation reaching up to 246 mm, marking a high-impact weather event. Given that the well-known challenges in accurately predicting such MCSs, this study leverages the high spatiotemporal-resolution IBM_VDRAS to examine the physical mechanisms driving the upstream development and maintenance of this long-lived MCS under complex multi-scale interactions, with a particular focus on the roles of the Mei-Yu front, LLJs, and terrain. Based on our findings, we aim to provide insights that may help improve the prediction of such MCSs in the future.

The remainder of this manuscript is organized as follows. Chapter 2 provides a brief introduction to IBM_VDRAS system. Chapter 3 describes the data used in this study, the configuration of IBM_VDRAS, and the validation of the analysis fields against observations. Chapter 4 presents an overview of the rainfall event and analyzes the rainfall event using the analysis fields from IBM_VDRAS, and further investigates the key factors influencing the rainfall event, including the local conditions over central Taiwan and the LLJs. A sensitivity experiment is conducted to examine the impact of terrain on the near-surface front, the LLJs, and ultimately the rainfall forecast. Chapter 5 summarizes the main findings with the aid of a simplified conceptual model, concludes the study, and suggests directions for future research.

Chapter 2 Description of IBM_VDRAS

Since the IBM_VDRAS has been successfully applied in many previous studies, this chapter is to give a description of this 4DVar analysis system, including the cloud-resolving forward integration model, the physical process implemented in cloud-resolving model, the cost function representing the misfits between the observations and the model forecasts, and the IBM method.

2.1 Cloud-resolving model

In IBM_VDRAS, the cloud-resolving model incorporates six prognostic equations (Sun and Crook, 1997, 1998), consisting of the 3-dimensoinal momentum equations, the thermodynamic equation, the rainwater equation, and the total water equation. The momentum equations, along with the mass continuity equation, are based on the anelastic approximation, which are expressed as follows:

$$\frac{d\bar{\rho}u}{dt} = -\frac{\partial p'}{\partial x} + \nu\nabla^2\bar{\rho}u \qquad (2.1)$$

$$\frac{d\bar{\rho}v}{dt} = -\frac{\partial p'}{\partial y} + \nu\nabla^2\bar{\rho}v \qquad (2.2)$$

$$\frac{d\bar{\rho}w}{dt} = -\frac{\partial p'}{\partial z} + \mathrm{g}\bar{\rho}\left(\frac{T'}{T} + 0.61q_v{}' - q_c - q_r\right) + \nu\nabla^2\bar{\rho}w \qquad (2.3)$$

$$\frac{\partial\bar{\rho}u}{\partial x} + \frac{\partial\bar{\rho}v}{\partial y} + \frac{\partial\bar{\rho}w}{\partial z} = 0, \qquad (2.4)$$

where u, v, and w are the 3-D wind components ($\mathrm{m\,s^{-1}}$), q_v ($\mathrm{g\,kg^{-1}}$), q_c ($\mathrm{g\,kg^{-1}}$), and q_r ($\mathrm{g\,kg^{-1}}$) are the mixing ratios for water vapor, cloud water vapor, and rain water, respectively; T, ρ ($\mathrm{kg\,m^{-3}}$), and p are the temperature, the density of air, and the pressure, respectively. The primed variables denote the perturbations from the initial unperturbed state and the unperturbed variables are represented with overbars. The quantity ν is the eddy viscosity. By differentiating Eq. (2.1) with respect to the x-direction, Eq. (2.2) with respect to

the y-direction, and Eq. (2.3) with respect to the z-direction, and subsequently substituting these results into Eq. (2.4), the diagnostic equation is derived for perturbation pressure:

$$\nabla^2 p' = -\boldsymbol{\nabla} \cdot \left(\vec{\boldsymbol{V}} \cdot \boldsymbol{\nabla} \bar{\rho} \vec{\boldsymbol{V}}\right) + \mathrm{g}\bar{\rho} \frac{\partial}{\partial z}\left(\frac{T'}{T} + 0.61 q_v{}' - q_c - q_r\right). \quad (2.5)$$

The thermodynamic equation is written regarding liquid water potential temperature, θ_l, as:

$$\frac{d\bar{\rho}\theta_l}{dt} = -\frac{L_v \bar{\rho}}{c_p T}\frac{{\theta_l}^2}{\theta}\frac{dV_{TM} q_r}{dz} + \kappa \nabla^2 \bar{\rho}\theta_l, \quad (2.6)$$

where V_{TM} (m s^{-1}) is the mass-weighted terminal velocity, κ (m^2 s^{-1}) is the diffusivity of liquid water potential temperature, and L_v (2.5×10^6 J kg^{-1}) is the latent heat of vaporization. The liquid water potential temperature is conserved in terms of condensation and evaporation, which is defined by

$$\theta_l = \theta\left[1 - \frac{L_v}{c_p T}(q_c + q_r)\right]. \quad (2.7)$$

The prognostic equations with regard to rainwater mixing ratio q_r and total water mixing ratio q_t are written as:

$$\frac{d\bar{\rho} q_r}{dt} = \bar{\rho} R_a + \bar{\rho} R_c + \bar{\rho} R_e + \bar{\rho}\frac{dV_{TM} q_r}{dz} + \kappa \nabla^2 \bar{\rho} q_r \quad (2.8)$$

$$\frac{d\bar{\rho} q_t}{dt} = \bar{\rho}\frac{dV_{TM} q_r}{dz} + \kappa \nabla^2 \bar{\rho} q_t, \quad (2.9)$$

where R_a (g kg^{-1} s^{-1}) is the transfer rate from cloud water to rainwater due to autoconversion, R_c (g kg^{-1} s^{-1}) is the transfer rate from cloud water to rainwater due to accretion, and R_e (g kg^{-1} s^{-1}) is the evaporation rate that raindrops become water vapor. The physical processes are discussed in more detail later. The total water is defined by

$$q_t = \begin{cases} q_c + q_{vs} + q_r, & \text{if } (q_v \geq q_{vs}) \\ q_v + q_r, & \text{if } (q_v < q_{vs}). \end{cases} \quad (2.10)$$

Assuming that all water vapor in excess of the saturation value is converted to cloud water, the temperature and cloud water mixing ratio q_{vs} (g kg^{-1}) are diagnosed from the prognostic variables as follows:

$$T = \left(\frac{p}{p_0}\right)^{R/c_p} \theta_l \left[1 + \frac{L_v}{c_p T}(q_c + q_r)\right] \quad (2.11)$$

$$q_c = \begin{cases} q_t - q_{vs} - q_r, & \text{if } (q_v \geq q_{vs}) \\ 0, & \text{if } (q_v < q_{vs}), \end{cases} \quad (2.12)$$

where q_{vs} is the saturation mixing ratio, obtained by

$$q_{vs} = \frac{3.8}{p} exp\left(17.27 \frac{T-273.16}{T-35.86}\right). \quad (2.13)$$

The Newton–Raphson method is employed to obtain the temperature from Eqs. (2.11) to (2.13), for enhancing the computational efficiency (Lo, 2019).

2.2 Physical processes

The warm-rain physical processes included in the model are the condensation and evaporation of cloud water (implicit in θ_l), autoconversion of cloud to rain, accretion of cloud by rain, evaporation of raindrops in subsaturated air, and sedimentation of rain. These processes are parameterized following Kessler (1969) and Miller and Pearce (1974) as:

$$R_a = \begin{cases} \alpha(q_c - q_{crit}), & \text{if } (q_c < q_{crit}) \\ 0, & \text{if } (q_c > q_{crit}) \end{cases} \quad (2.14)$$

$$R_e = \beta(q_v - q_{vs})(\rho q_r)^{0.65} \quad (2.15)$$

$$R_c = \gamma q_c {q_r}^{0.95}. \quad (2.16)$$

The coefficients α, β, and γ are set to 0.001 s^{-1}, 0.0486 s^{-1}, and 0.002 s^{-1}, respectively. The criteria q_{crit} is set to 1.5 g kg^{-1}. The mass-weighted terminal velocity of rainwater, based on a Marshall-Palmer drop-size distribution, is used to calculate sedimentation and expressed as follows:

$$V_{TM} = 5.4\left(\frac{p_0}{\bar{p}}\right)^{0.4} (\bar{\rho} q_r)^{0.125}, \quad (2.17)$$

where p_0 is the pressure at the ground and $\bar{p}$ is the basic-state pressure. The sedimentation is given by

$$R_s = \bar{\rho} \frac{dV_{TM} q_r}{dz}. \quad (2.18)$$

In addition to the warm-rain process described above, the latest version incorporates an cold-rain process including snow and ice, the details of which are provided in Chang et al. (2016).

2.3 Cost function

The four-dimensional variational data assimilation (4DVar) method is employed in IBM_VDRAS to obtain the optimal initial conditions, ensuring the model integration best matches the observations. The cost function is used to represent the misfit between the model prediction and the observations, given by

$$J = (\boldsymbol{x_0} - \boldsymbol{x_b})^T \boldsymbol{B}^{-1} (\boldsymbol{x_0} - \boldsymbol{x_b}) + \sum_{\sigma,\tau,i} \left[\eta_v \left(V_{r,i} - V_{r,i}^{obs} \right)^2 + \eta_q \left(q_{r,i} - q_{r,i}^{obs} \right)^2 \right] + J_{mb} + J_p. \quad (2.19)$$

Here, $\boldsymbol{x_0}$ represents the model variables at the initial time within an assimilation cycle, $\boldsymbol{x_b}$ denotes the background field, and $\boldsymbol{B}$ is background error covariance matrix. σ, τ, and i correspond to the spatial domain, temporal domain, and the i-th radar, respectively. η_v and η_q are the weighting coefficients. The second term on the right-hand side of Eq. (2.19) demonstrates the misfit between the radial wind ($V_{r,i}$) and rainwater mixing ratio ($q_{r,i}$) predicted by the model, and the corresponding observations ($V_{r,i}^{obs}$ and $q_{r,i}^{obs}$) from radars.

The third term on the right-hand side, J_{mb}, represents the mesoscale background term, which means that the data-void regions are constrained toward mesoscale background. The final term, J_p, is the penalty term, which incorporates spatial and temporal smoothness constraints. This term helps to stabilize the model integration both spatially and temporally and facilitates faster convergence of the cost function.

The model-predicted radial velocity $V_{r,i}$ is calculated projecting the model-generated Cartesian velocity components (u, v, w) to radial direction of the radar, given by

$$V_{r,i} = u \frac{x - x_i}{r_i} + v \frac{y - y_i}{r_i} + (w - V_{TM}) \frac{z - z_i}{r_i}, \quad (2.20)$$

where r_i stands for the distance between the location of the radar (x_i, y_i, z_i) and a model grid point (x, y, z).

The observed $q_{r,i}^{obs}$ is estimated from observed radar dual-polarized parameters. The

original q_r-Z (reflectivity) relation used in IBM_VDRAS is given by

$$\rho q_r = 10^{(Z-43.1)/17.5}, \tag{2.21}$$

where ρ represents the air density ($\mathrm{kg\,m^{-3}}$), and ρq_r denotes the liquid water content ($\mathrm{g\,m^{-3}}$). Since Eq. (2.21) is derived based on the assumption of Marshall–Palmer drop size distribution (DSD), it cannot accurately represent the local relation in Taiwan. According to Chen et al. (2017), the combination of specific differential phase (KDP; unit: $°/km$) and reflectivity (Z; unit: dBZ) provides more accurate rainfall estimation than using reflectivity alone in northern Taiwan. In addition, the q_r serves as a key indicator of rainfall intensity, with higher q_r values generally associated with a greater likelihood of heavy rainfall. Therefore, we adopted this approach to improve the estimation of $q_{r,i}^{obs}$ in this study, DSDs from the NCU Joss–Waldvogel disdrometer (JWD) marked in Fig. 3.2, collected from 2005 to 2015, were utilized to perform T-matrix simulations to derive the relations between the dual-pol parameters

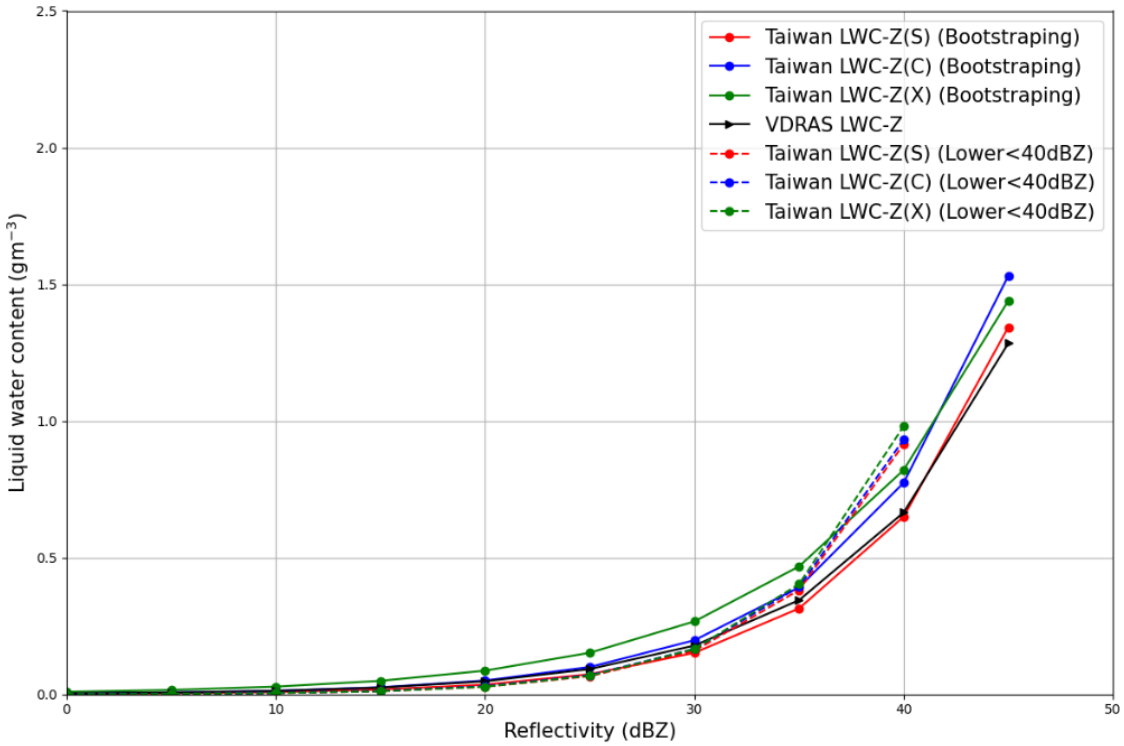

Figure 2.1. Relations between liquid water content (ρq_r) and reflectivity (Z). Solid lines with circular dots represent the q_r-Z relations using all reflectivity data to fit, while dashed lines represent those using reflectivity data below 40 dBZ to fit. Red, blue, and green lines correspond to the S-, C-, and X-band wavelengths, respectively. Black line indicates the original q_r-Z relation used in IBM_VDRAS.

and q_r, under the assumptions of a temperature of 20°C in pure rain and an elevation angle of 20°, for S-, C-, and X-band radars. It should be noted that this work was conducted by one of my laboratory colleagues. As a result, the rainwater mixing ratio can be estimated using the radar-observed Z or KDP, depending on the radar's wavelength (S-, C-, and X-band). The derived relations are given in Eqs. (2.22) to (2.30) and discussed in detail in the following paragraph.

Since KDP data tends to be noisy in regions of low reflectivity, the q_r-KDP relations are only applied when Z exceeds 40 dBZ. In addition, two q_r-Z relations are derived: Eqs. (2.22) to (2.24) are based on all radar-observed reflectivity using the Bootstrapping fitting method to mitigate uneven data distribution, and Eqs. (2.28) to (2.30) are based solely on radar-observed reflectivity values below 40 dBZ to fit and only used in conjunction with the implementation of the q_r-KDP relations. The comparison between locally derived q_r-Z relations and original q_r-Z relation is shown in Fig. 2.1. When the reflectivity is below 30 dBZ, the liquid water content estimated from the locally derived relations is generally closer to that from original relation, except for Eq. (2.23). For reflectivity between 30 and 40 dBZ, the liquid water content estimated from the locally derived relations is higher than that from original relation, except for Eq. (2.22). When the reflectivity exceeds 40 dBZ, all the liquid water content estimated from the locally derived relations are greater than those from original relation. As a result, the original relation underestimates the rainwater mixing ratio retrieved from reflectivity in Taiwan.

If the radar data quality is insufficient for reliable KDP usage, q_r is estimated using Z alone, which is expressed as the following formulas:

$$S-band: \rho q_r = 10^{(Z-42.97)/15.85} \quad (2.22)$$

$$C-band: \rho q_r = 10^{(Z-41.88)/16.88} \quad (2.23)$$

$$X-band: \rho q_r = 10^{(Z-41.76)/20.49}. \quad (2.24)$$

When high-quality KDP data are available, the choice of formula depends on the reflectivity

threshold:

1) If Z $\geq$ 40 dBZ:

i. If KDP $\geq$ 0 $°/km$, the following power-law relations are used:

$$S-band: \rho q_r = 1.8077 KDP^{0.64435} \quad (2.25)$$

$$C-band: \rho q_r = 1.1453 KDP^{0.6333} \quad (2.26)$$

$$X-band: \rho q_r = 0.81727 KDP^{0.65991}. \quad (2.27)$$

ii. If KDP $<$ 0 $°/km$, q_r is calculated using Eqs. (2.22) to (2.24).

2) If Z $<$ 40 dBZ, an alternative Z-based relation, derived from radar-observed reflectivity values below 40 dBZ, is used.:

$$S-band: \rho q_r = 10^{(Z-40.51)/13.17} \quad (2.28)$$

$$C-band: \rho q_r = 10^{(Z-40.41)/13.35} \quad (2.29)$$

$$X-band: \rho q_r = 10^{(Z-40.11)/12.95}. \quad (2.30)$$

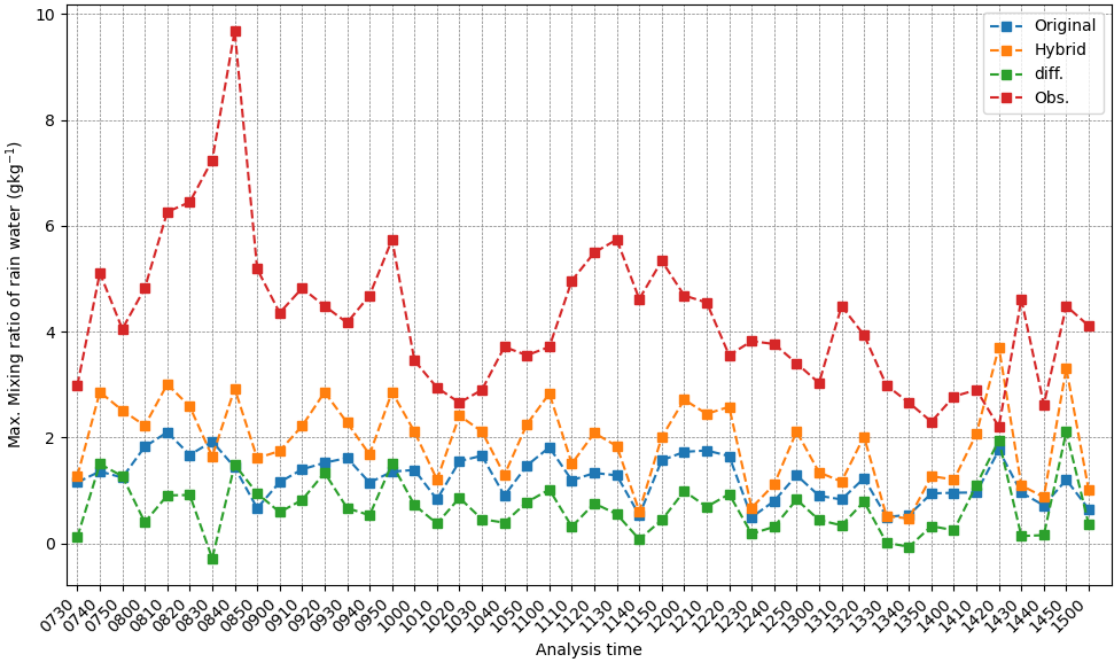

Figure 2.2. Three-dimensional maximum rainwater mixing ratio values at each analysis time. Red line denotes estimation based on Eq. (2.22) using the observed maximum mosaic reflectivity from QPESUMS provided by Central Weather Administration (CWA). Hybrid estimation scheme (orange lines), original estimation scheme (blue lines), and their differences (green lines).

Therefore, the Eqs. (2.22) to (2.30) constitute a hybrid approach for rainwater mixing ratio

estimation, whereas Equation (2.21) represents the original rainwater mixing ratio estimation method. Both methods had been implemented in IBM_VDRAS to evaluate whether the hybrid estimation scheme yielded higher rainwater mixing ratio values following data assimilation compared to the original method. The sole difference of IBM_VDRAS configuration was the employed rainwater mixing ratio estimation method. As illustrated in Fig. 2.2, at each analysis time, the figure presents (1) the rainwater mixing ratio estimated by Eq. (2.22) based on the observed maximum mosaic reflectivity from QPESUMS (provided by the Central Weather Administration), (2) the 3-D maximum rainwater mixing ratios produced by IBM_VDRAS using both the hybrid and original estimation methods, and (3) the 3-D maximum rainwater mixing ratio differences between the two methods. Figure 2.2 indicates that the maximum rainwater mixing ratio values obtained by two methods were obviously lower than observed ones. Furthermore, the maximum rainwater mixing ratio values obtained using hybrid method were generally higher than those obtained using the original method, with the maximum difference exceeding 2.0 g kg^{-1}, indicating a notable improvement. Accordingly, the new hybrid scheme is implemented in this study.

2.4 IBM

To account for terrain effects, the Immersed Boundary Method (IBM), proposed by Tseng and Ferziger (2003) , has been introduced. This method can be implemented within a Cartesian coordinate system using either staggered or non-staggered grids. Given the complex terrain of Taiwan, Tai et al. (2017) incorporated the IBM into VDRAS to encompass the orographic influences; the improved system was subsequently termed IBM_VDRAS. A key advantage of this technique is that it does not require modification of the VDRAS dynamic core, making it relatively straightforward to implement. The procedure of the IBM is briefly introduced below.

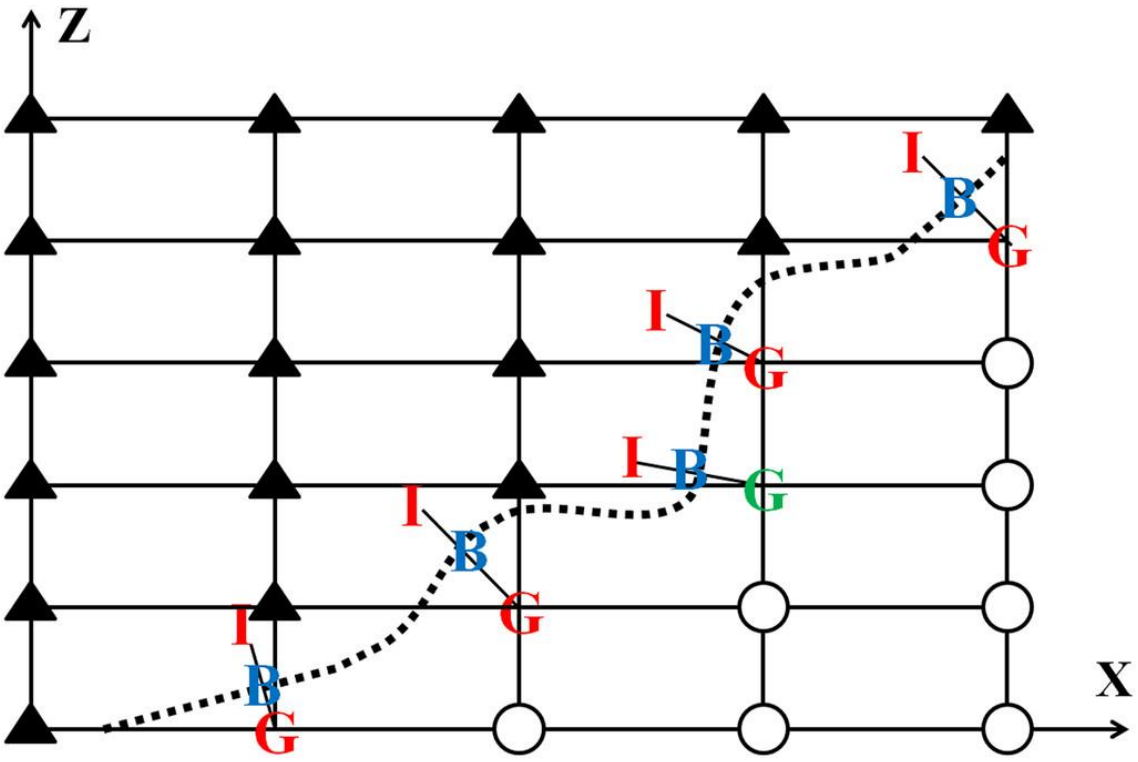

Figure 2.3. Three classifications of grid points along X- and Z- directions. Dashed line represents the terrain surface boundary. Grids with filled triangles denote flow regime points, while grids with open circles denote points inside the terrain. Locations of ghost cell grids, boundary points, and image points are labeled with letters ''G", ''B", and ''I," respectively. These three grid points are connected with lines perpendicular to the terrain surface boundary. It is noted that green point ''G" and red point ''G" are the first grid points immediately inside the terrain when searching along the horizontal direction (from the flow regime) and vertical (from the top) direction, respectively. Source from Tai et al. (2017).

As shown in Fig. 2.3, the model grid points are initially classified into terrain grid points (grid points inside the terrain) and flow regime points. The ghost cell grid is defined as the first grid point immediately inside the terrain when searching either vertically from the top or horizontally from the flow regime. The image point is located symmetrically to the ghost cell relative to the boundary surface. The straight line connecting image point and ghost cell grid is perpendicular to the plane tangential to the boundary.

The values at the image points are interpolated from points in flow regime using Inverse Distance Weighting (IDW) method, chosen for its simplicity and accuracy (Franke, 1982). The IDW formulas following Gao et al. (2007) are given as:

$$\Phi_I = \frac{1}{W_{tot}} \sum_{m=1}^{n} W_m \Phi_m \qquad (2.31)$$

$$W_m = \left(\frac{D-d_m}{Dd_m}\right)^p \quad (2.32)$$

$$W_{tot} = \sum_{m=1}^{n} \left(\frac{D-d_m}{Dd_m}\right)^p. \quad (2.33)$$

Here, Φ_I and Φ_m denote the interpolated value at the image point and the value at m-th selected point in flow regime, respectively. W_m is the weighting coefficient, d_m is the distance between the image point (Φ_I) and the m-th selected point (Φ_m), and D is the distance from the image point to the farthest selected point in flow regime. The power p is set to be 0.5. W_{tot} stands for the sum of all n weighting coefficients. Once the values at the image points are obtained, the values at the ghost cell grids can be determined by applying two types of boundary conditions:

$$\frac{\partial \Phi_x}{\partial n_r} = 0 \quad (2.34)$$

$$\Phi_{G,w} = u\frac{\partial h_t}{\partial x} + v\frac{\partial h_t}{\partial y}. \quad (2.35)$$

Eq. (2.34) is Neumann boundary condition. Φ_x are the values of variables including horizontal winds (u, v), liquid water potential temperature (θ_l), mixing ratios of total water (q_t), and mixing ratios of rainwater (q_r) at ghost cell grid points. n_r is the distance normal to the surface of the terrain. This condition assumes the values of these variables at the ghost cell grids to be equal to those at their corresponding image points.

Eq. (2.35) is Dirichlet boundary condition. $\Phi_{G,w}$ is the vertical velocity at the ghost cell point. h_t, u and v stand for the terrain height, and the horizontal wind components in the flow regime but closest to the image point associated with the ghost cell grids, respectively. This condition assumes that the vertical velocity at the lower boundary is induced by the terrain.

Upon updating all prognostic variables at the ghost cell grids, terrain effects are resolved, and the lower boundary conditions of the model are correspondingly updated. Through nonlinear model integration, performed exclusively for flow regime points with the updated lower boundary conditions, the model prediction for the subsequent time step is obtained.

Chapter 3 Data, configuration and validation

3.1 Data Preparation

The 4DVar analysis system was employed in this study to analyze the rainfall event. Prior to assimilating the radar data into the system, the mesoscale background fields were prepared to provide, and quality control (QC) procedures were performed to ensure that the radar data did not contain erroneous data points.

3.1.1 Mesoscale background

In this study, ECMWF Reanalysis v5 (ERA5) hourly data, produced by the Copernicus Climate Change Service (C3S) at the European Centre for Medium-Range Weather Forecasts (ECMWF), were utilized to generate the mesoscale background field. The horizontal grid resolution is 31 km with atmospheric parameter on 37 pressure levels. The Weather Research and Forecasting Model (WRF), a mesoscale numerical weather prediction system designed for both atmospheric research and operational forecasting applications, was employed to interpolate the ERA5 data to finer horizontal resolution, a process analogous to downscaling. The nested domains consisted of three domains with grid spacings of 9 km (D01), 3 km (D02), and 1 km (D03), as shown in Fig. 3.1. The finest horizontal resolution of nested domains was required to be identical to the horizontal resolution used in IBM_VDRAS. After obtaining the horizontally interpolated WRF fields, these fields at the finest resolution were subsequently interpolated vertically to correspond with the height of each layer of IBM_VDRAS, thereby ensuring complete compatibility with both the horizontal and vertical resolutions employed in IBM_VDRAS, which utilizes a Cartesian coordinate system.

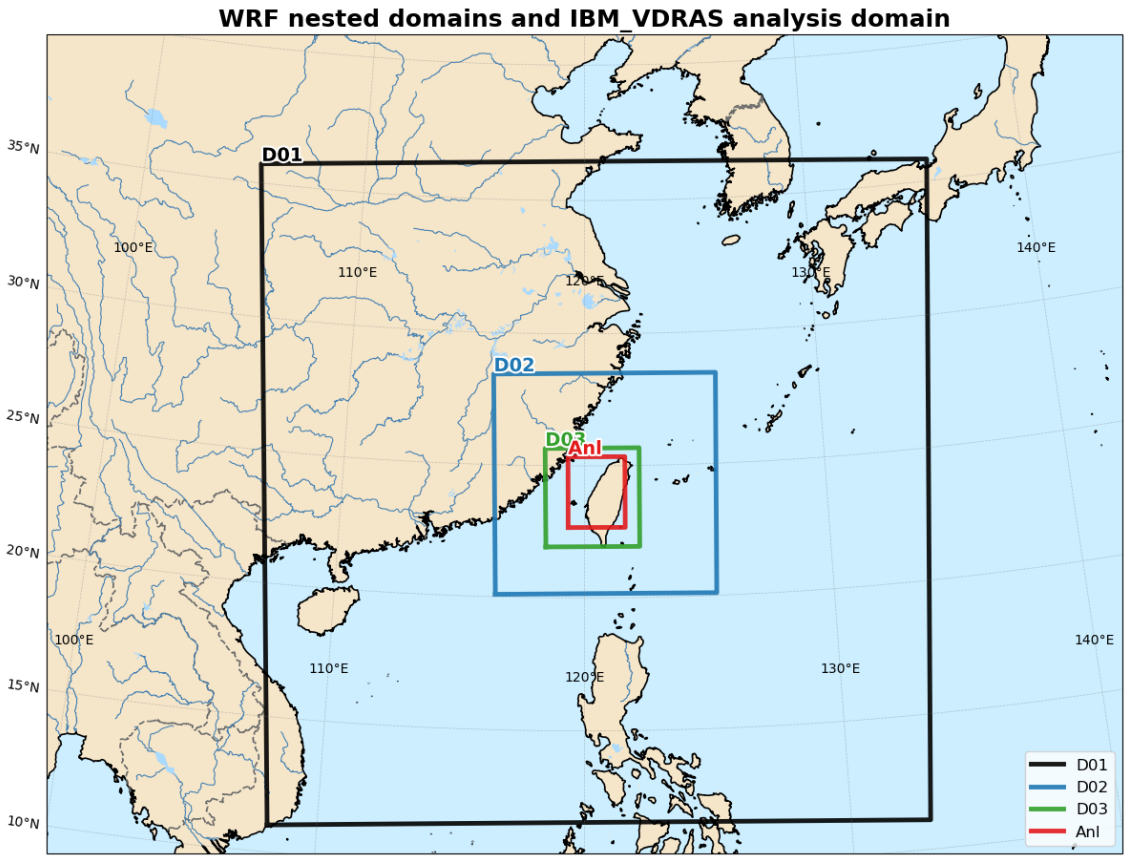

Figure 3.1. WRF nested domains and IBM_VDRAS analysis domain. Black, blue, and green rectangular boxes stand for 9-km (D01), 3-km (D02), and 1- km (D03) domains of WRF nested domains, respectively. Red rectangular box denotes the analysis domain of IBM_VDRAS.

3.1.2 Radar data

To capture the evolution of the MCS that persisted over central Taiwan for several hours, high-resolution observations were crucial, especially over regions where convective development was most active. To maximize the observational coverage of this region, data from seven radars distributed from northern to southern Taiwan were assimilated into IBM_VDRAS, with their locations marked by red diamond symbols in Fig. 3.2. These included the RCMK radar from Republic of China Air Force (ROCAF), the S-band Dual Polarization Doppler Radar (S-POL) from NSF National Center for Atmospheric Research (NCAR), the Taiwan Experimental Atmospheric Mobile Radar (TEAM-R) from the Radar Meteorology Laboratory (RaMeLa) at National Central University (NCU), and four operational radars from the Central

Weather Administration (CWA), including RCWF, RCSL, RCNT, and RCCG. These radars were QCed utilizing the RAKIT (Radar kit) developed by RaMeLa, the details about QC procedures are given in Appendix A.

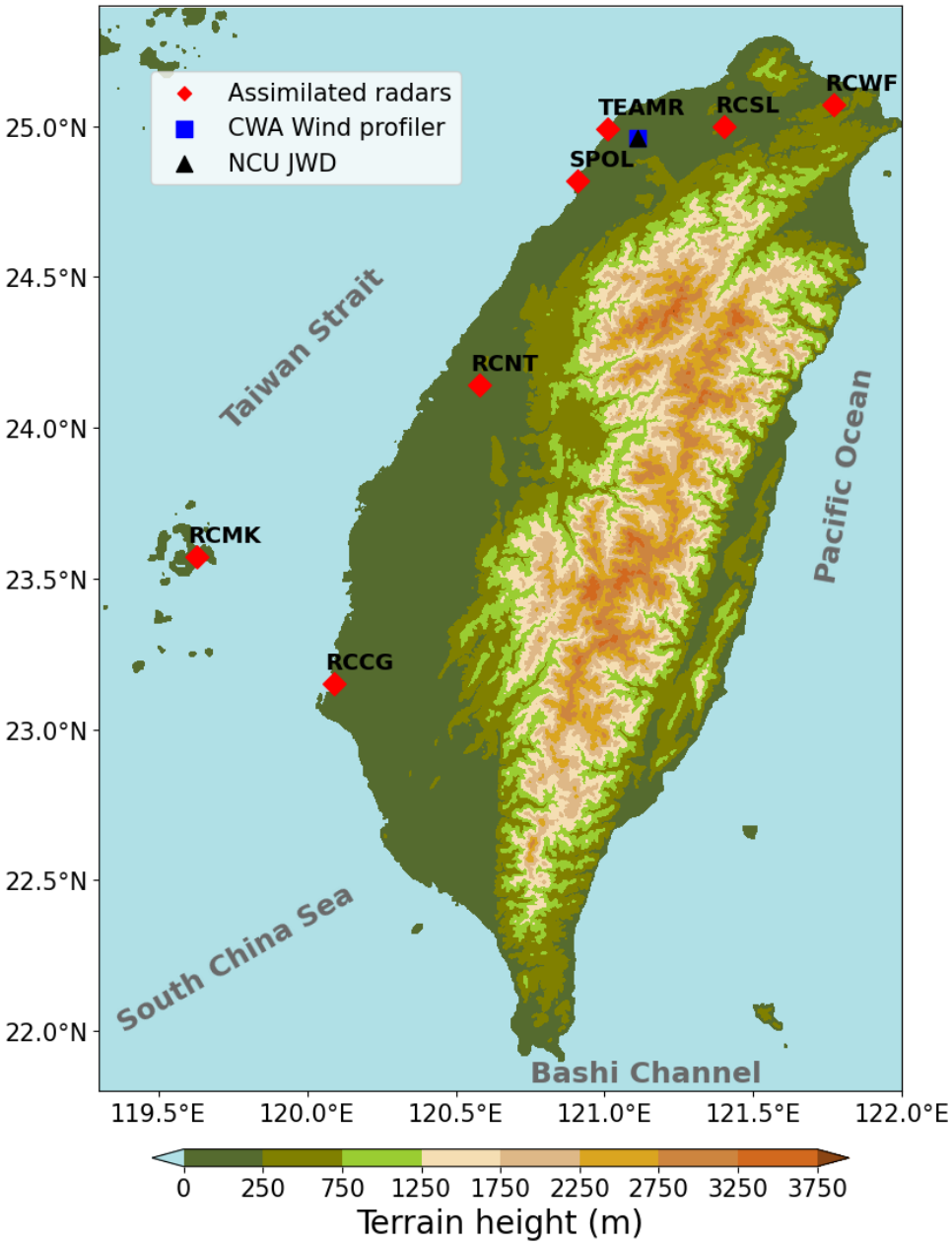

Figure 3.2. Site map of the assimilated radars across Taiwan, with Joss–Waldvogel disdrometer (JWD) and Central Weather Administration (CWA) wind profiler at National Central University (NCU). Red diamond symbols stand for the assimilated radars, including the RCWF, RCSL, TEAM-R, S-POL, RCNT, RCMK, and RCCG. Blue rectangular symbol denotes the CWA wind profiler. Black triangular symbol denotes the Joss–Waldvogel disdrometer (JWD).

3.2 Configuration and validation

3.2.1 Configuration of IBM_VDRAS and assimilation strategy

To investigate the MCS over central Taiwan, the IBM_VDRAS domain was designed to capture the regions of active convective development and orographic influence. As highlighted by the red rectangle in Fig. 3.1, the IBM_VDRAS domain covered the area where the MCS developed and includes most of Taiwan's complex terrain. This domain is nested within the innermost domain of the WRF model. The horizontal resolution of IBM_VDRAS is 1 km and the vertical resolution of it is 0.5 km, with the lowest vertical level at 0.25 km.

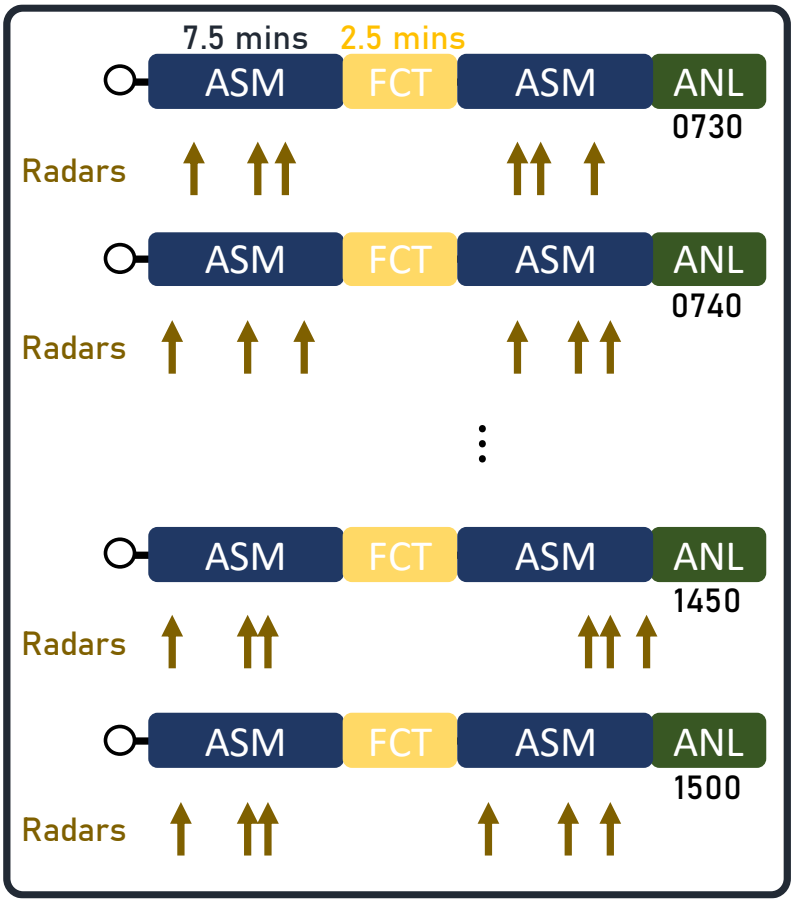

Figure 3.3. Schematic diagram of the assimilation strategy employed in this study. Blue, yellow, and green boxes represent the 7.5-minute assimilation window, 2.5-minute short-term forecast period, and generated analysis fields, respectively. White open circles denote the initial time. Brown arrows indicate radar data available for assimilation into IBM_VDRAS within the assimilation window from seven radars.

Although the latest version of IBM_VDRAS is capable of resolving simple ice phase process, the IBM_VDRAS employed the warm-rain microphysics scheme in this study. To produce high spatiotemporal-resolution analysis fields to investigate this rainfall event, as shown in Fig. 3.3, the schematic diagram of the assimilation strategy demonstrates that each analysis field was generated after two 7.5-minute assimilation windows with a 2.5-minute short-term forecast inserted between them, from 0730 to 1500 UTC 26 May 2022 at 10-minute intervals. Within each assimilation window, the maximum number of radar volume scans from each radar assimilated into IBM_VDRAS was set to be 3. Additionally, since the scanning strategies across 7 radars were not fully synchronized, the total number of radar volume scans across 7 radars assimilated into IBM_VDRAS depended on the data availability across 7 radars during the assimilation window. Eventually, a total of 46 analysis fields was obtained upon completing the entire cycle.

3.2.2 Validation with observation

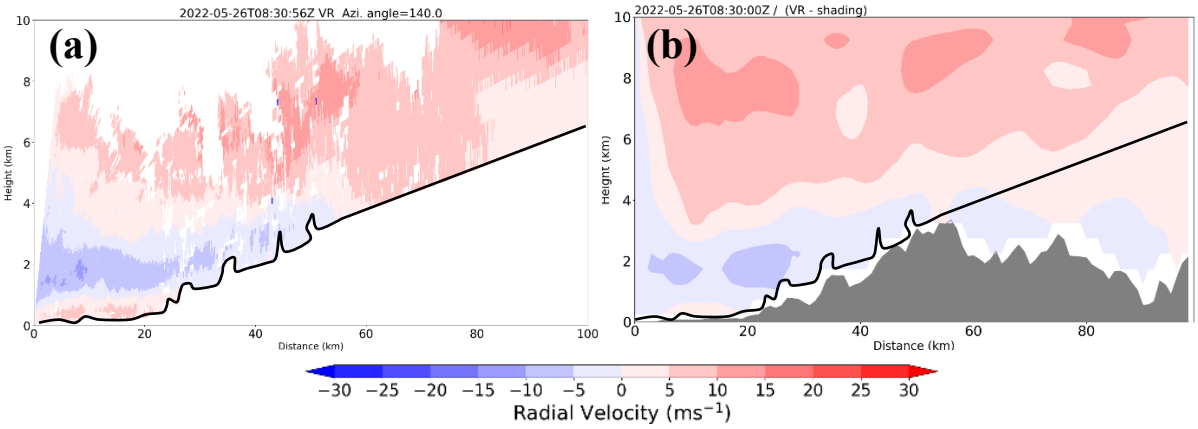

Figure 3.4. RHI data at azimuthal angle 140° from S-POL at 0830 UTC 26 May 2022 and the corresponding vertical cross section from IBM_VDRAS. (a) and (b) show the radial wind fields from S-POL and IBM_VDRAS, respectively. Black line denotes the lowest height of RHI scan along the distance.

Utilizing observed data from the Range Height Indicator (RHI) scanning at azimuthal angle 140° from S-POL at 0830 UTC 26 May 2022, the corresponding vertical cross section of radial wind estimated by IBM_VDRAS was validated, as shown in Fig. 3.4. The radial winds

were well captured, where the observed blowing-away radar wind was detected at both lower and upper levels, and observed blowing-toward radar wind was detected between these levels (Fig. 3.4a). As shown by the wind field above the black line in Fig. 3.4b, these patterns were successfully reproduced by IBM_VDRAS.

The CWA wind profiler data (marked by blue rectangular box in Fig. 3.2) were compared with the analysis field at each analysis time and over the entire analysis period. The root mean square error (RMSE) and relative root mean square error (RRMSE) of wind speed between the wind profiler and the analysis fields were calculated. Prior to computing the validation of wind direction, data points of the wind speeds from the wind profiler below 1 ms^{-1} were filtered out. The validation of wind direction was performed by calculating the inner product of the wind vectors from analysis fields and from wind profiler to obtain the angular difference. The angular difference was then used to calculate the root mean square (RMS) and relative root mean square (RRMS). The formulas are given as:

$$RMS = \sqrt{\frac{\sum_{i=1}^{N} x_i^2}{N}} \quad (3.1)$$

$$RMSE = \sqrt{\frac{\sum_{i=1}^{N} (x_{mod,i} - x_{obs,i})^2}{N}} \quad (3.2)$$

$$RRMS = \frac{RMS}{\bar{x}} \quad (3.3)$$

$$RRMSE = \frac{RMSE}{\bar{x}_{obs}}. \quad (3.4)$$

Here, the *N* denotes the total number of data points. The variables x_i, $x_{mod,i}$ and $x_{obs,i}$ represent the *i-th* data point, data point from analysis fields and data point from wind profiler, respectively. The overbar denotes the average computed over all data points.

As shown in Fig. 3.5a and 3.5b, the RMSEs (RRMSEs) of wind speed and RMSs (RRMSs) of wind vector angular difference remained predominantly below 5 ms^{-1} (0.35) and 50° (0.20), respectively, throughout the entire analysis period. The validation across all analysis fields against wind profiler was computed as well to provide an overall assessment. The RMSE

and RRMSE of wind speed were approximately 3.34 ms^{-1} and 0.218, respectively, while the RMS and RRMS of wind vector angular difference were roughly 23.02 ° and 0.098, respectively. These results demonstrate that the retrieved analysis fields were sufficiently accurate for investigating the rainfall event.

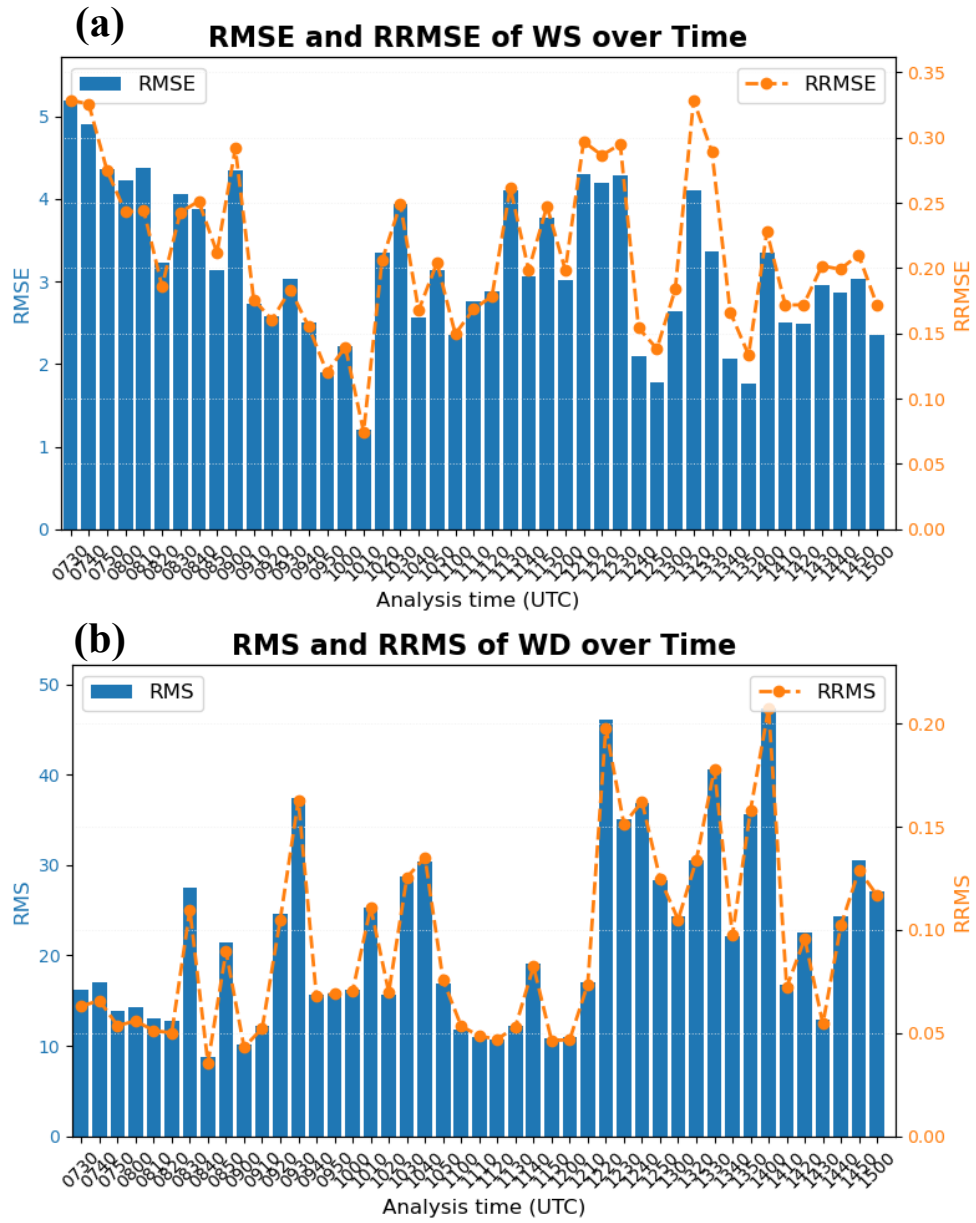

Figure 3.5. Validation results of analysis fields against the CWA wind profiler at NCU. (a) represents the RMSE and RRMSE between the wind speeds of the analysis fields and the CWA wind profiler. (b) represents the RMS and RRMS of the angular differences of the wind vectors between the analysis fields and the CWA wind profiler.

Chapter 4 Results and discussion

4.1 Case overview

The TAHOPE field campaign was conducted from late May to mid-August in 2022 to enhance the understanding of extreme rainfall events and improve forecasting in the Taiwan area. During the early phase of field campaign, from late May to June, Taiwan is typically influenced by quasi-stationary Mei-Yu fronts, which can contribute to torrential rainfall and significant financial losses. In this study, a quasi-stationary prolonged MCS event lasting from 0700 to 1500 UTC 26 May during IOP#1 is investigated.

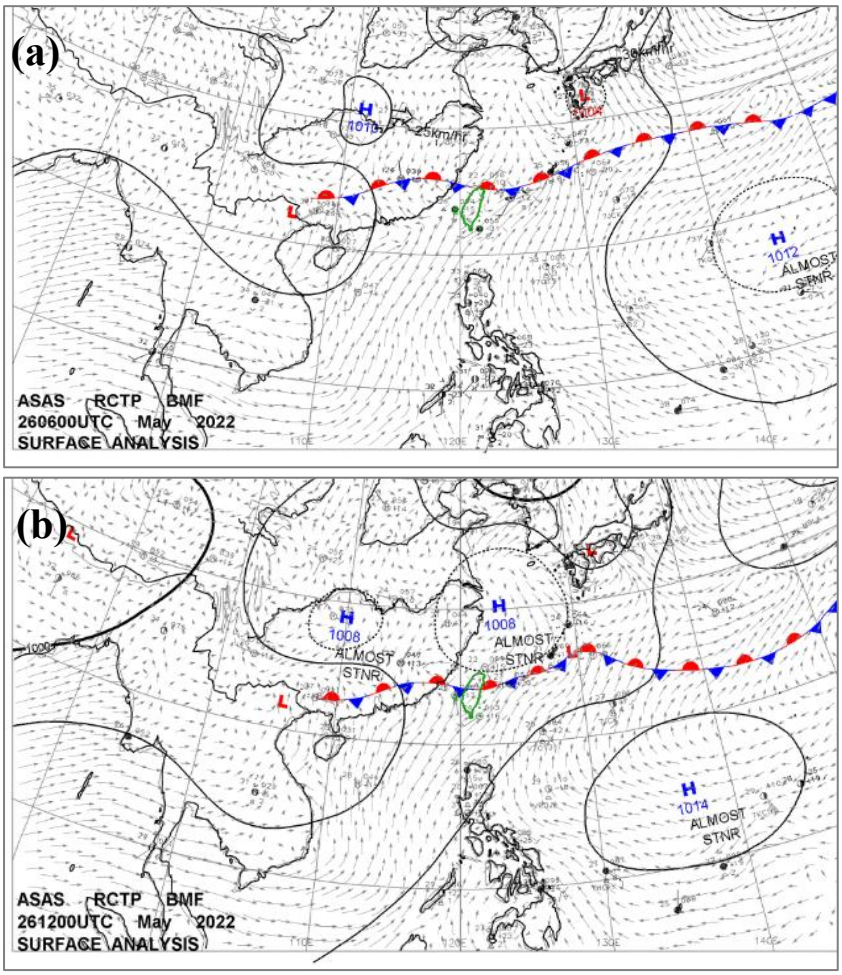

Figure 4.1. Surface weather maps at (a) 0600 and (b) 1200 UTC on 26 May 2022.

4.1.1 Pre-MCS conditions

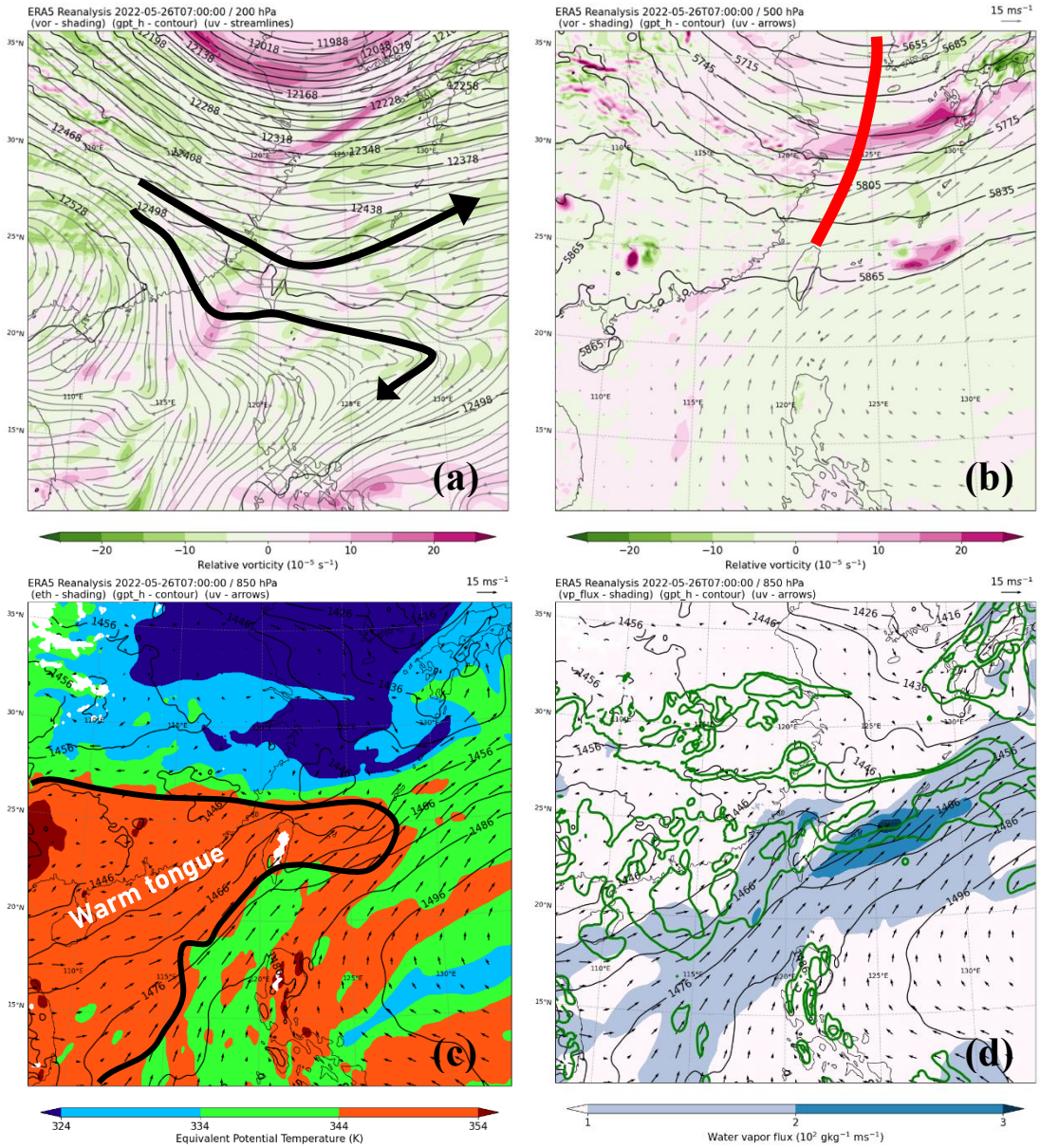

Figure 4.2. Upper-level weather maps at 0600 UTC 26 May 2022. (a) and (b) represent the 200-hPa and 500-hPa weather maps, while (c) and (d) represent 850-hPa weather maps. Black contour lines in (a) to (d) denote geopotential heights (unit: m). Shading in (a) and (b) stands for relative vertical vorticity. Shading in (c) and (d) stands for equivalent potential temperature and water vapor flux, respectively. Green contour lines in (d) stand for the 85% and 95 % relative humidity levels. (b) to (d) are overlaid by horizontal wind fields, whereas (a) is overlaid by streamlines.

On 26 May 2022, shown in Fig 4.1, surface weather maps reveal that the Mei-Yu front was situated north of Taiwan at 06 UTC (Fig. 4.1a). The front subsequently moved over Taiwan by 12 UTC, following the eastward progression of the high-pressure system located over Eastern

China (Fig. 4.1b). This shows that Taiwan was influenced by the Mei-Yu front during this period.

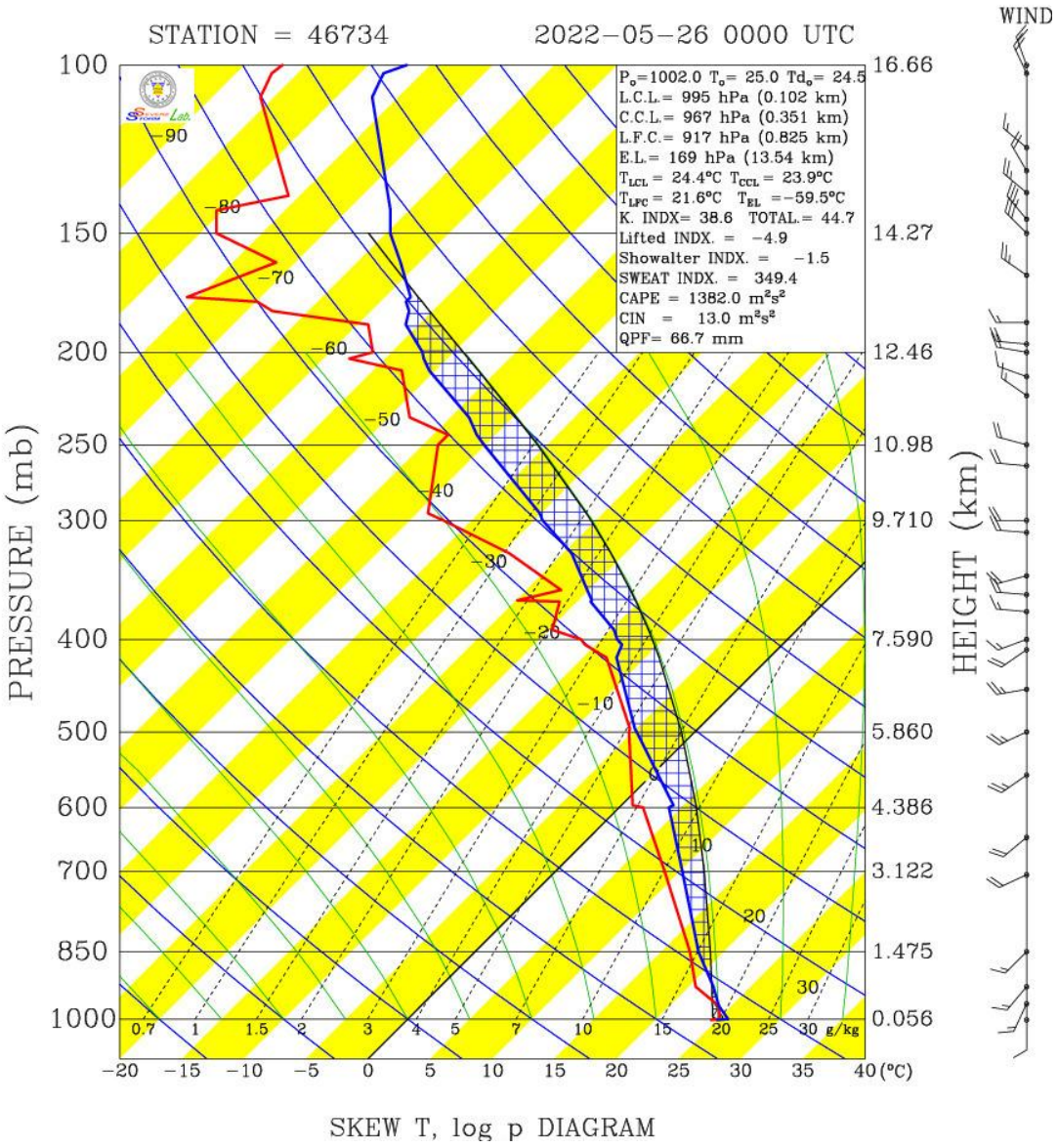

Figure 4.3. Magong sounding profile at 00 UTC 26 May 2022.

A pronounced 200-hPa divergent flow was observed east of Taiwan, as indicated by the black arrows in Fig. 4.2a. Meanwhile, a 500-hPa trough, marked by the red line in Fig. 4.2b, extended from the southwest of Korea to the north of Taiwan. These conditions suggest a favorable environment for upward motion near Taiwan due to upper-level divergent configuration. At lower level, 850-hPa weather maps reveal that Taiwan was under the influence of a strong southwesterly monsoonal flow, which transported substantial water vapor (Fig. 4.2d).

A moist region (outlined by green contours in Fig. 4.2d) and a warm tongue (characterized by equivalent potential temperature exceeding 344 K in Fig. 4.2c) extended from the South China Sea to the areas north of Taiwan. Accordingly, the transport of low-level warm, moist air was conducive to the development of moist convection over Taiwan.

The sounding profile at 00 UTC in Magong (Fig. 4.3) shows that the southwesterly flow extended from the near-surface layer up to 500-hPa layer. Additionally, it is observed that the temperature line was close to the dew point temperature line at low level, indicating a moist low-level environment, and the CAPE value reached 1382 m^2s^2, suggesting a conducive condition for deep convective development.

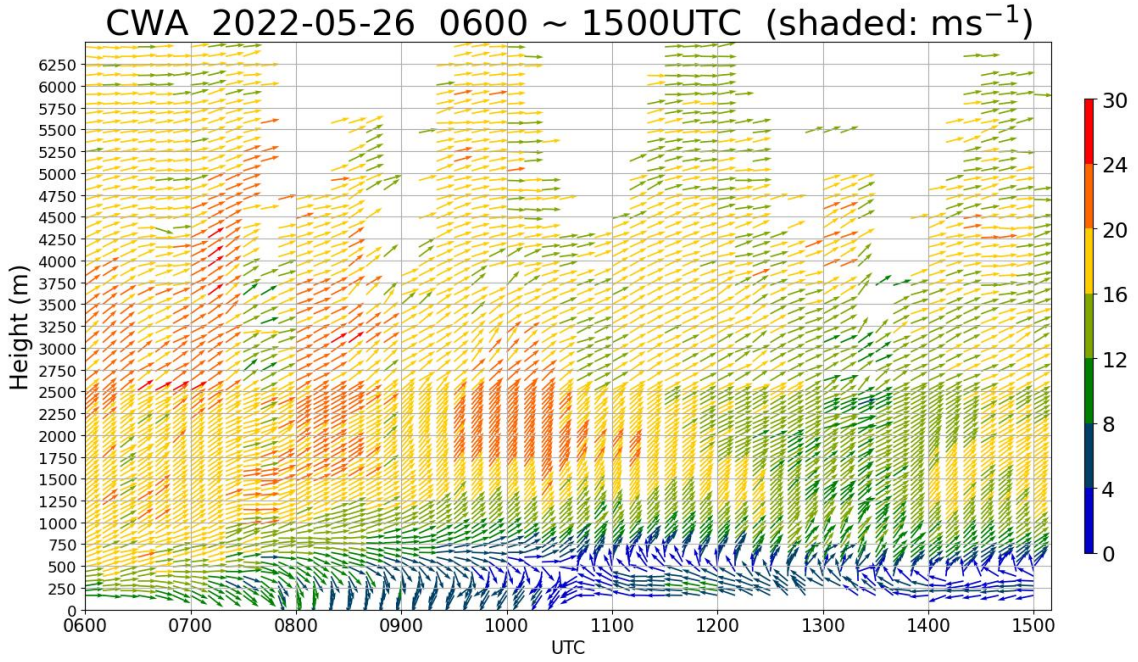

Figure 4.4. CWA wind profiler (at NCU) from 0600 to 1500 UTC 26 May 2022.

The CWA wind profiler at NCU (Fig. 4.4) exhibited that the near-surface westerly winds began transitioning at 08 UTC and eventually became easterly winds. The top layer of easterly winds was observed around 0.5 km, with southwesterly winds dominating above this layer up to 5 km. Notably, the low-level southwesterly winds between 0.5 and 1.25 km were mostly stronger than 16 ms^{-1} but began weakening after 0800 UTC, revealing a possible existence of a LLJ at the early stage.

4.1.2 Evolution of MCS

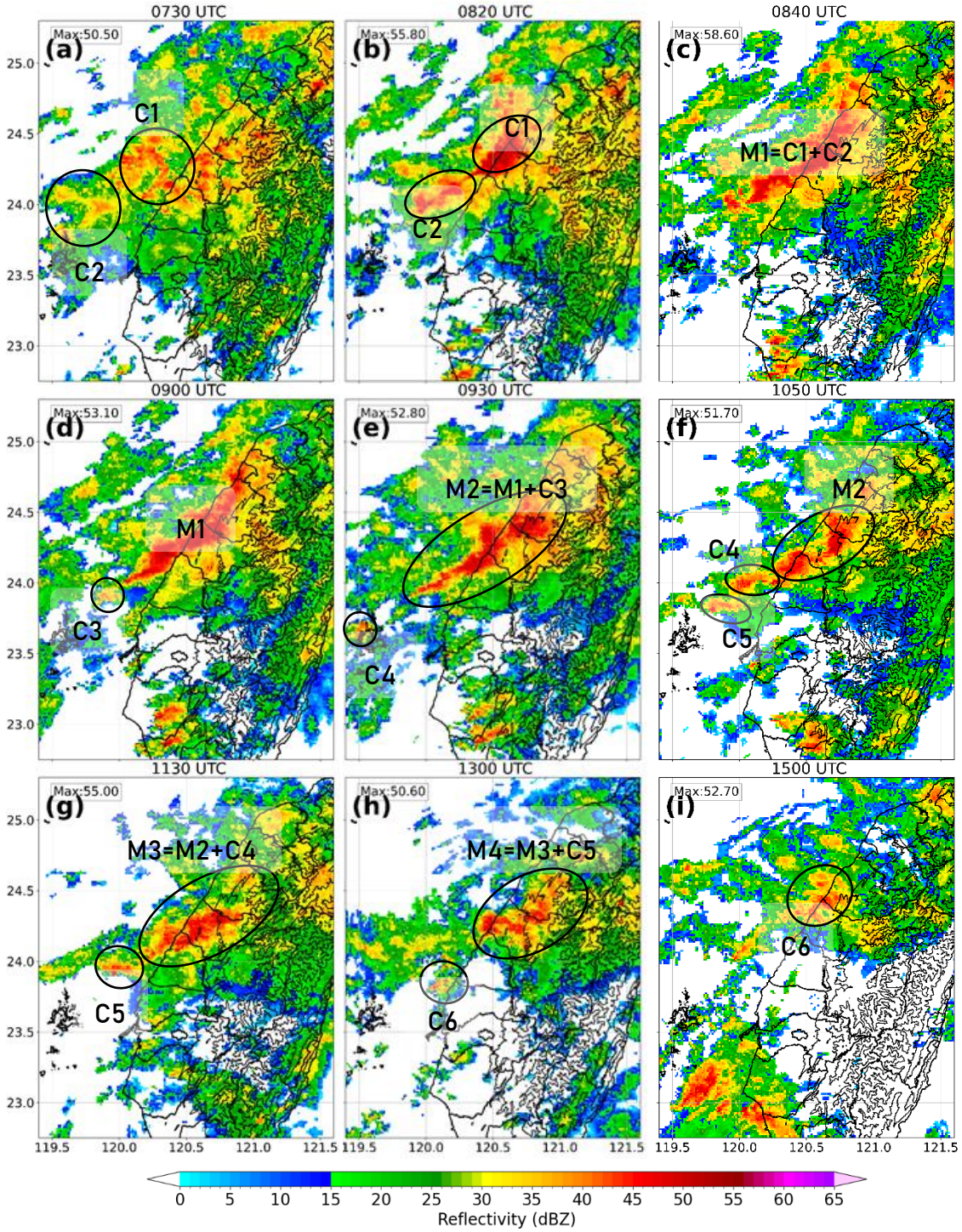

Figure 4.5. Observed maximum mosaic reflectivity from QPESUMS at (a) 0730, (b) 0820, (c) 0840, (d) 0900, (e) 0930, (f) 1050, (g) 1130, (h) 1300, and (i) 1500 UTC 26 May 2022. New convective cells are labeled with prefix ''C,'' such as C1 to C6, while merged cells are labeled with prefix ''M,'' such as M1 to M4.

The observed maximum mosaic reflectivity from QPESUMS (Fig. 4.5), provided by the

CWA, illustrates that the new convective cells were repeatedly formed at different but nearby upstream locations. These cells, labeled with the prefix "C" (e.g., C1 to C6), propagated toward the same downstream region (central Taiwan) and merged with the pre-existing convective cells. The resulting merged cells are labeled with the prefix ''M" (e.g., M1 to M4). This pattern indicates that the MCS exhibited the characteristics of a back-building system. The MCS maintained a widespread area of high reflectivity from 0800 to 1100 UTC. However, after 1100 UTC, the MCS gradually weakened, with the high-reflectivity area diminishing in scale, eventually leaving only a single convective cell, C6.

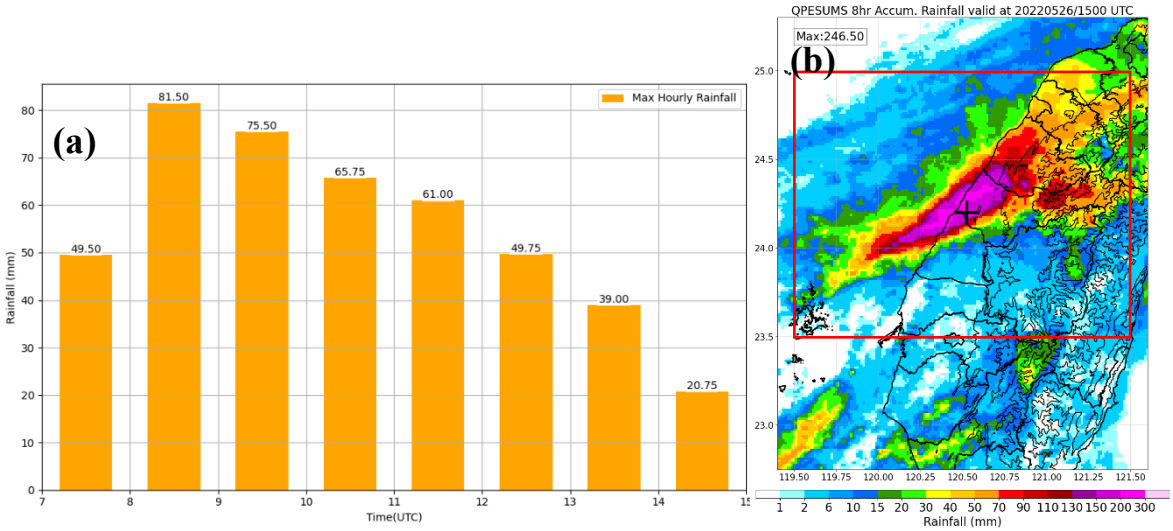

Figure 4.6. (a) stands for the 2-D maximum hourly rainfall within the red box in (b). (b) stands for 8-hr accumulated rainfall from QPESUMS between 0700 and 1500 UTC 26 May 2022. Cross symbol in (b) marks the location of the maximum 8-hr accumulated rainfall.

The hourly accumulated rainfall shown in Fig. 4.6a reveals that the maximum hourly rainfall exceeded 70 mm from 08-09 UTC and from 09-10 UTC periods. The 8-hour accumulated rainfall shown in Fig. 4.6b shows that the major heavy rainfall areas exhibited an elongated triangle shape, with a maximum value of 246.50 mm located in central Taiwan.

Correspondently, from Fig. 4.7, it can be observed that most of the convective cells were concentrated over Central Taiwan throughout this rainfall event. Knowing favorable synoptic conditions, the purpose of this research is to investigate what favorable local conditions could

repeatedly trigger convection upstream, intensify convection when they approached central Taiwan, and cause the MCS to stay quasi-stationary for a prolonged time under multi-scale factors including Mei-Yu front, prevailing southwesterly flow and terrain effect.

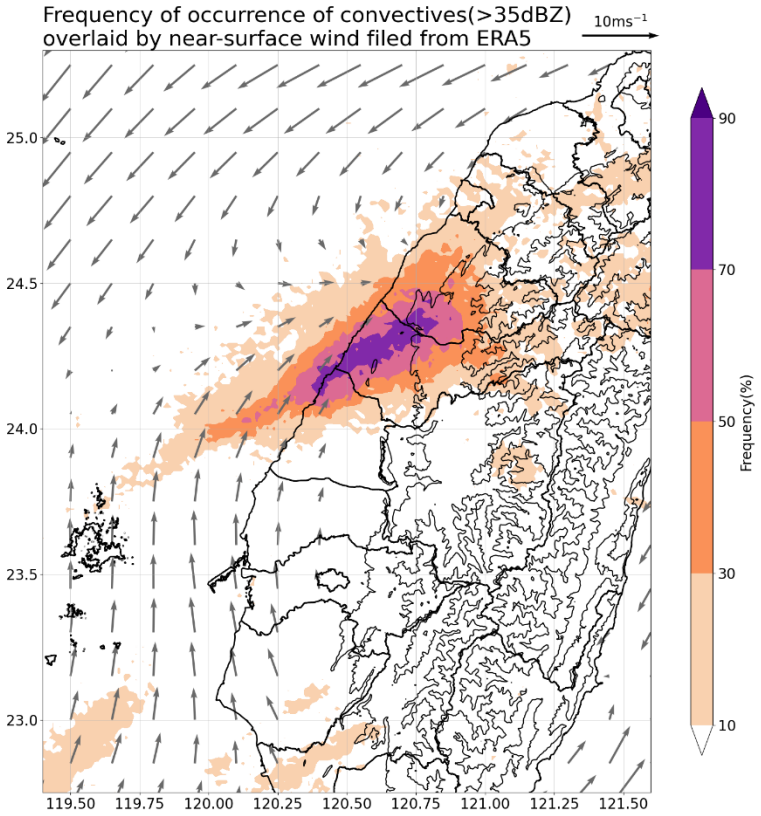

Figure 4.7. Frequency distribution of the observed maximum mosaic reflectivity from QPESUMS exceeding 35 dBZ at each grid point during the period from 0700 to 1500 UTC 26 May 2022.

4.2 IBM_VDRAS analysis

4.2.1 0730 – 1100 UTC：Early stage with favorable local conditions

During the period shown in Figs. 4.8a to 4.8e, wide-ranging linear convective cells formed from north of Penghu to northwest of Taiwan. Southwesterly winds prevailed over the analysis domain, with LLJ (indicated by red arrows) forming over central Taiwan. A near-surface front (defined as the boundary between the northeasterly and southwesterly winds, indicated by black

dashed lines) was situated northwest of Taiwan. As time progressed shown in Fig. 4.8f, the southwesterly winds weakened, leading to a gradual weakening of the LLJ, while the front steadily shifted southward and remained west of Taiwan. Consequently, the convective cells shifted southward accordingly.

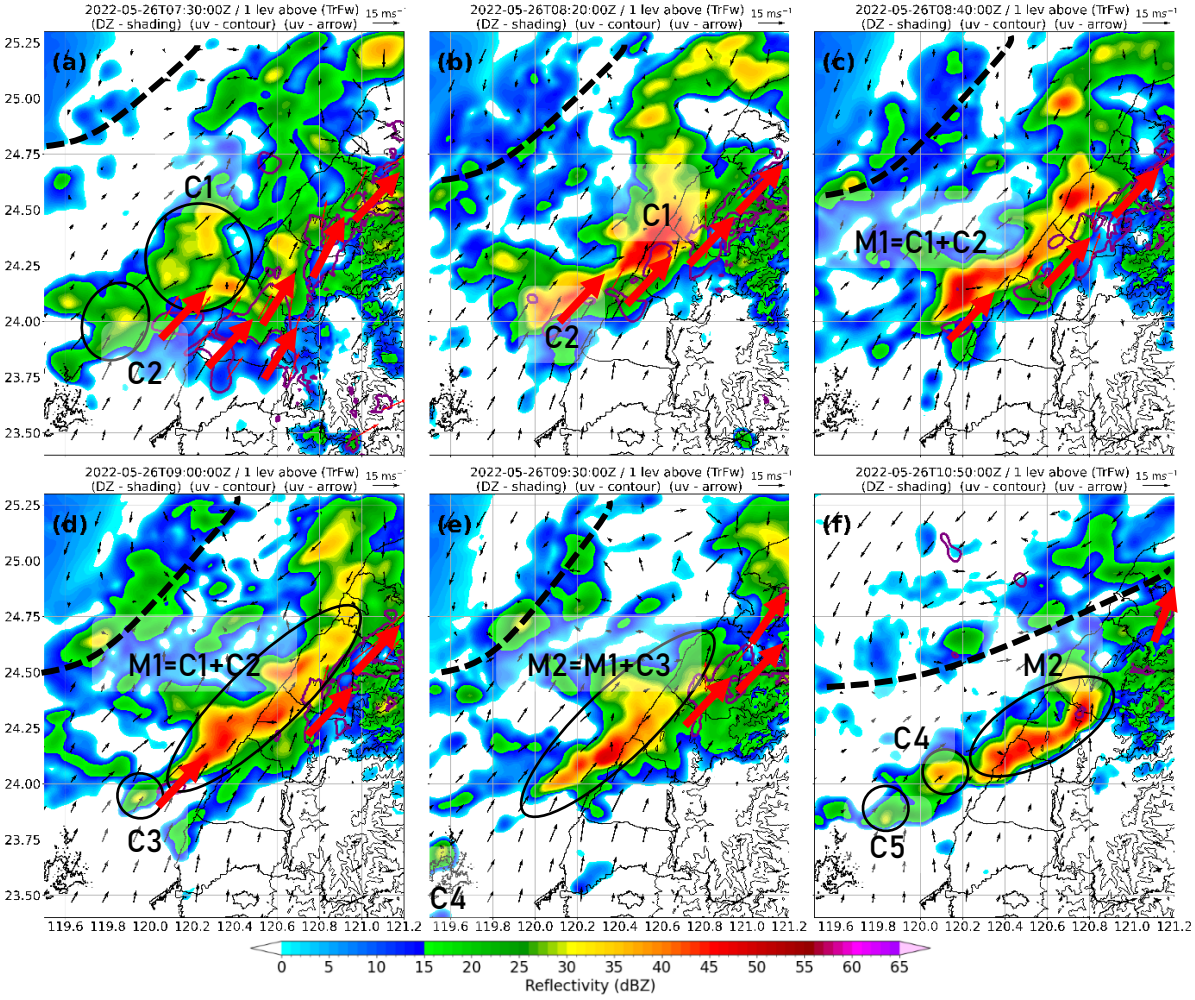

Figure 4.8. Terrain-following reflectivity field estimated using Eq. (2.22), overlaid by wind field. Red arrows and purple solid lines stand for wind speeds exceeding 15 ms^{-1} and the area where wind speeds exceeding 15 ms^{-1}, respectively. Black dashed lines stand for near-surface fronts. (a) to (f) correspond to 0730, 0820, 0840, 0900, 0930, 1050 UTC 26 May 2022, respectively.

To examine the moisture transport associated with the LLJ, the total Integrated Vapor Transport (hereafter referred to as IVT) was calculated, given as:

$$IVT_x = \frac{-1}{g}\int udp \qquad (4.1)$$

$$IVT_y = \frac{-1}{g}\int vdp \qquad (4.2)$$

$$Total\ IVT = \sqrt{{IVT_x}^2 + {IVT_y}^2}. \qquad (4.3)$$

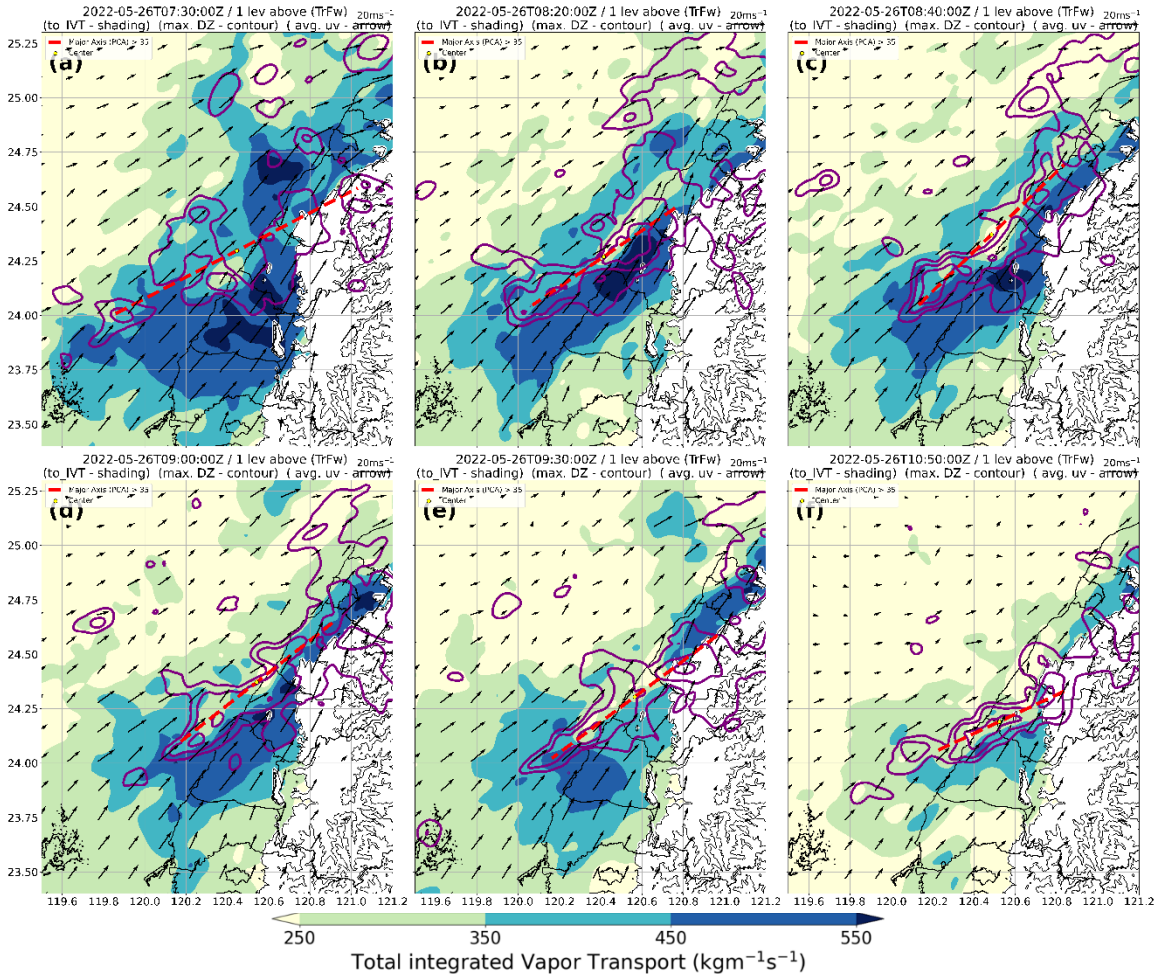

Figure 4.9. Shading indicates low-level IVT within 0.25-2.25 km layer, with purple contour lines of the 2-D maximum reflectivity at 25, 35, and 45 dBZ. Wind arrows depict the average wind field within 0.25-2.25 km layer. Red dashed lines indicate the major axes of convective regions with reflectivity exceeding 35 dBZ. (a) to (f) correspond to 0730, 0820, 0840, 0900, 0930, 1050 UTC 26 May 2022, respectively.

Meanwhile, the major axes of convective cells with reflectivity exceeding 35 dBZ were identified by extracting the first principal component using Principal Component Analysis (PCA). Further details are given in Appendix B. As shown in Fig. 4.9, the major axes (marked by red dashed lines) were oriented from northeast to southwest and formed angles with respect to the prevailing southwesterly winds, causing the low-level IVT to concentrate on the southeastern flanks of the convective cells. Additionally, the existence of the LLJ enhanced moisture supply from the windward sides of the convective cells (Fig. 4.9a to 4.9e), supporting

the wide-ranging convective developments. The K-Index (KI) was analyzed to evaluate the potential for convection development. It is defined as:

$$KI = (T_{850hPa} - T_{500hPa}) + T_{d,850hPa} - \left(T_{700hPa} - T_{d,700hPa}\right), \qquad (4.4)$$

where T and T_d stand for the temperature and dewpoint temperature, respectively. A KI value greater than 35 K indicates a high likelihood of convection activity. As shown in Fig. 4.10, KI values exceeding 35 K, event 40 K, were distributed in the regions where the convective cells were positioned, suggesting that the local thermodynamic conditions were favorable for convective developments.

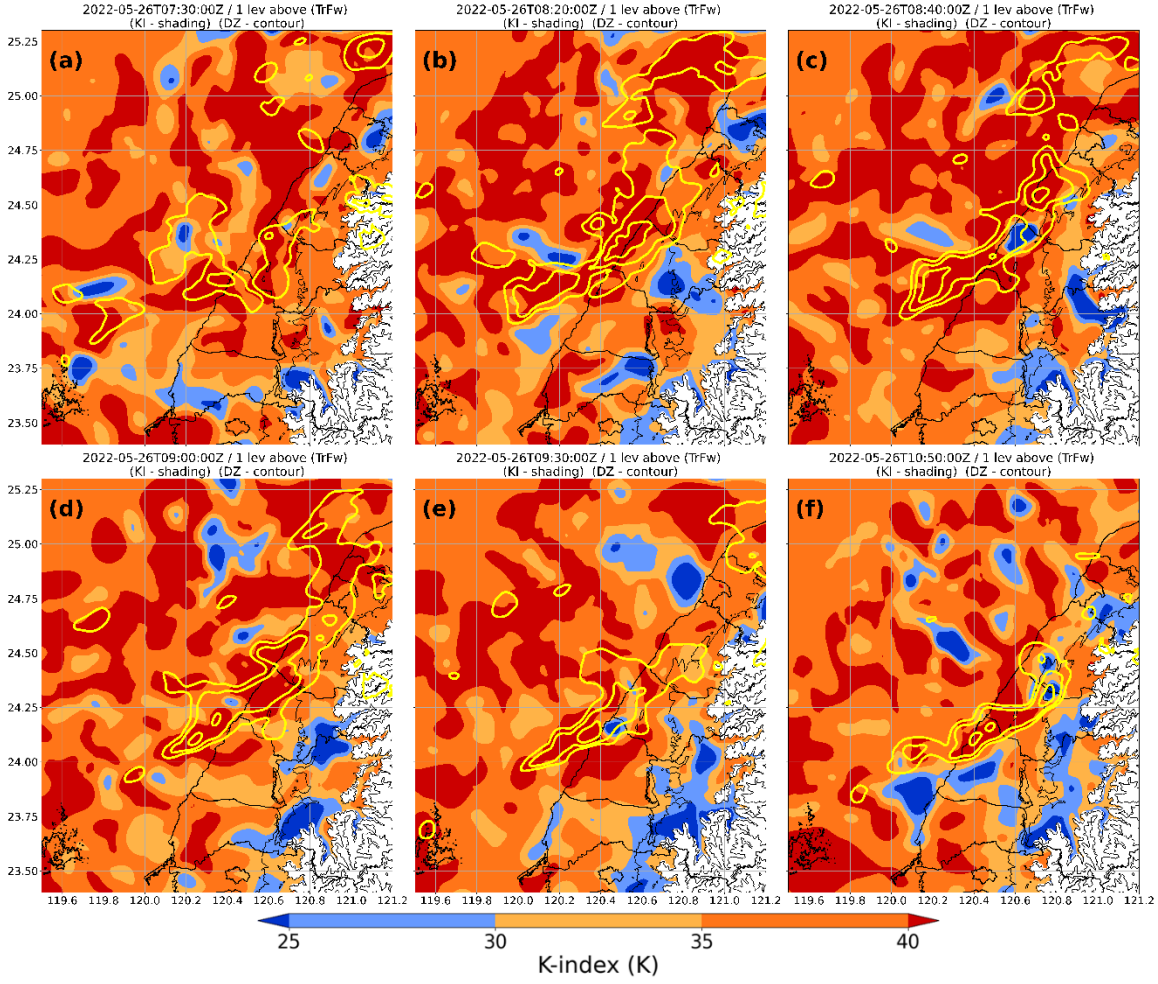

Figure 4.10. Shading indicates terrain-following KI field, overlaid with yellow contour lines of the 2-D maximum reflectivity at 25, 35, and 45 dBZ. (a) to (f) correspond to 0730, 0820, 0840, 0900, 0930, 1050 UTC 26 May 2022, respectively.

An examination of both the near-surface convergence fields (Fig. 4.11) and temperature

fields (Fig. 4.12) reveals that regions of divergence within the convective cells corresponded to lower temperatures compared to other regions within convective cells, indicating the presence of cold pools and their associated outflows. This resulted in convergence lines forming along the windward sides of the convective cells (denoted by black dashed lines in Fig. 4.11) when the southwesterly flow encountered the outflows. Additionally, the near-surface temperature fields revealed that the cold air mass behind the front slowly advanced southward.

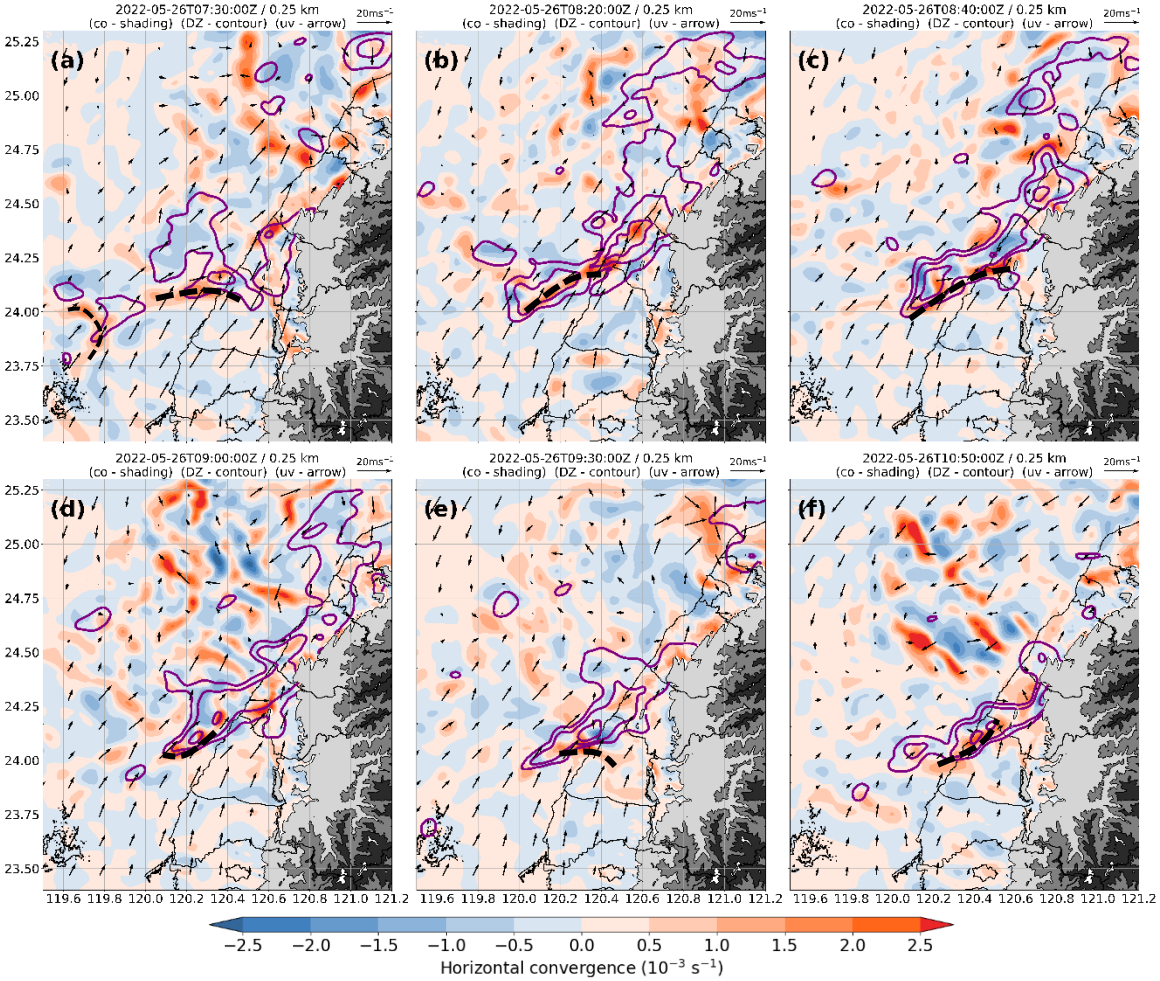

Figure 4.11. Shading indicates 0.25-km convergence field, overlaid with purple contour lines of reflectivity at 25, 35, and 45 dBZ, as well as wind fields. Black dashed lines denote the convergence lines at windward sides of convective cells. (a) to (f) correspond to 0730, 0820, 0840, 0900, 0930, 1050 UTC 26 May 2022, respectively.

As previously mentioned, a substantial amount of water vapor was transported from the windward sides, combined with the convergence lines developing along these windward regions, this allowed the convective cells to sustain their intensities and widespread structures,

and even intensify.

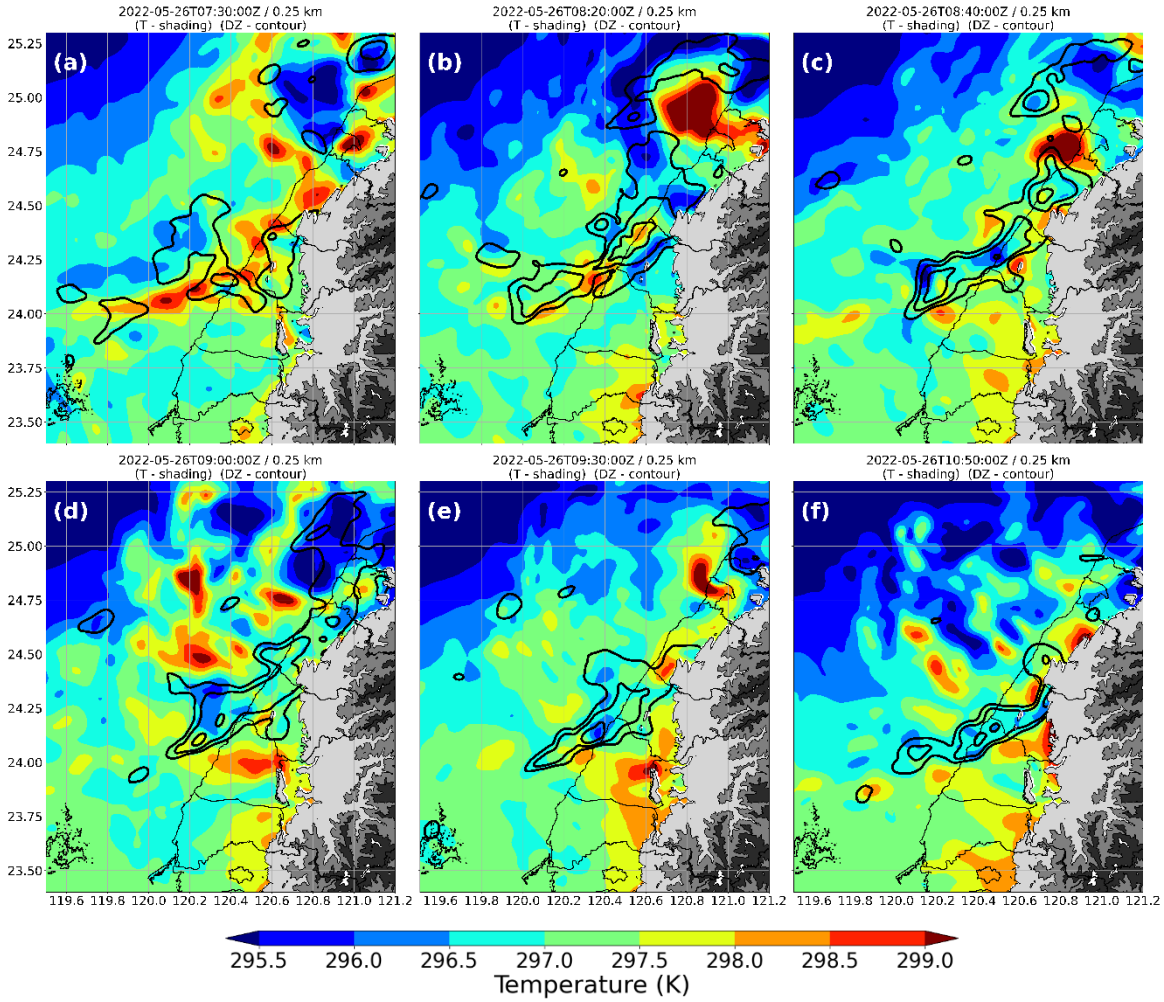

Figure 4.12. Shading indicates 0.25-km temperature field, overlaid with black contour lines of reflectivity at 25, 35, and 45 dBZ. (a) to (f) correspond to 0730, 0820, 0840, 0900, 0930, 1050 UTC 26 May 2022, respectively.

4.2.2 1100 – 1500 UTC：Later stage with unfavorable local conditions

As shown in Fig. 4.13, the convective cells shifted over central Taiwan, accompanied by a gradual re-intensification of the prevailing southwesterly winds and the redevelopment of the LLJ. However, both the maximum wind speed and the spatial coverage of the LLJ were smaller compared to those observed during the early stage. Notably, the northeasterly winds north of

the near-surface front competed with the prevailing southwesterly winds, causing the front to remain quasi-stationary to the west of Taiwan. As the prevailing southwesterly flow weakened, the convective cells propagated downstream more slowly than during the early stage. Concurrently, the cold-air region associated with northeasterly winds continued to advance southward (Fig. 4.14), thereby inhibiting convective development north of the front.

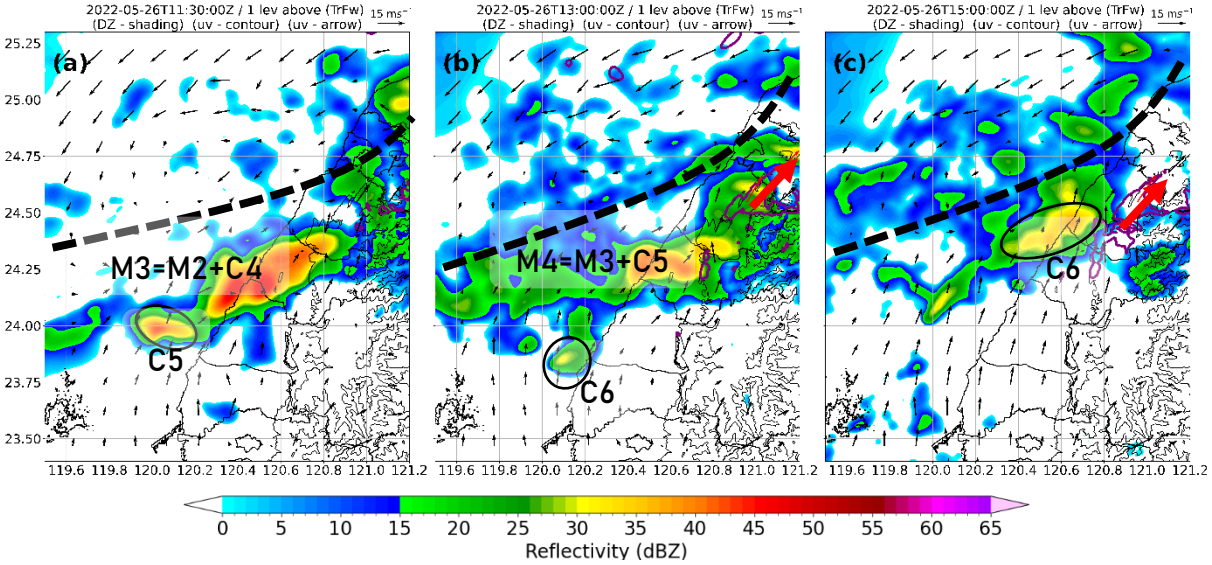

Figure 4.13. Same as Fig. 4.8, but (a) to (c) correspond to 1130, 1300, 1500 UTC 26 May 2022.

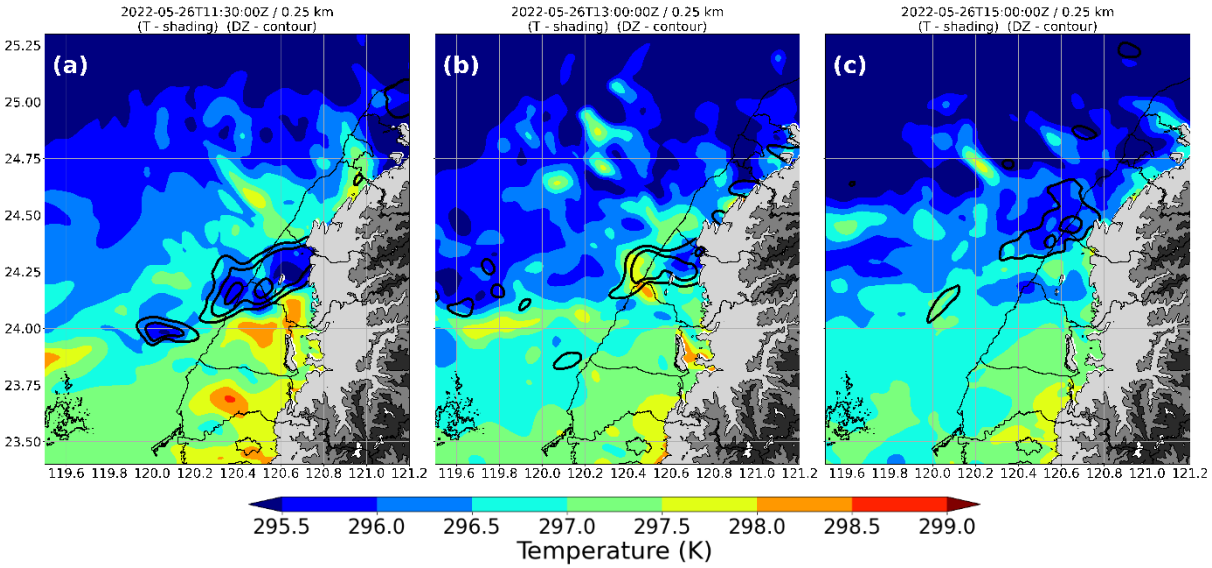

Figure 4.14. Same as Fig. 4.12, but (a) to (c) correspond to 1130, 1300, 1500 UTC 26 May 2022.

According to the IVT field (Fig. 4.15), the low-level IVT over central Taiwan increased steadily over time, whereas the low-level IVT in the northern portion of the analysis domain was less than during early stage, due to the southward progression of the near-surface front. In

addition, the major axes of moisture transport rotated clockwise, eventually aligning in more east–west orientation. This alignment blocked the northward transport of moisture and trapped the moisture transport at the southern sides of convective cells. Compared to earlier times, the KI field (Fig. 4.16) shows a relative decline in favorable conditions for convective development in central Taiwan, with a decrease in areas where KI exceeds 40.

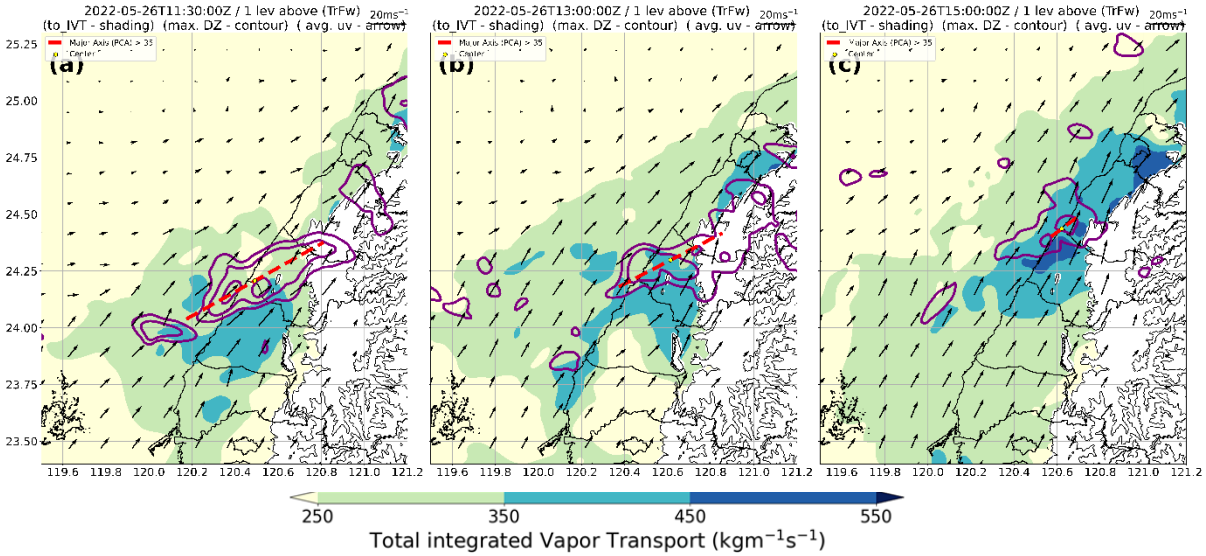

Figure 4.15. Same as Fig. 4.9, but (a) to (c) correspond to 1130, 1300, 1500 UTC 26 May 2022.

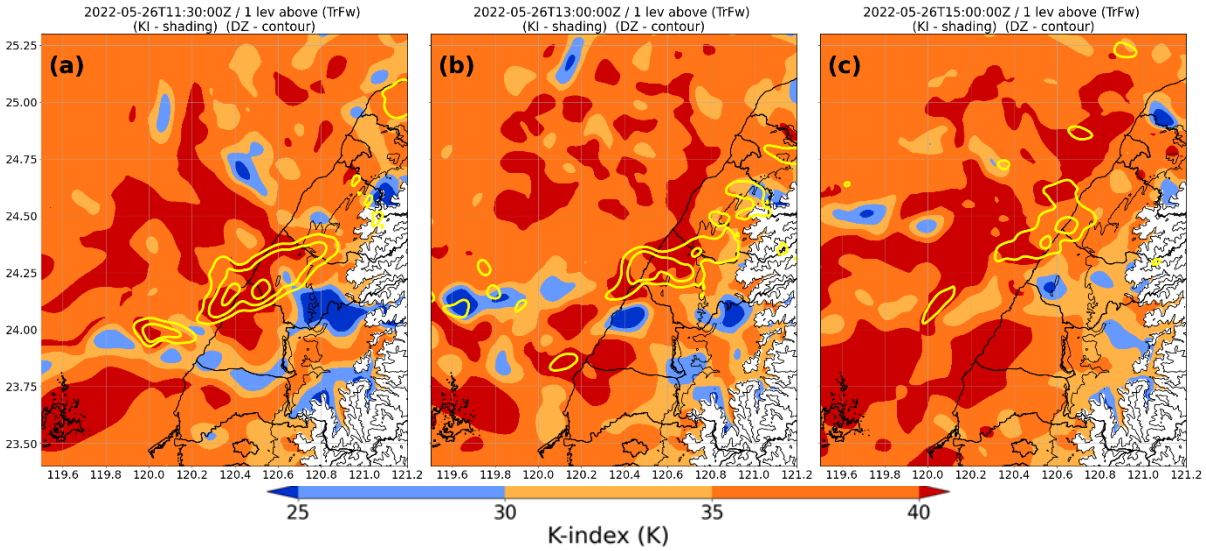

Figure 4.16. Same as Fig. 4.10, but (a) to (c) correspond to 1130, 1300, 1500 UTC 26 May 2022.

Although the convergence lines continued to form along the windward sides of the convective cells (Fig. 4.17), indicating dynamic support for convective development, the overall thermodynamic environment was insufficient to sustain widespread convective

development. As a result, the convective cells gradually diminished in scale and were primarily located farther south compared to early stage.

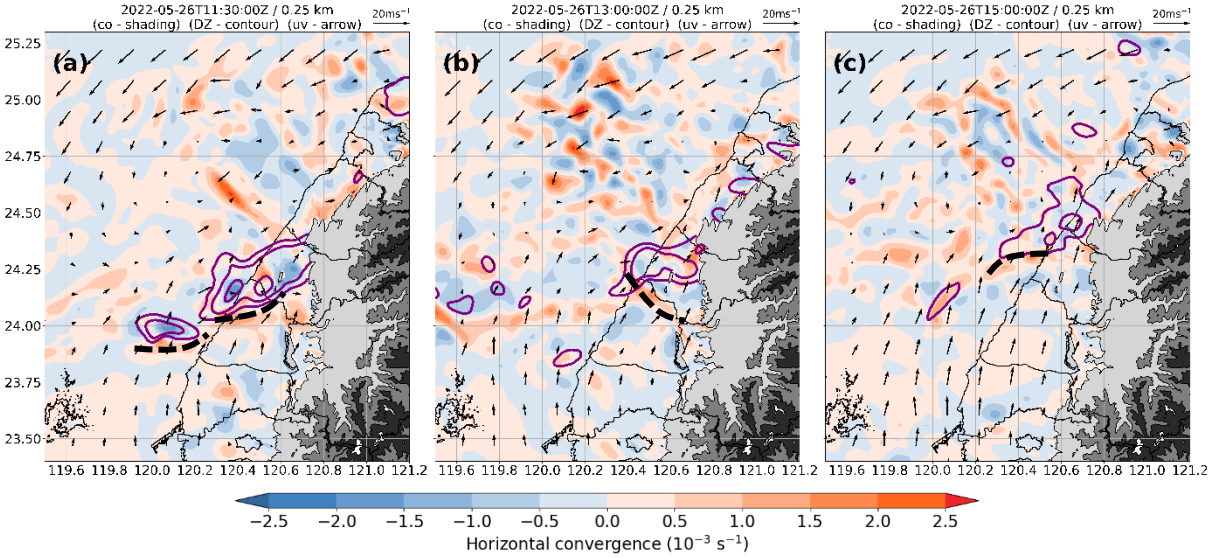

Figure 4.17. Same as Fig. 4.11, but (a) to (c) correspond to 1130, 1300, 1500 UTC 26 May 2022.

4.2.3 Convective structure

Multiple merging processes occurred throughout the MCS event. According to Miao and Yang (2019), merging processes can be classified into two mechanisms: (1) rear-end collisions caused by differential propagation speeds of convective cells, and (2) head-on collisions resulting from oppositely directed outflows generated by convective cells. In this study, the merging processes were primarily attributed to new convective cells moving faster than pre-existing ones, eventually colliding and merging with them, which resembled rear-end collision. During the early stage, favorable local conditions supported convective development, allowing both M1 and M2 to evolve into a widespread linear convective system extending from central to northern Taiwan. However, during the later stage, the weakening of the southwesterly winds and LLJ, accompanied by reduced water vapor transport and cold-air intrusion, limited convective development to central Taiwan. As a result, the subsequent systems, M3 and M4, were of diminished scale compared to the early ones. Therefore, in this section, the vertical structures of M1 at 0840 UTC and M4 at 1300 UTC are examined and compared by analyzing

three vertical cross sections for each case. The locations of these cross sections are indicated in Fig. 4.18.

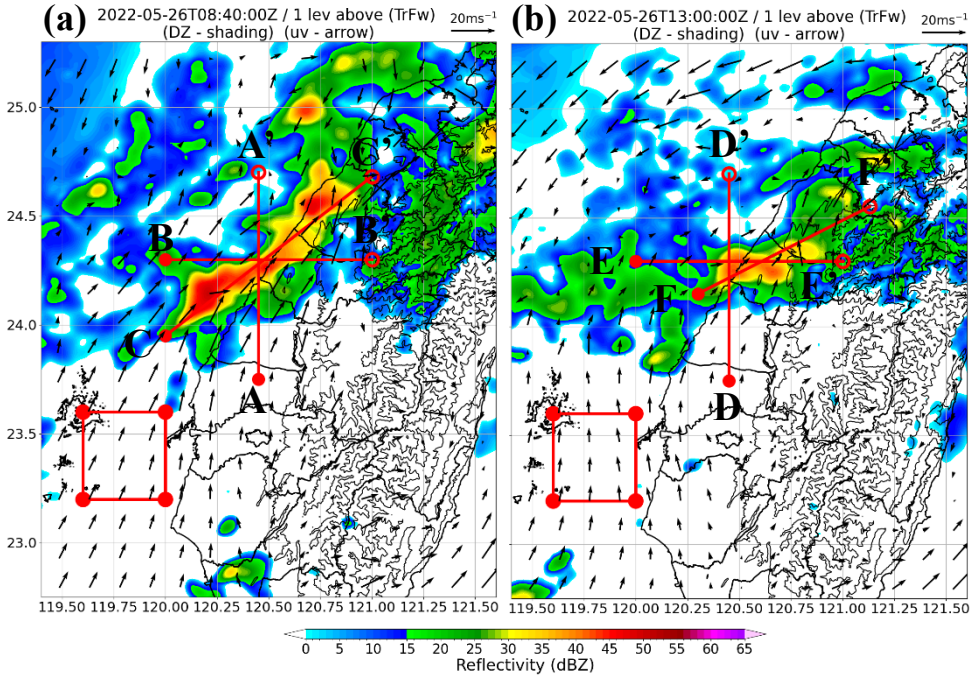

Figure 4.18. Terrain-following reflectivity fields overlaid with wind fields at (a) 0840 (M1) and (b) 1300 (M4) UTC 26 May 2022, respectively. Red lines in (a) and (b) correspond to the locations of the vertical cross sections. Red box indicates the region used for averaging to obtain the background wind fields.

4.2.3.1 Merged cell M1 at 0840 UTC

The south–north-oriented vertical cross section of reflectivity and convergence fields (Figs. 4.19a and 4.19b) shows that outflows generated by a cold pool between 50 and 60 km (associated with near-surface downdrafts, divergence, and cold air) encountered the prevailing southwesterly winds. This interaction formed a convergence zone (denoted by the red circle), which in turn concentrated water vapor flux along the southern edge of the convective cell.

In the east–west-oriented vertical cross section, a similar configuration of outflows and convergence zones was observed at the western side of convective cell (Fig. 4.19d). Notably, the moisture transport appeared more concentrated over the land between 60 and 80 km than over the ocean (Fig. 4.19c), suggesting that the moist air was channeled between the

mountainous terrain and convective cells. This configuration likely created a corridor that enabled northward moisture transport by the southwesterly flow.

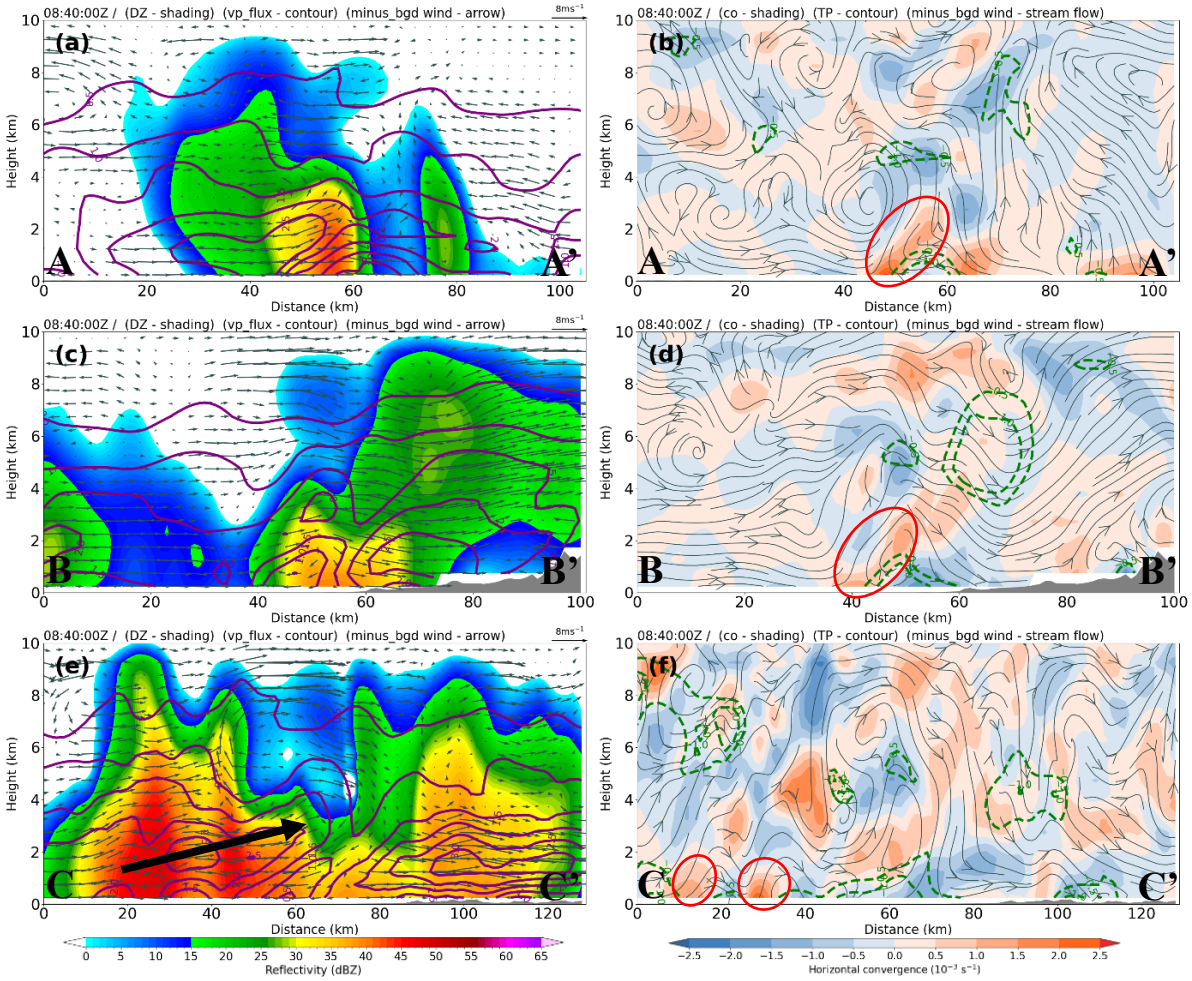

Figure 4.19. (a), (c), and (e) show vertical cross sections of reflectivity overlaid with purple contour lines of water vapor flux (starting from $0.5 \times 10^2 gkg^{-1}ms^{-1}$ *with an interval of* $0.5 \times 10^2 gkg^{-1}ms^{-1}$*) and wind fields relative to the background wind fields along cross sections A–A', B–B', and C–C' at 0840 UTC 26 May 2022, respectively. (b), (d), and (f) show the corresponding vertical cross sections of convergence overlaid with green dashed contour lines of temperature perturbation at −0.5 and −1.0 K and background-wind-relative streamlines.*

The southwest–northeast-oriented vertical cross section (Fig. 4.19e and 4.19f) reveals that outflows originating near 20 km collided with both the southwesterly winds at its western side and outflows near 40 km, leading to two significant convergence zones. This intensified the southwestern portion of M1. Additionally, the moisture transport within M1 was substantial due to the LLJ (see Figs. 4.8c and 4.9c), with water vapor flux exceeding $3.0 \times 10^2 gkg^{-1}ms^{-1}$,

and a northward slant. This illustrates the northward moisture supply to the convective system (highlighted by the black arrow).

3-D figure (view toward Taiwan from the southwest over the sea) shown in Fig. 4.20 illustrates that the winds rotated clockwise with height, indicating warm advection associated with warm, moist southwesterly flow. Additionally, the maximum height of 40-dBZ regions was observed to exceed 5 km, depicting a deep convective structure.

These findings suggest that M1 was able to maintain a broad, linear, and deep convective structure, driven by a combination of external and internal factors.

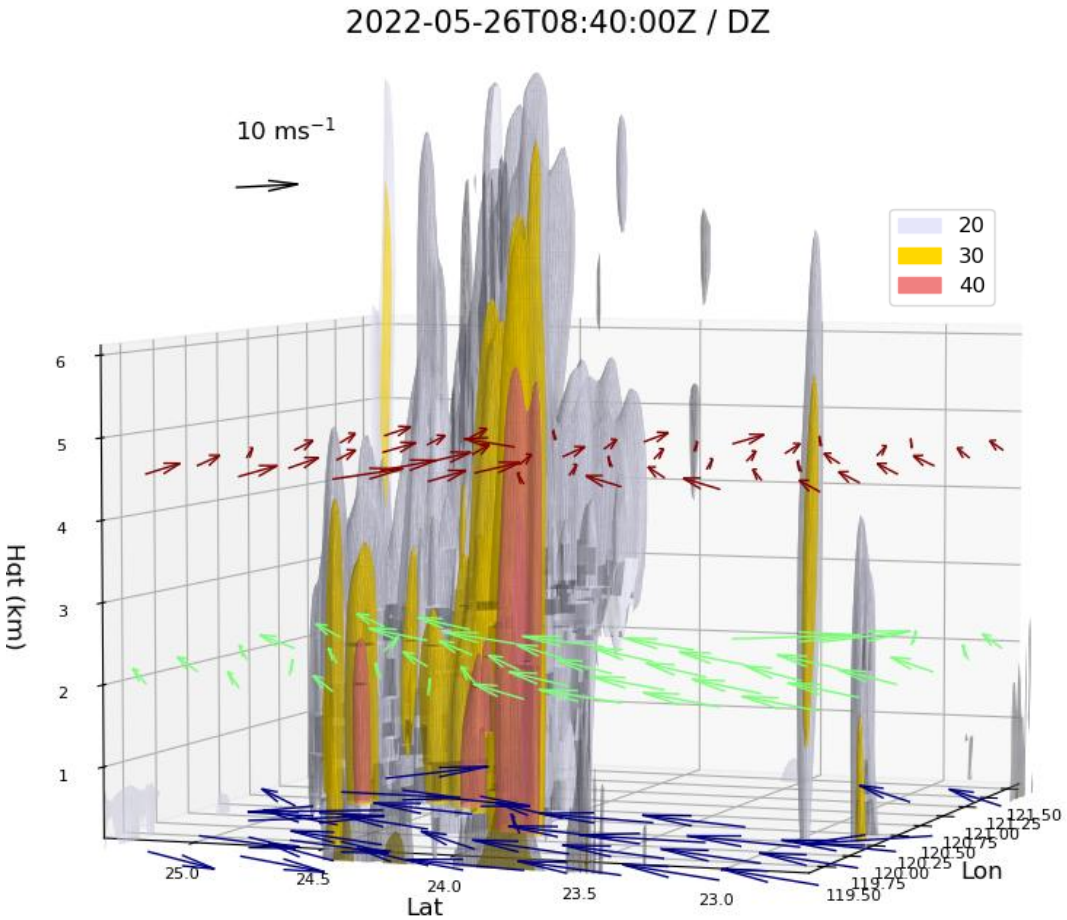

Figure 4.20. 3-D reflectivity field at 0840 UTC 26 May 2022, where lavender, gold, and light coral shading represent 20, 30, and 40 dBZ, respectively. Horizontal wind fields at 0.25 (blue arrows), 2.25 (green arrows), and 4.75 (red arrows) km are overlaid.

4.2.3.2 Merged cell M4 at 1300 UTC

At later stage, the south–north-oriented and east–west-oriented vertical cross sections (Fig. 4.21a to 4.21d) show the formation of convergence zones (outlined by the red circles) induced by outflows along the windward sides of the convective cells as well, consistent with the pattern at 0840 UTC. However, the water vapor flux weakened, primarily due to the diminishing southwesterly winds (see Figs. 4.13b and 4.15b). The east–west orientation of the convective cells (Fig. 4.21c) impeded northward moisture transport due to the formation of the convective cell inland.

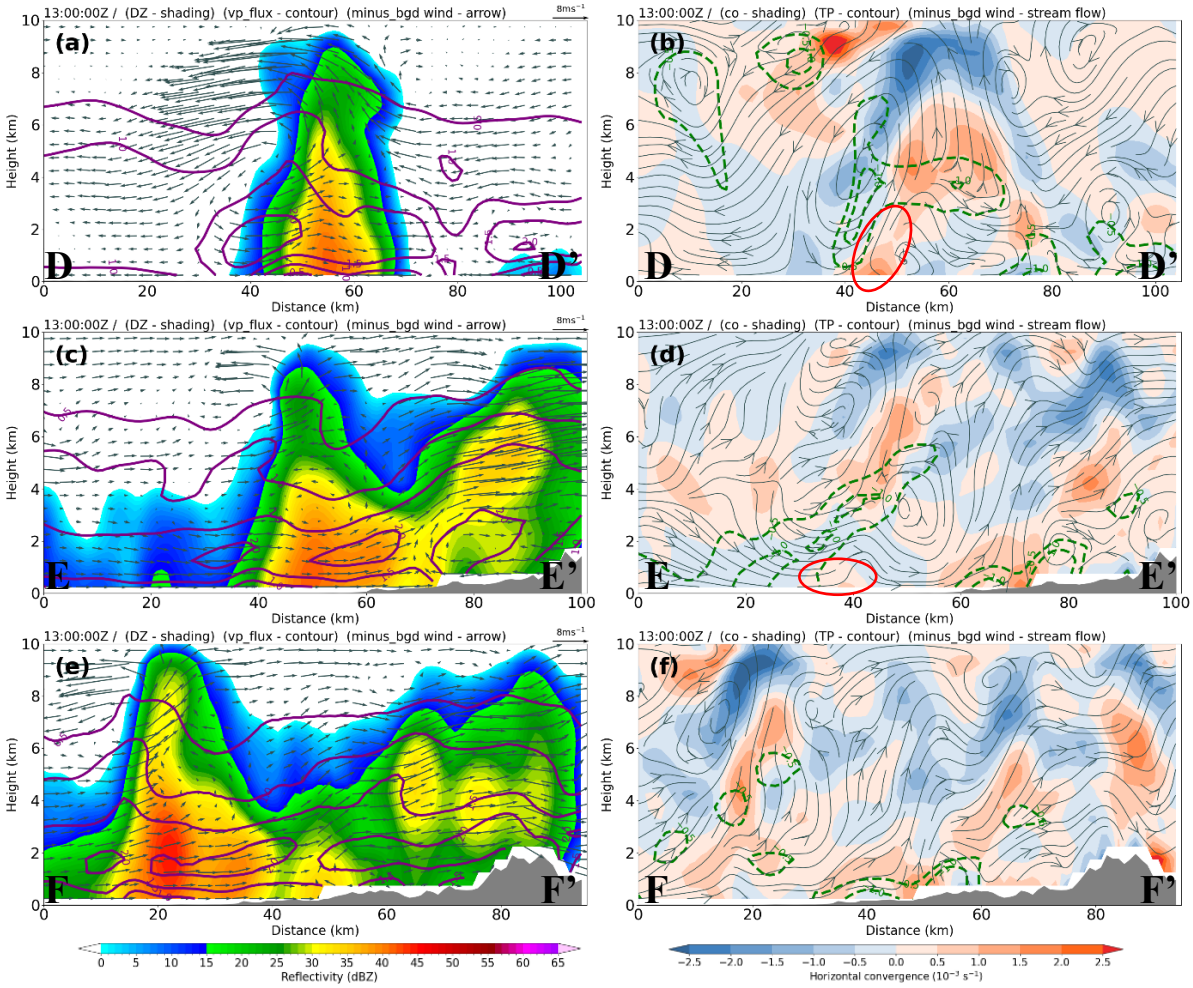

Figure 4.21. Same as Fig. 4.19, but for cross sections of D-D', E-E', and F-F' at 1300 UTC 26 May 2022.

As shown in Fig. 4.13, the near-surface front remained quasi-stationary over the Taiwan Strait, and the LLJ developed over the western slopes of the mountains. This caused high moisture transport to become concentrated inland (see Fig. 4.15), shifting favorable convective

conditions to inland accordingly. Correspondently, the development of convective cells was observed over inland, as shown in the southwest–northeast-oriented vertical cross section (Figs. 4.21e and 4.21f). 3-D figure shown in Fig. 4.22 illustrates a vertical structure similar to that observed at 0840 UTC. However, it is noteworthy that northeasterly winds dominated the northern regions at near-surface layer, where no convective cells developed. The maximum height of the 40-dBZ regions was lower than that observed at 0840 UTC, indicating relatively weaker convective intensity.

Compared to M1, the overall local conditions had become less favorable for widespread convective development, resulting in a localized-scale convective structure.

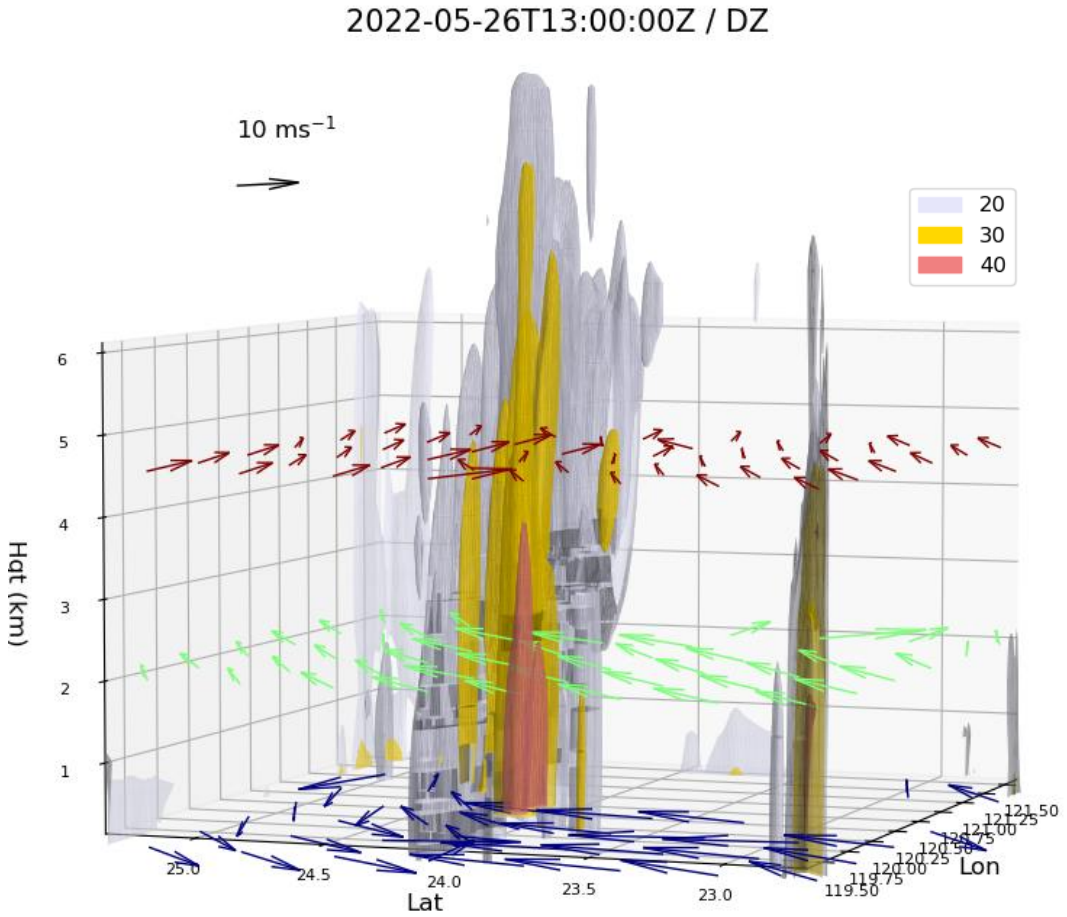

Figure 4.22. Same as Fig. 4.20, but at 1300 UTC 26 May 2022.

4.3 Local conditions in Central Taiwan

As upstream convective cells approached central Taiwan and merged with pre-existing downstream cells, the resulting merged cells intensified and persisted for roughly 1 to 2 hours. Therefore, this section aims to investigate the local conditions over central Taiwan to understand the factors that contributed to the sustained convective development in the region. This analysis is conducted by averaging the relevant fields within the area outlined by the red box in Fig. 4.23. Figure 4.24 illustrates that relatively strong convective development occurred prior to 1300 UTC, with the most intense activity observed between 0900 and 0930 UTC.

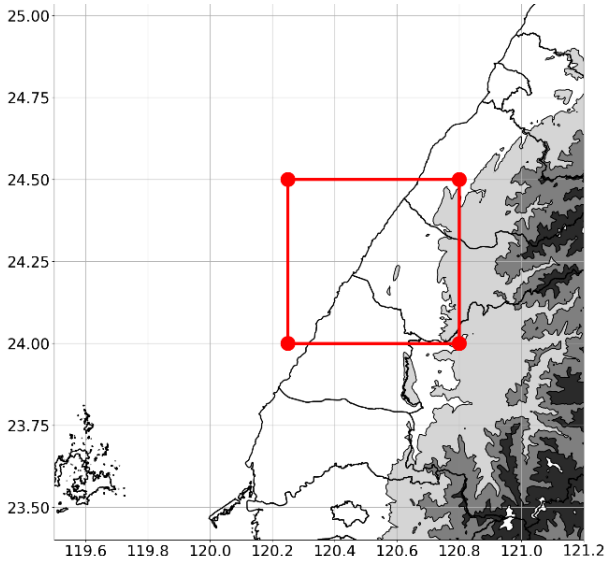

Figure 4.23. Red box indicates the region used to compute the area-averaged values for analyzing local conditions in central Taiwan.

Dynamically, the vertical wind shear (defined as the wind speed difference between 0.25 and 6 km) exceeded 13 ms^{-1} from 0820 to 1050 UTC, indicating relatively more favorable conditions throughout the analysis period (Fig. 4.25). Additionally, both of the hodographs at 0800 and 1400 UTC (Fig. 4.26) show predominantly northwesterly shear vectors, suggesting that newly developed convective cells, as they grew vertically, were advected eastward by the shear flow and subsequently blocked by the terrain. This interaction likely contributed to the quasi-stationary nature of the convective system over central Taiwan.

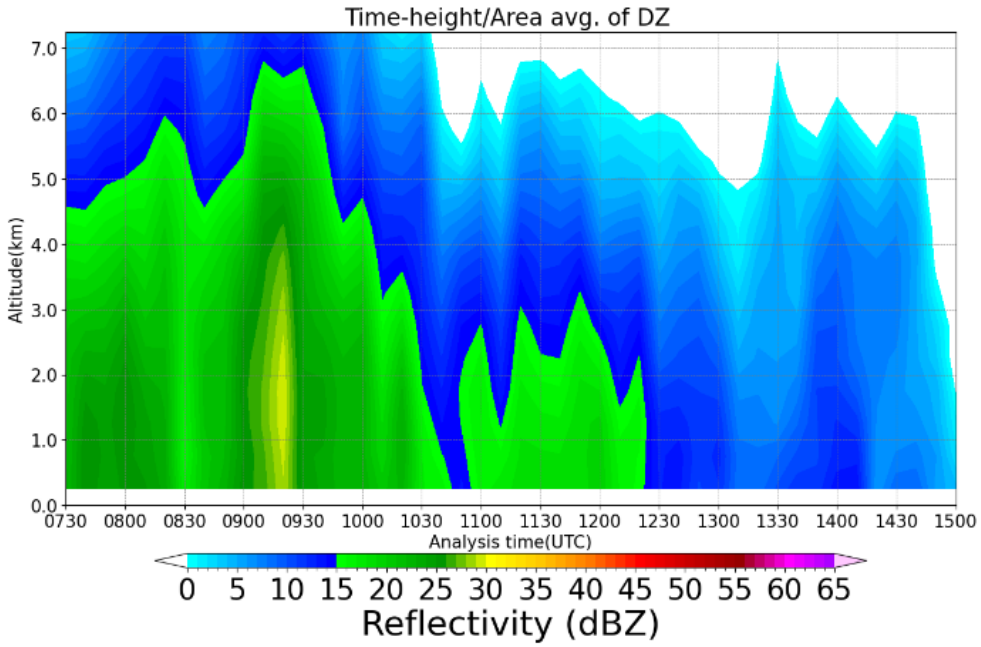

Figure 4.24. Time evolution of the area-averaged reflectivity with height within the red box shown in Fig. 4.23.

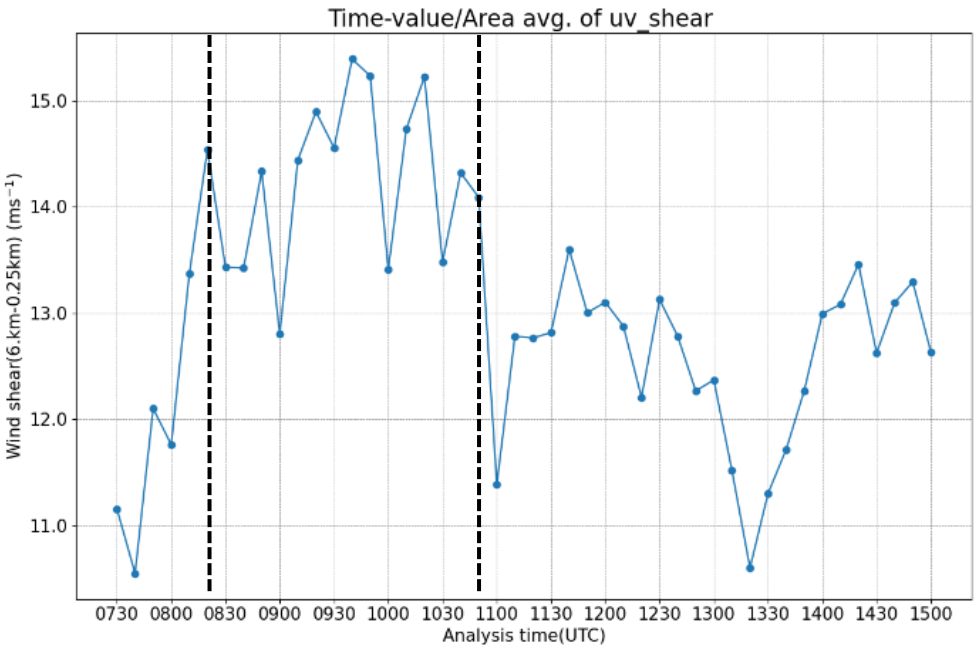

Figure 4.25. Time evolution of the vertical wind shear, calculated by subtracting the area-averaged wind speed at 0.25 km from that at 6.25 km within the red box shown in Fig. 4.23.

Thermodynamically, as shown in the KI field (Fig. 4.27), the environment was favorable for convective development, with KI values exceeding 35 K throughout the analysis period, particularly from 0730 to 0800 UTC and from 0900 to 1000 UTC. To further evaluate the characteristics of moisture transport, IVT was analyzed by averaging the IVT_x (defined in Eq.

4.1) along the eastern and western boundaries of the red box (shown in Fig. 4.23), and the IVT_y (defined in Eq. 4.2) along the southern and northern boundaries of the red box. The net IVT_x was derived by subtracting the eastern IVT_x from the western IVT_x (x-direction), and the net IVT_y was derived by subtracting the southern IVT_y from the northern IVT_y (y-direction). Results (Fig. 4.28) show that net IVT_y was notably higher, influenced by the LLJ channeled along the terrain. Both of the net IVT_x and net IVT_y remained positive before 1350 UTC, indicating efficient moisture supply to support convective development, as the outgoing IVT at the northern and eastern boundaries was lower than the incoming IVT at the southern and western boundaries.

In summary, the persistence of the convective cells over central Taiwan was supported by both dynamically favorable and thermodynamically unstable conditions, along with continuous moisture supply facilitated by terrain-enhanced transport.

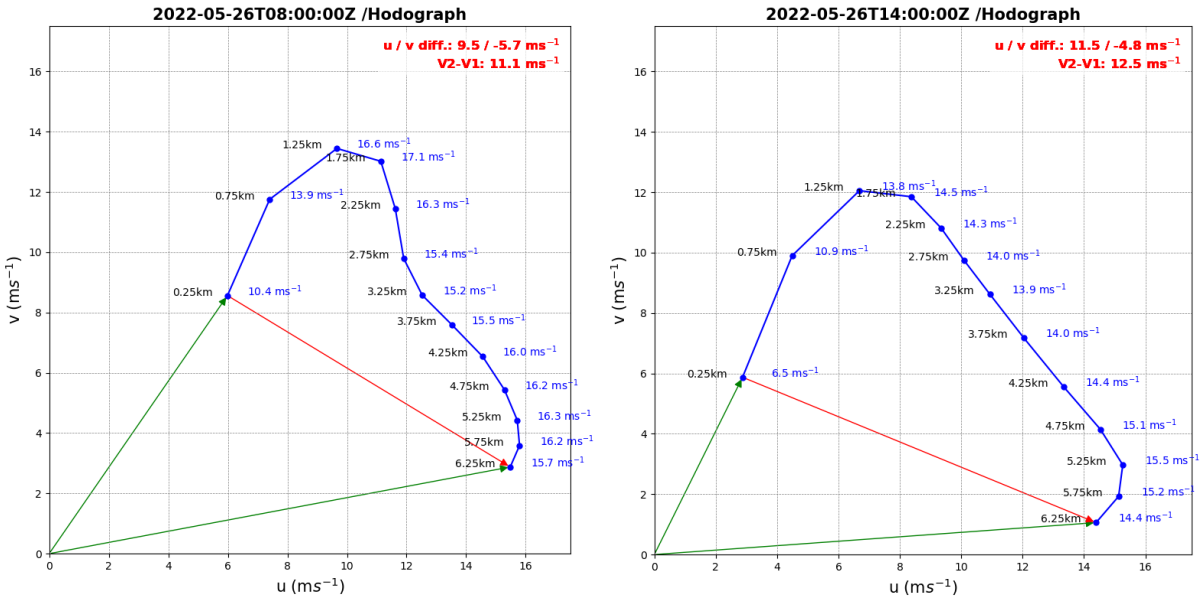

Figure 4.26. Hodograph constructed by averaging horizontal wind components (u, v) from 0.25 km to 6.25 km in height within the red box shown in Fig. 4.23.

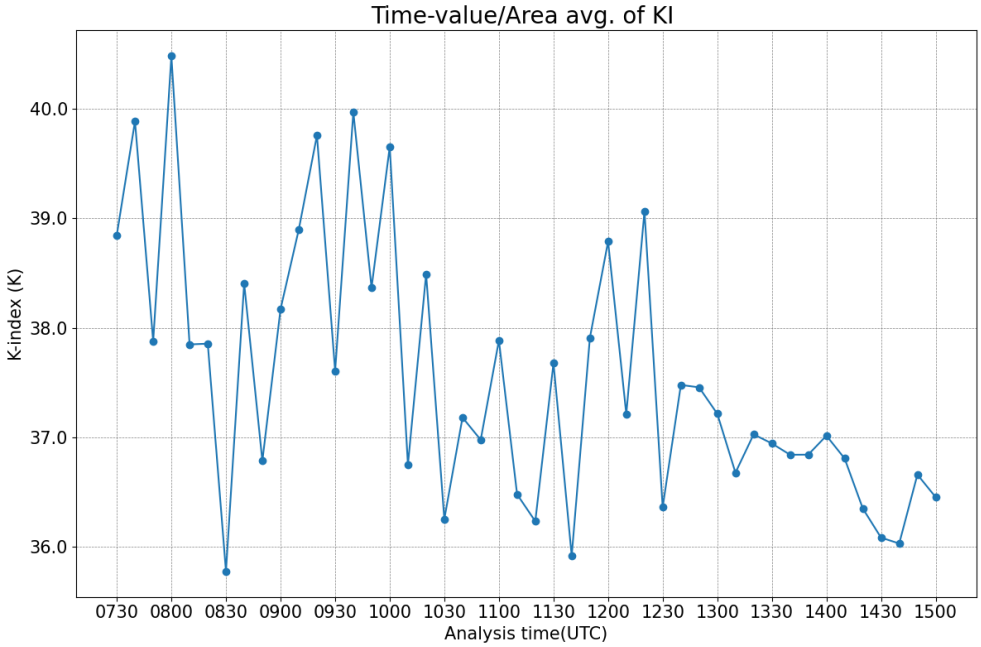

Figure 4.27. Time evolution of the area-averaged KI within the red box shown in Fig. 4.23.

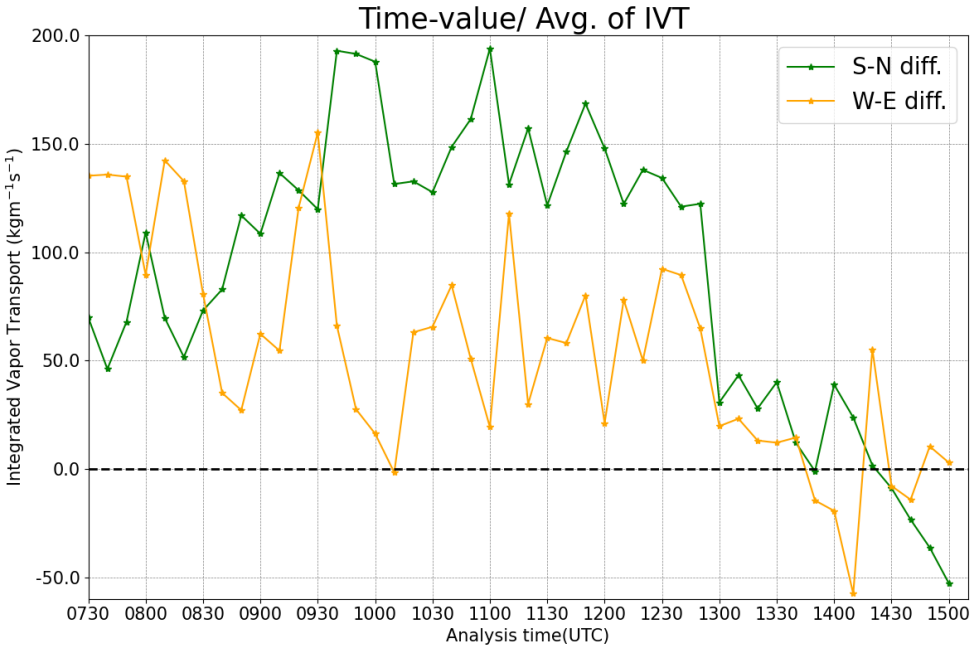

Figure 4.28. Time evolution of the net IVT_x (yellow line) and net IVT_y (green line).

4.4 Low-level jet

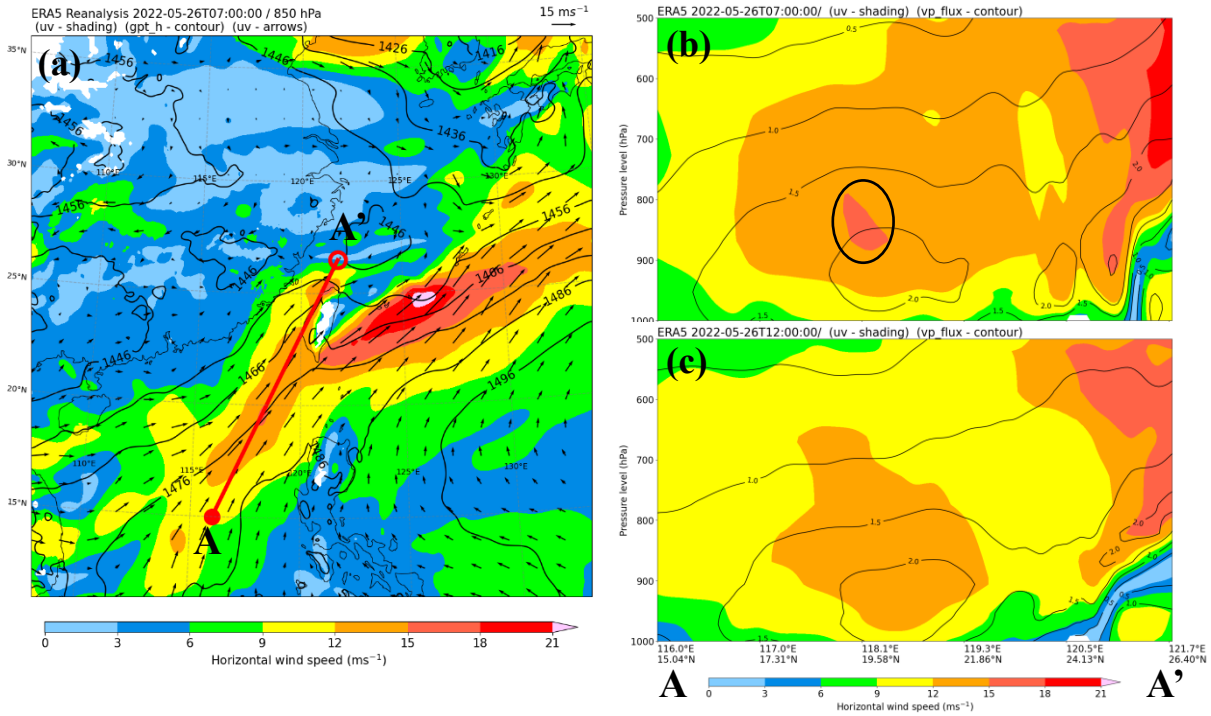

Figure 4.29. (a) represents the 850-hPa weather map with shading indicating horizontal wind speed, overlaid with contour lines of the geopotential height (unit: meter) and wind arrows. (b) and (c) show vertical cross sections of horizontal wind speed (shading) and water vapor flux (contour lines; unit: $10^2 gkg^{-1}ms^{-1}$) along the red line marked in (a) at 0700 and 1200 UTC, respectively.

As shown in Fig. 4.29, a SLLJ was originated over the South China Sea and extended northeastward across the Taiwan Strait and into the sea east of Taiwan. The vertical cross section at 0700 UTC (Fig. 4.29b) reveals that the jet core (denoted by the black circle) was located between 800 and 900 hPa (approximately 1 to 1.5 km), accompanied by substantial moisture transport (exceeding 200 $gkg^{-1}ms^{-1}$) toward Taiwan. At 1200 UTC, the SLLJ appeared to weaken (Fig. 4.29c), correspondent with the gradual weakening of the southwesterly winds as previously mentioned. Details of the LLJ over Taiwan are further revealed by IBM_VDRAS plotting the vertical cross sections along A-A' and B-B' and calculating the momentum equation along the lines shown in Fig. 4.30. The west–east vertical cross sections at 0730 UTC reveal that southwesterly winds decelerated as they moved inland and encountered the mountains (Fig. 4.31a), resulting in mass accumulation and convergence along the windward slopes (Fig. 4.31b).

This process contributed to the formation of high-pressure regions on the windward sides and low-pressure regions on the leeward sides (Fig. 4.31c). Consequently, the southwesterly flow was deflected northward (Fig. 4.31d). Given the presence of a localized high-pressure system to the southern Taiwan, the south–north vertical cross section of the pressure perturbation at 0730 UTC (Fig. 4.32a) indicate the existence of a northward-directed horizontal pressure gradient force. Additionally, a pronounced LLJ with the speed of jet core exceeding 21 m s^{-1} was observed near 1.25 km altitude (marked by the black circle in Fig. 4.32b), contributing to substantial moisture transport exceeding 350 $gkg^{-1}ms^{-1}$ below the jet core over central Taiwan (Fig. 4.32c).

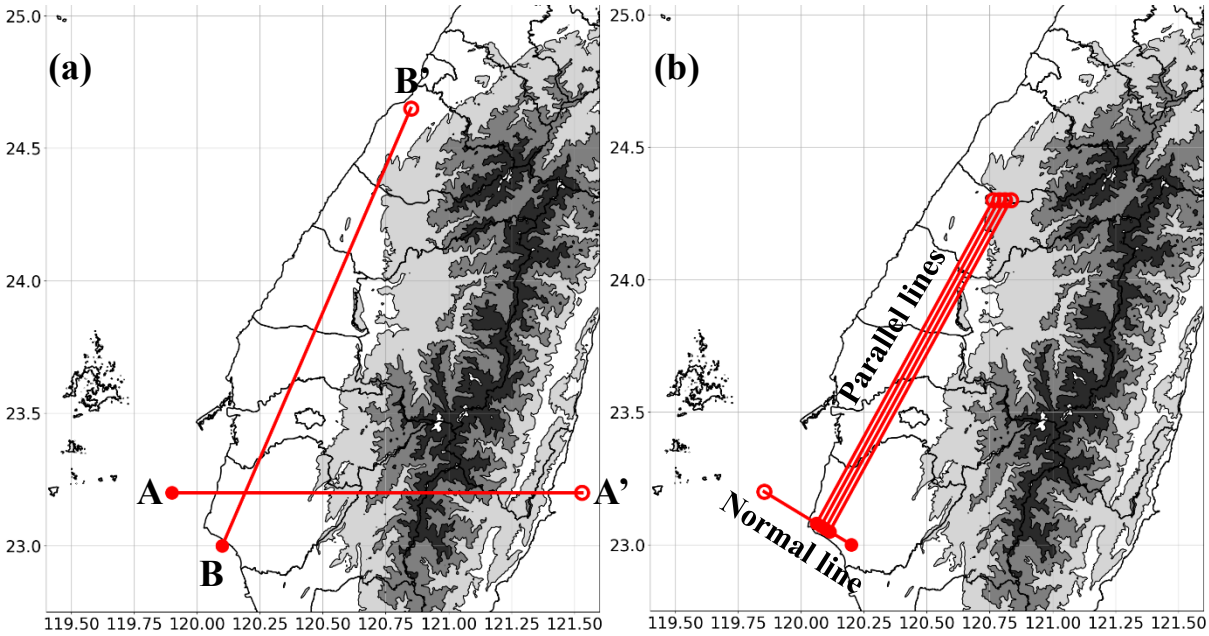

Figure 4.30. (a) shows two lines of the vertical cross sections. (b) shows the 4 parallel lines and their corresponding normal (perpendicular) line for calculating the momentum equation.

According to Li and Chen (1998), the momentum equation can be similarly written in natural coordinate system as

$$\frac{Dv_s}{Dt} = -\frac{1}{\rho}\frac{\partial P}{\partial s} + fv_n + R, \qquad (4.5)$$

where v_s and v_n represent the wind components parallel and normal to lines marked in Fig. 4.30b. The Coriolis parameter f is assumed to be $5.9 \times 10^{-5}\ s^{-1}$. The left-hand side denotes

acceleration, while the three terms on the right-hand side represent the pressure gradient force, Coriolis force, and residual, respectively. This equation provides a simplified assessment of which term on the right-hand side exerts the most significant influence on the acceleration of v_s. Before estimating each term of Eq. (4.5), Rossby number R_o is used in scale analysis to determine whether the Coriolis force needs to be considered in this equation. It is defined as:

$$R_o = \frac{\left|\frac{Dv_s}{Dt}\right|}{|fv_n|} = \frac{{v_s}^2/L}{f_0 v_n}. \qquad (4.6)$$

The Rossby number in this study is approximately 10, indicating that the Coriolis force on the right-hand side of Eq. (4.5) is relatively small compared to the acceleration term and can thus be neglected. As a result, the Eq. (4.5) is simplified to include only three terms.

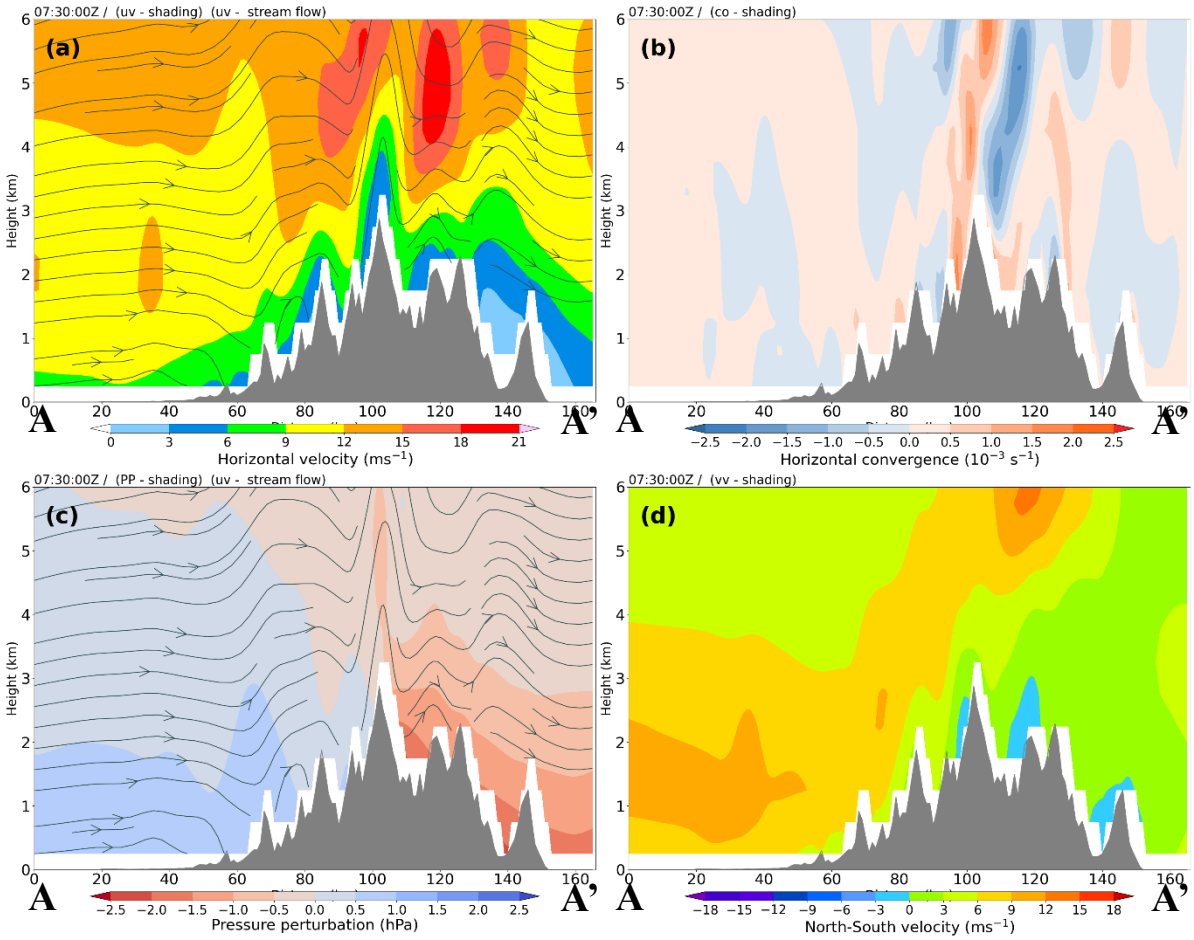

Figure 4.31. Vertical cross section along A-A' marked in Fig. 4.30a at 0730 UTC 26 May 2022. (a), (b), (c), and (d) stand for horizontal wind speed overlaid with streamlines, horizontal convergence, pressure perturbation overlaid with streamlines and north-south wind velocity, respectively.

The results of each term in momentum equation (see Table 1) indicate that the acceleration

term was comparable in magnitude to the pressure gradient force at 0.75 and 1.25 km heights. Additionally, the v_n values at these two levels were significantly lower than at 2.25 km, suggesting that the LLJ was likely driven by terrain-induced horizontal pressure gradient force, and it mainly flowed parallel to the terrain. Furthermore, the strongest v_s, associated with wind speed of 15.56 ms^{-1}, appeared at 1.25 km, corresponding to the jet core height, as shown in Fig. 4.32b. These results indicate that the LLJ was a barrier jet triggered orographically that transported abundant moisture.

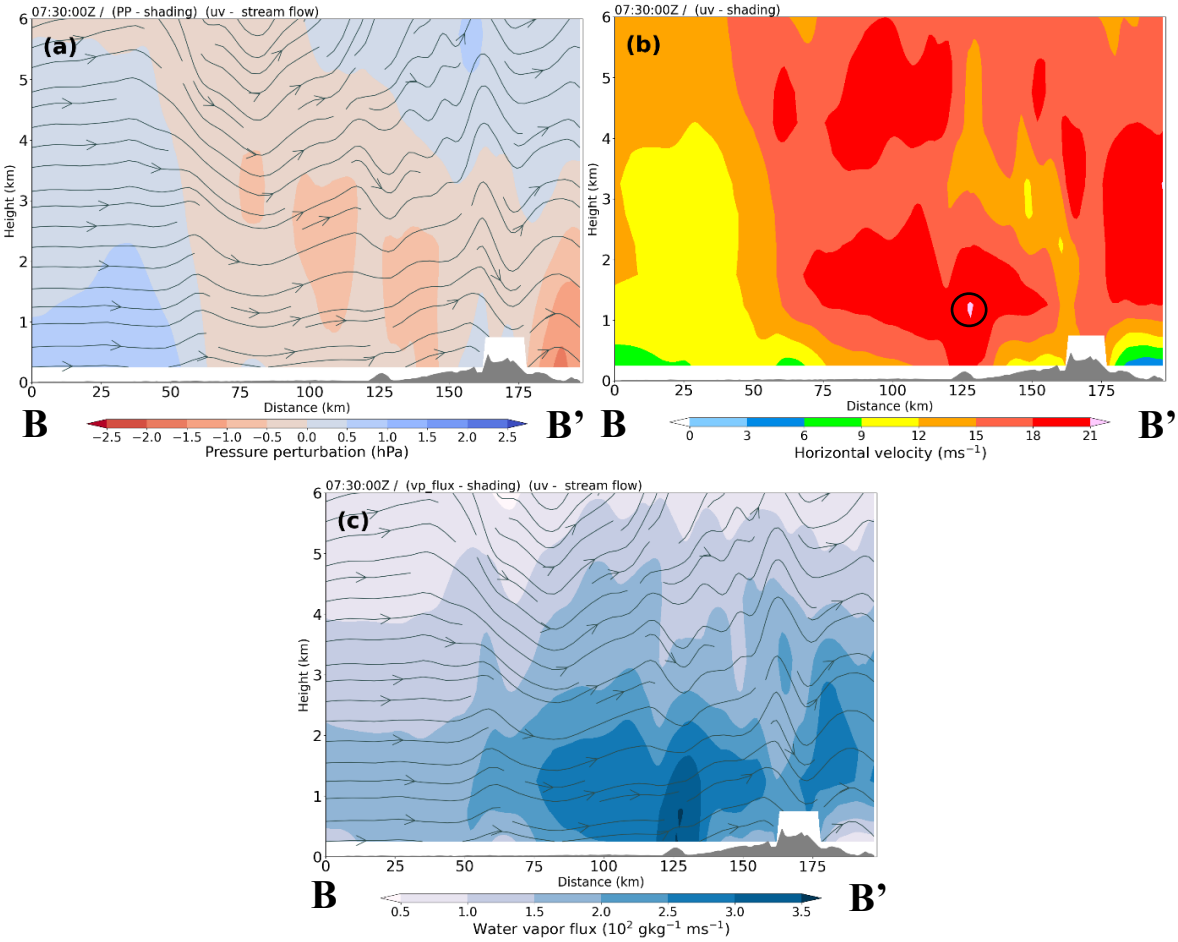

Figure 4.32. Vertical cross section along B-B' marked in Fig. 4.30a at 0730 UTC 26 May 2022. (a), (b), and (c) stand for pressure perturbation overlaid with streamlines, horizontal wind speed, and water vapor flux overlaid with streamlines, respectively. Black circle in (b) indicates the jet core.

Table 1. Estimated results of Eq. (4.5), with the Coriolis force term neglected. Each value is obtained by averaging the results calculated along the four parallel lines aligned with the same normal line, as shown in Fig. 4.30b. Overbar denotes the average along the distance, while the delta symbol (Δ) represents the averaged difference between the start and end points of four parallel line.

	Altitude (km)		
Parameters	0.75	1.25	2.25
$\overline{v_n}$ (ms^{-1})	0.80	-1.00	-2.83
$\overline{v_s}$ (ms^{-1})	13.59	15.56	14.91
Δv_s (ms^{-1})	8.89	8.29	5.03
ΔP (Pa)	-15.14	-36.39	-85.97
$\frac{Dv_s}{Dt}$ $(10^{-4}\, ms^{-2})$	1.58	3.05	3.91
$-\frac{1}{\rho}\frac{\Delta P}{\Delta s}$ $(10^{-4}\, ms^{-2})$	0.86	2.15	5.60
R $(10^{-4}\, ms^{-2})$	0.72	0.90	-1.69

4.5 Sensitivity experiment

Given that the terrain can induce LLJs, influence the advancement of near-surface fronts, and affect moisture transport, which ultimately impacts the development of convection, a sensitivity experiment was conducted to evaluate these effects, as detailed in Table 2. The forecast using the original topography served as the control run (hereafter referred to as CONT), whereas a sensitivity run was configured with terrain elevation over Taiwan uniformly reduced to 0 meter (hereafter referred to as w/o_TER).

Table 2. Configuration of the sensitivity test. CONT and w/o_TER denote control run and sensitivity run, respectively.

Experiment	CONT	w/o_TER
Data assimilation	0742 – 0800 UTC 26 May 2022	
Forecast period	0800 – 1200 UTC 26 May 2022	
Terrain	Original topography	Reduced to 0 m over Taiwan

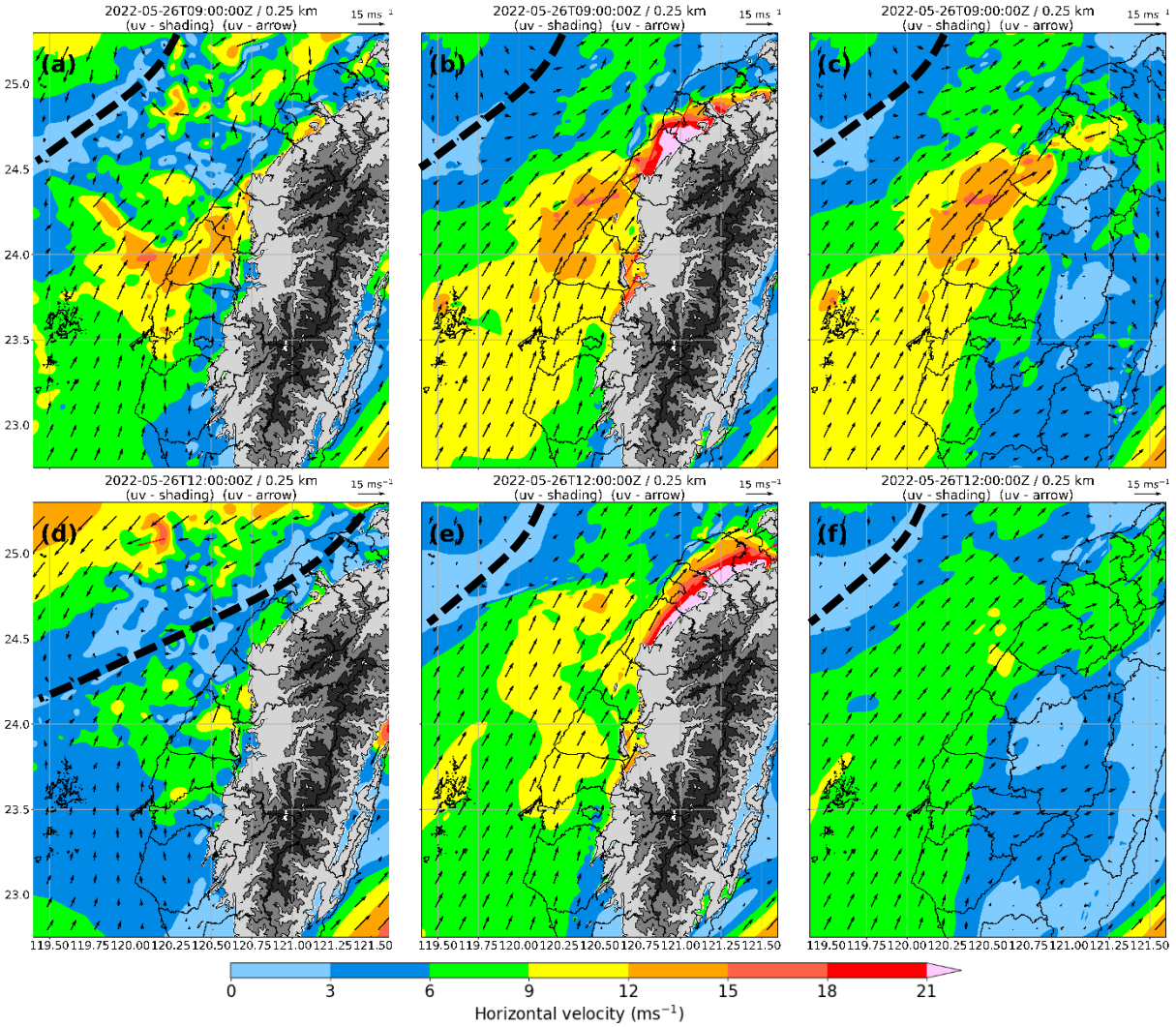

Figure 4.33. (a), (b), and (c) correspond to the 0.25-km wind fields at 0900 UTC 26 May 2022 from analysis field, CONT, and w/o_TER, respectively, whereas (d), (e), and (f) correspond to 0.25-km wind fields at 1200 UTC 26 May 2022 from analysis field, CONT, and w/o_TER, respectively. Red arrows stand for wind speeds exceeding 15 ms^{-1}. Black dashed line denotes the front.

Both forecast runs started carrying out data assimilation at 0742 UTC, followed by a 4-hour forecast commencing at 0800 UTC. It is noteworthy that the initial conditions of both the CONT and w/o_TER at 0800 UTC incorporated information about the LLJ through data assimilation. This explains the presence of the LLJ in w/o_TER, despite the absence of terrain.

By comparing the wind fields at 0.25 km (Fig. 4.33), neither CONT nor w/o_TER could reproduce the southward movement of the near-surface front (denoted by the black dashed lines) with northeasterly winds to its north as observed in the analysis field. Consequently, southwesterly winds almost dominated over the Taiwan Strait in both of the CONT and

w/o_TER. It can be seen that southwesterly winds of CONT at northwestern mountain were significantly accelerated and exceeded 21 ms^{-1}. At higher level of 1.25 km, the LLJ (outlined by the red arrows) in CONT and w/o_TER was distributed further north (Figs. 4.34b, 4.34c, 4.34e, and 4.34f) as compared to that in the analysis field (Figs. 4.34a and 4.34d). Particularly, the LLJ in CONT exhibited the strongest intensity among all, demonstrating the acceleration induced orographically.

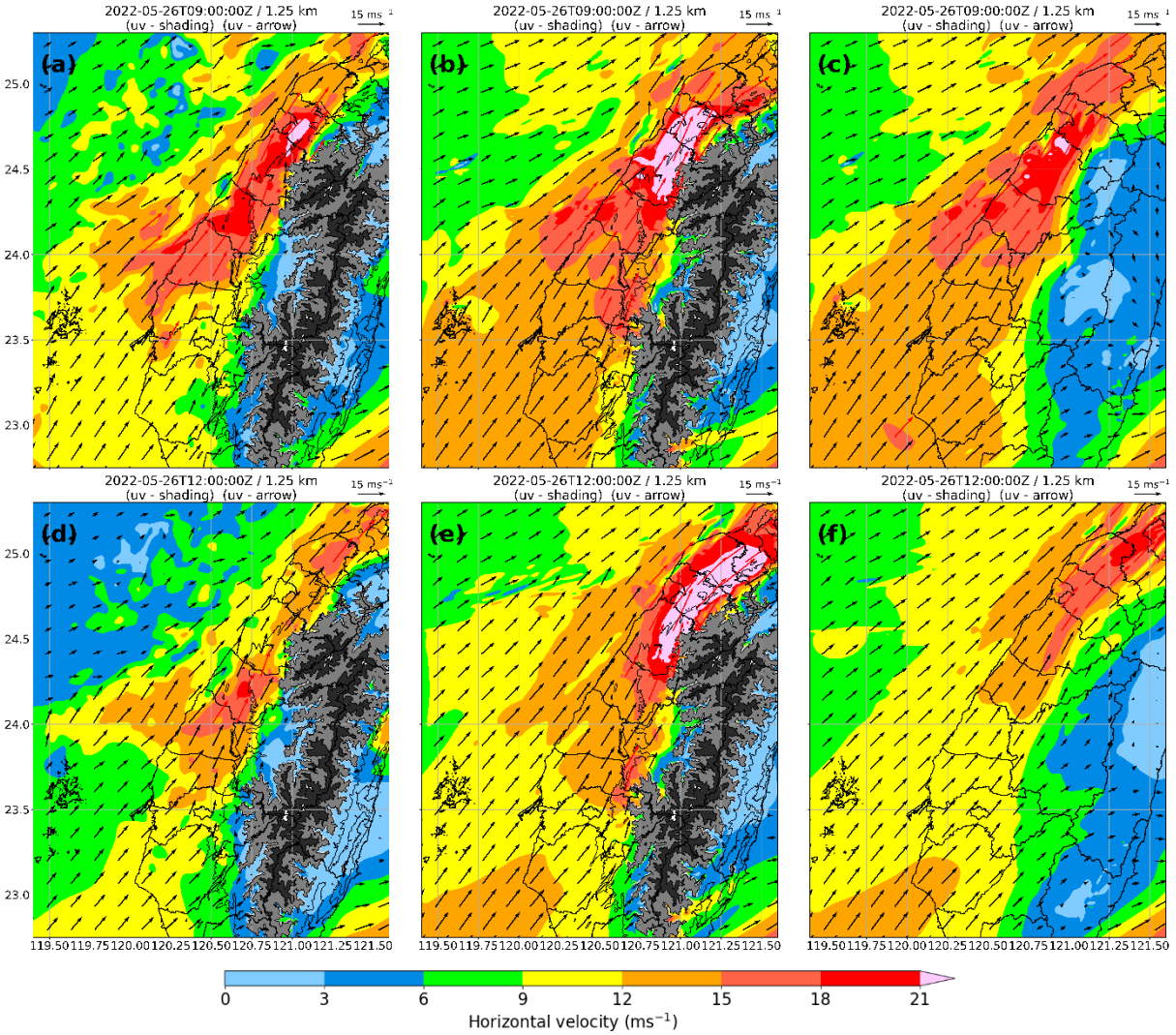

Figure 4.34. Same as Fig. 4.33, but for wind fields at 1.25 km altitude.

With respect to low-level moisture transport characteristics, the averaged low-level southwesterly winds within northern domain were stronger in magnitude in both forecasts (Figs. 4.35b, 4.35c, 4.35e, and 4.35f) relative to the analysis field (Figs. 4.35a and 4.35d). Thus, during

0900 to 1200 UTC, the low-level moisture transport in both forecasts was concentrated over northern Taiwan, whereas in the analysis field, low-level moisture transport was locked in central Taiwan.

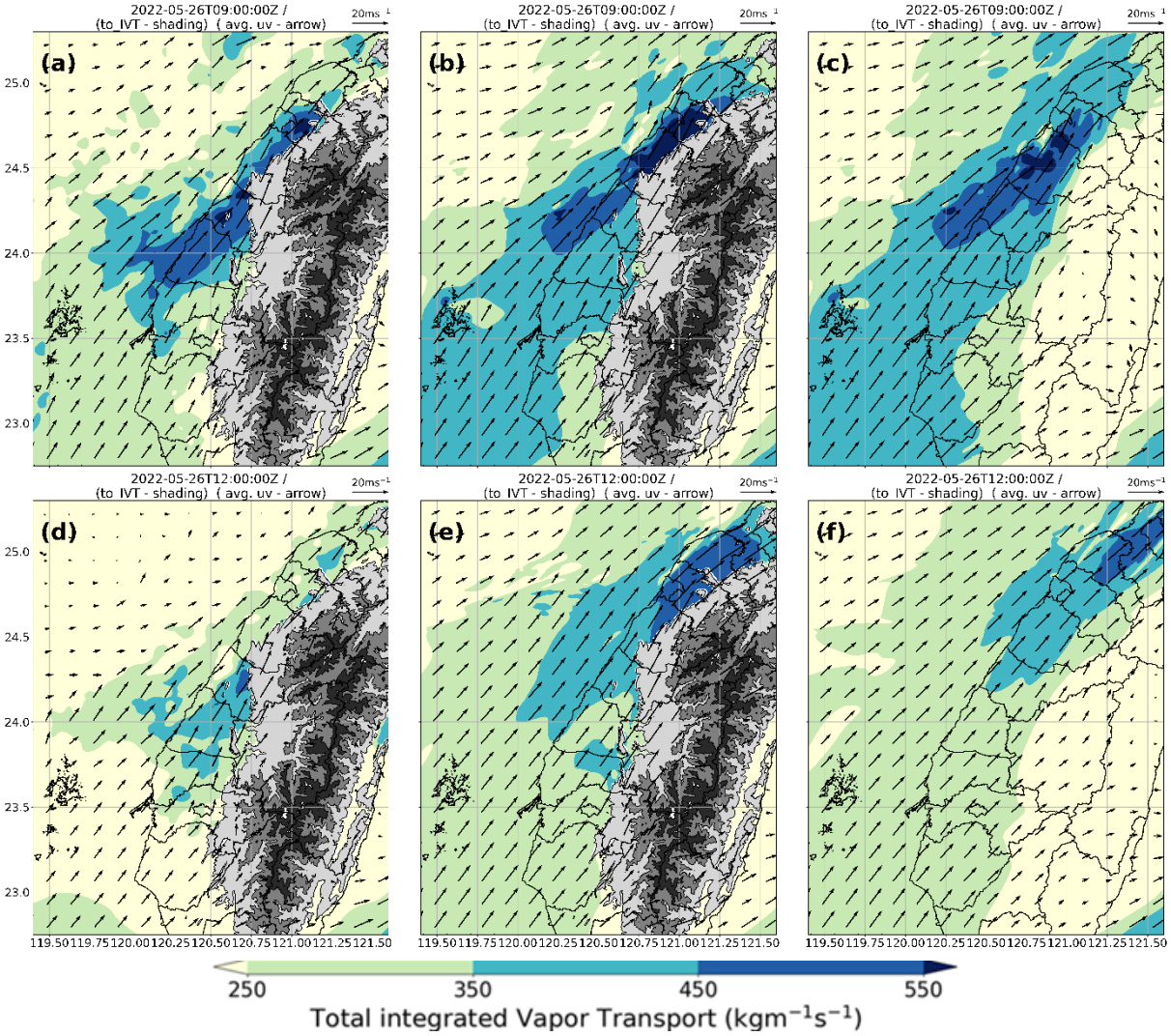

Figure 4.35. Shading indicates low-level IVT between 0.25 and 2.25 km. Wind arrows depict the averaged wind fields within the 0.25-2.25 km layer. (a), (b), and (c) correspond to fields at 0900 UTC 26 May 2022 from analysis field, CONT, and w/o_TER, respectively, whereas (d), (e), and (f) correspond to fields at 1200 UTC 26 May 2022 from analysis field, CONT, and w/o_TER, respectively.

In terms of the rainfall forecast, as shown in Fig. 4.36, both CONT and w/o_TER roughly captured the major precipitation regions as seen in observation, but both underestimated the rainfall intensities. When comparing rainfall patterns, CONT was clearly closer to the observation. Especially, the location and value of the maximum accumulated rainfall of CONT

were clearly closer to that of observation than that of w/o_TER. The maximum accumulated rainfall of CONT was located at the west of mountain, in contrast to w/o_TER, highlighting that terrain played a partial role in obstructing the progression of convective cells. In the absence of blocking effect generated by both of the near-surface front and terrain in CONT and w/o_TER, moisture was transported further north, resulting in more favorable conditions for convective development at the north. As a result, the convective cells developed over the northern Taiwan, leading to a decreased concentration of rainfall accumulation over central Taiwan.

It can be concluded that both the near-surface front and the terrain were crucial roles in blocking convection over central Taiwan, thereby contributing to prolonged convective development. Additionally, the acceleration of southwesterly winds was found to be induced by a northward horizontal pressure gradient force generated through orographic effects, as discussed in previous section.

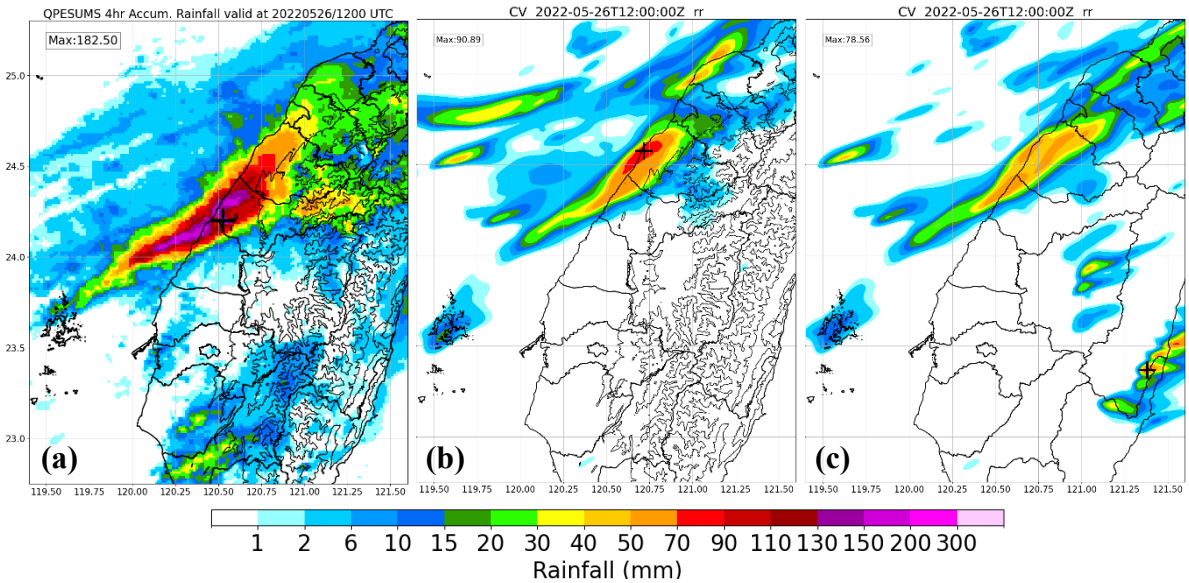

Figure 4.36. 4-hr (0800-1200 UTC) accumulated rainfall from (a) QPESUMS, (b) CONT, and (c) w/o_TER. The cross symbol denotes the location of the maximum 4-hr accumulated rainfall.

Chapter 5 Summary, conclusions and future work

5.1 Summary and conclusions

In this study, the extreme rainfall event on 26 May 2022 was investigated using the rapid-update IBM_VDRAS by assimilating 7 radars covering almost the whole MCS. Local factors contributing to this event were revealed by high-spatiotemporal-resolution analysis fields. Before analyzing the event, to address the underestimation of the rainwater mixing ratio estimated by the original relation in IBM_VDRAS, new localized relations were applied. The results show that the revised relations yielded a higher maximum rainwater mixing ratio and demonstrated better agreement with observations.

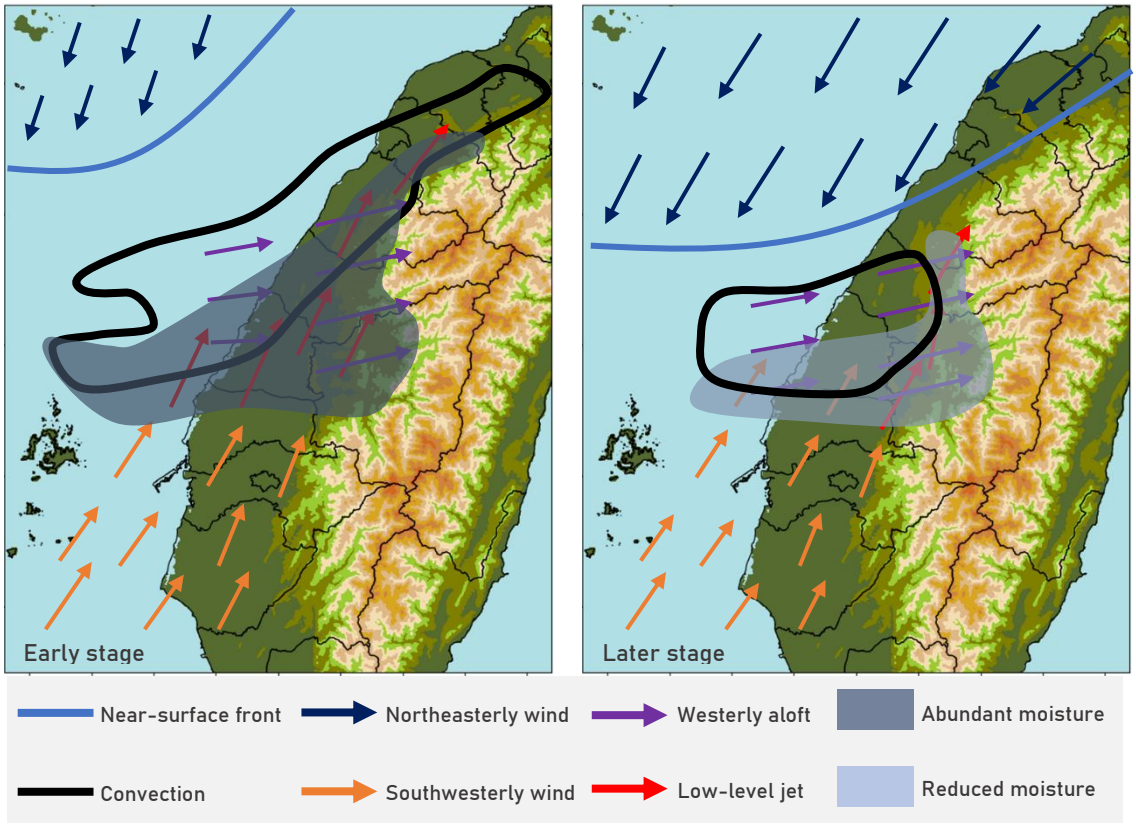

Figure 5.1. Schematic diagram illustrating the evolution of the MCS event.

Our results indicate that multi-scale key factors played crucial roles in the formation of this MCS: large-scale Mei-Yu front and monsoonal southwesterly flow, local-scale blocking

effect and barrier jet, and storm-scale back-building process. The MCS event is conceptualized through the schematic diagram shown in Fig. 5.1 and other findings are summarized as follows:

1. During the early stage, strong southwesterly winds prevailed, and a LLJ developed over central Taiwan, transporting abundant moisture, while a near-surface front was positioned northwest of the island.
2. The orientation of the convection was primarily from northeast to southwest, forming a corridor between the terrain and convective cells that facilitated northward moisture transport.
3. With convergence zones forming on the windward sides of the convective cells and a continuous moisture supply, widespread convective development was sustained.
4. During the later stage, the southwesterly winds gradually weakened, accompanied by a weakening LLJ and a southward advancement of the near-surface front. Accordingly, the moisture supply reduced, with the cold air intrusion of the front.
5. As convection became oriented more east–west, northward moisture transport was inhibited due to the interception by convective system over central Taiwan, resulting in an unfavorable environment for convective development over northern Taiwan.
6. The convective development was eventually shifted southward to central Taiwan and became smaller scale.
7. The local conditions over central Taiwan were both dynamically and thermodynamically favorable for convective development. Notably, vertical wind profiles exhibited clockwise rotation, indicating that once convection developed vertically, it tended to be advected eastward and subsequently blocked by the mountainous terrain. The LLJ observed over central Taiwan appeared to be a barrier jet transporting substantial moisture.
8. The sensitivity experiment indicates that both the near-surface front and the terrain exerted a blocking effect, obstructing convective cells from advancing northward and causing

them to remain over central Taiwan. The acceleration of southwesterly winds over central Taiwan appeared to be driven by a northward-directed horizontal pressure gradient force generated through orographic processes.

The back-building process was successfully reproduced in this study. New convective cells merged with preceding cells downstream, and the resulting merged cells were further intensified and sustained through both external and internal interactions. Wang et al. (2016) analyzed a back-building MCS that developed over northern Taiwan during the approach of a Mei-Yu front, accompanied by a prefrontal low-level jet. Their study revealed that cold pools did not serve as a key factor in the initiation of new convection. A similar environmental configuration was observed in our case. Our results indicate that although the cold pools formed within convective cells, they were insufficient in strength to develop into persistent and enhanced mesoscale boundaries capable of initiating new convection. While the back-building process alone can generate intense localized precipitation, our findings demonstrate that the blocking effects induced by the front and terrain during this MCS event significantly amplified the rainfall concentration over central Taiwan, consequently triggering extreme precipitation in localized regions.

Through the complex interplay of multi-scale factors, a quasi-stationary, long-lived extreme rainfall event was ultimately triggered. To enhance the accuracy of quantitative precipitation forecasts (QPF) for similar MCS events in the future, it is essential to accurately capture the intricate multi-scale interactions, particularly the position and evolution of the near-surface front, the timing and intensity of the prevailing southwesterly flow, and orographic influences. Furthermore, the integration of high-resolution data assimilation can improve model forecasting capability by improving the representation of mesoscale features and moisture transport, thereby providing valuable guidance prior to the onset of extreme rainfall events.

5.2 Future work

1. According to previous studies, analysis fields generated after two assimilation windows with a short-term forecast inserted between them exhibit superior performance. Accordingly, in this study, IBM_VDRAS adopts this configuration to produce each analysis field. This approach also mitigates the risk associated with continuous cycling in IBM_VDRAS, where each newly generated analysis field serves as the first guess for the subsequent assimilation without interruption. Such a process is vulnerable to unexpected system failures that may necessitate a complete restart. However, this approach may introduce minor inconsistencies in the dynamic and thermodynamic structures between preceding and subsequent analysis fields. To address this limitation, a potential enhancement involves implementing continuous assimilation cycles from 0730 UTC to 1500 UTC, with 10-minute cycle (7.5-min assimilation followed by 2.5-min short-term forecast) for generating analysis fields. This configuration maintains the identical 10-minute temporal resolution while enabling verification of whether more consistent results can be achieved.
2. Increasing the vertical resolution from 0.5 km to 0.25 km is expected to yield more refined vertical information, including the detailed convective structures and the features of the shallow Mei-Yu front.
3. The barrier jet was investigated and found to be orographically induced by a horizontal northward-directed pressure gradient force, resulting from a locally high-pressure region on the windward side of the southern mountains and a locally low-pressure region over central Taiwan. The high-pressure region is inferred to be dynamically generated by mass accumulation. However, thermodynamic mechanisms can be further examined to assess their influence on the development of the high-pressure region and to determine whether dynamic or thermodynamic processes predominantly contribute to the formation of the local high-pressure

system.

4. This study primarily focuses on how multi-scale factors influenced the development of the MCS, rather than on the mechanisms that triggered convection during the event. Therefore, future research could investigate the triggering mechanisms of convection. In particular, it is worth examining why convection was repeatedly initiated at nearly the same upstream location and whether the back-building process could still occur in the absence of any one of the multi-scale factors identified in this study.

Appendix A

Radar data quality control (QC)

Prior to assimilating radar data into IBM_VDRAS, QC must be applied to each radar dataset to ensure the integrity of meteorological signals. In this study, most of the QC procedures are performed using the RAKIT (Radar kit) software developed by the Radar Meteorology Laboratory at National Central University (NCU), while additional QC methods are specifically developed for this study. The QC procedures applied are as follows:

- **TR**: Removes all data obstructed by terrain.
- **PR**: Removes data points where the co-polar cross-correlation coefficient (RhoHV, ρ_{HV}) falls below a defined threshold or the standard deviation of differential phase shift (PhiDP, Φ_{DP}) exceeds the threshold.
- **PU**: Unfolds the Φ_{DP}.
- **BV**: Identifies and removes radar beams contaminated by noise based on sign reversals in radial velocity. If more than 15% of valid data along a beam show positive-to-negative (or vice versa) sign changes with respect to distance, the beam is considered noisy and discarded.
- **SR**: Filters out sea clutter over the ocean when the absolute value of radial velocity is below 15 ms^{-1}, reflectivity is below 20 dBZ, and spectrum width is either less than 1 or greater than 8.
- **VU**: Unfolds the radial wind fields V_r.
- **VS**: Smooths the radial wind fields by comparing each gate's value with the local background. Specifically, the background radial velocity is calculated by averaging values near the target gate. If the absolute difference between the target gate's value and the background exceeds 5 m s^{-1}, the target value is replaced with the background

velocity.

- **RM**: Manually removes clutters and non-meteorological signals.
- **AC**: The attenuated reflectivity (Z) and differential reflectivity (ZDR) are corrected using

$$Z_H^{Corr} = Z_H^{obs} + A_H + Z_H^{bias} \quad \text{(A. 1)}$$

$$Z_{DR}^{Corr} = Z_{DR}^{obs} + A_{HV} + Z_{DR}^{bias} \quad \text{(A. 2)}$$

Here, A_H and A_{HV} represent the attenuation correction terms, where the coefficients α and β must be determined for A_H and A_{HV}, respectively. Z_H^{bias} and Z_{DR}^{bias} represent the system bias correction terms. Z_H^{Corr} and Z_{DR}^{Corr} are corrected values, while Z_H^{obs} and Z_{DR}^{obs} are observed values.

- **BC**: The system-biased reflectivity (Z) and differential reflectivity (Z_{DR}) are corrected by determining Z_H^{bias} and Z_{DR}^{bias} as used in Eqs. (A.1) and (A.2).
- **SN**: Since both convective and stratiform regions exhibit higher signal-to-noise ratios (SNR), as shown in Fig. A.1(b) and (c), data points with SNR, calculated from reflectivity, less than a specified threshold are removed, as they are not of interest in this study. According to Ryzhkov and Zrnic (2019), the SNR is derived using the following procedure:

1. **Create the pseudo noise field** $\hat{Z}$:

   Identify the minimum reflectivity at each gate (i.e., range or distance), marked by the red dots in Fig. A.1, and subtract 3 dBZ:

$$\hat{Z}(dis) = Z(dis)_{min} - 3 \quad \text{(A. 3)}$$

2. **Calculate the constant** *C*:

   Consider only data points beyond 20 km in distance. Subtract $20log(dis)$ from $\hat{Z}$, and compute the average of the resulting values:

$$C = avg\left(\hat{Z}(dis) - 20log(dis)\right), \quad \text{(A. 4)}$$

where $20\ km \leq distance \leq maximum\ scanning\ range.$

3. **Construct the estimated noise** Z_{noise}:

   Add $20log(gate)$ back to the C to obtain the estimated noise at each gate:

$$Z_{noise}(dis) = C\ + 20log(dis) \quad \text{(A. 5)}$$

4. **Compute the signal-to-noise ratio** *SNR*:

   Subtract the estimated noise from the observed reflectivity:

$$SNR(dis) = Z\ - Z_{noise}(dis) \quad \text{(A. 6)}$$

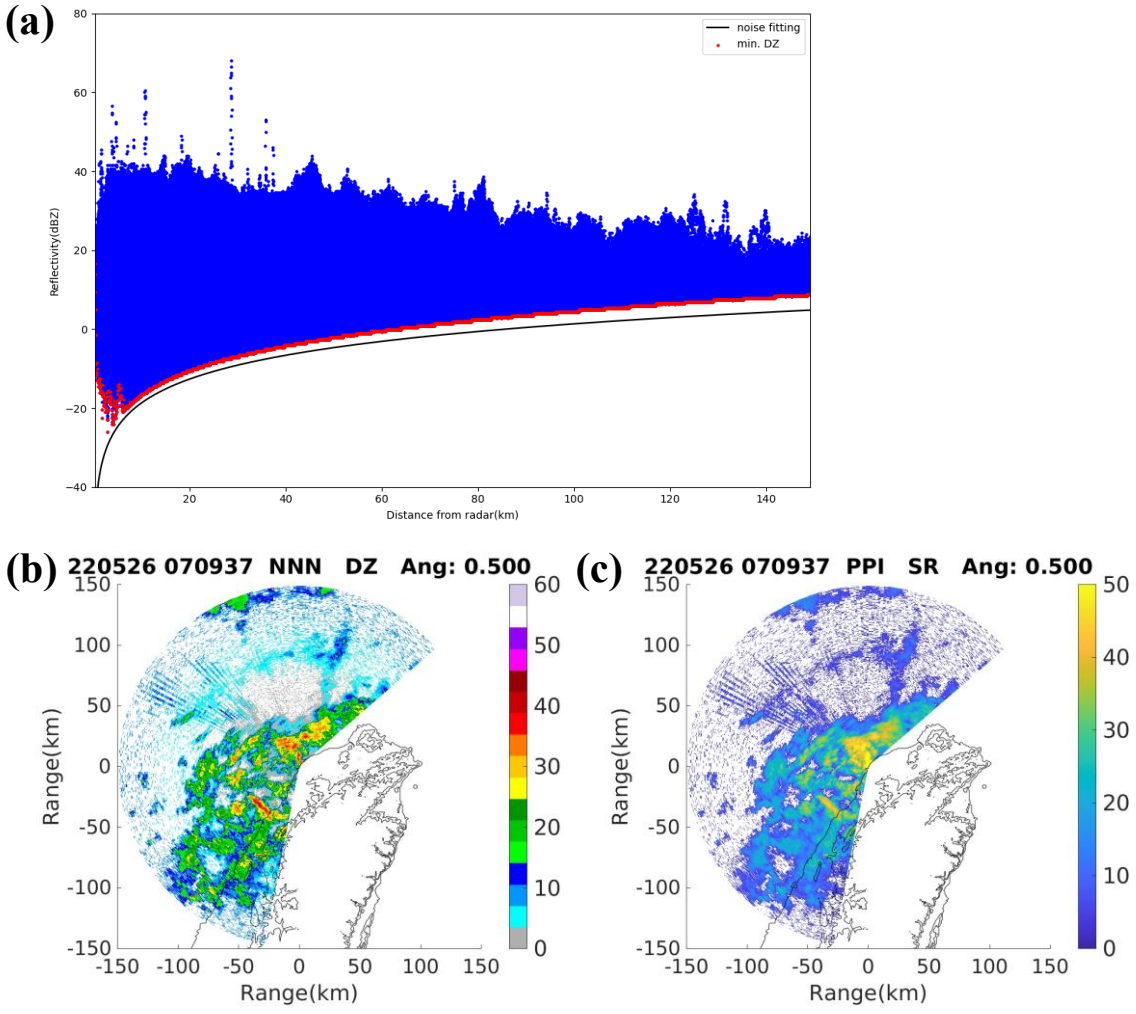

Figure A.1. (a) Reflectivity data are obtained from the TEAMR radar. Blue dots represent the reflectivity values at each gate along the distance from the radar across all elevation angles. Red dots indicate the minimum reflectivity at each gate along the distance. Black line represents the estimated noise curve. (b) Raw reflectivity field at 0.5 elevated angle from TEAM-R at 0709 UTC 26 May 2022. (c) SNR calculated from the raw reflectivity field at a 0.5° elevation angle at 0709 UTC 26 May 2022.

Before applying quality control (QC) to the NCAR S-POL radar data using RAKIT, the data had already undergone QC by the Earth Observing Laboratory (EOL) at NCAR and Colorado State University (CSU), ensuring that high-quality meteorological signals were retained. For the NCU TEAM-R radar data, prior to QC with RAKIT, azimuth angle misalignment was identified in the raw data, specifically discontinuities in the angle sequence. This issue was resolved by reordering the azimuthal angles to restore continuity and consistency. The attenuation correction coefficients used in RCMK follow Tang (2010). The QC procedures for each radar are summarized in Table A.1.

Table A.1. QC steps of each radar assimilated into the IBM_VDRAS.

Radar	QC steps
S-POL	TR → PR (RH=0.85 and S.T.D=10) → BV → RM (Remove V_r data corresponding to azimuth angles between 26° and 32°) → VS (only for lowest 3 elevated angles)
TEAM-R	SN (threshold=15) → TR → PU → PR (RH=0.8 and S.T.D=10) → BV → SR → AC ($\alpha = 0.264\ and\ \beta = 0.0373$) → SC ($Z_H^{Corr} = -4.71$ and $Z_{\mathrm{DR}}^{Corr} = -2.4950$) → VU → VS
RCSL	TR → PU → PR (RH=0.8 and S.T.D=10) → BV → VU → AC ($\alpha = 0.0197\ and\ \beta = 0.0023$)
RCWF	TR → PR (RH=0.85 and S.T.D=10) → BV → VU
RCNT	TR → PU → PR (RH=0.8 and S.T.D=10) → SR → BV → VU → VS → AC ($\alpha = 0.0197\ and\ \beta = 0.0023$)
RCMK	TR → PU → PR (RH=0.8 and S.T.D=10) → BV → AC ($\alpha = 0.054\ and\ \beta = 0.01$)
RCCG	RM (Remove V_r and Z data within a radial distance of 0 to 40 km from the radar) → TR → SR → VU

Appendix B

Major axis derived from Principal Component Analysis (PCA)

To objectively determine the orientation of a convection, the PCA method is applied. The calculation procedure is described as follows and illustrated in Fig. B.1.

First, grid points with reflectivity values exceeding a specified threshold are selected. The longitudes and latitudes of these selected grid points are stored in a 2-D array, where the first row corresponds to longitudes and the second row corresponds to latitudes. The mean longitude and latitude are then computed, and each coordinate is subtracted by its respective mean, a covariance matrix is then constructed. Finally, eigenvalue decomposition is performed on the covariance matrix, and the eigenvector associated with the largest eigenvalue is identified as the first principal component (PC1), which indicates the dominant orientation of the convection. The standard deviation is equal to the square root of the corresponding eigenvalue.

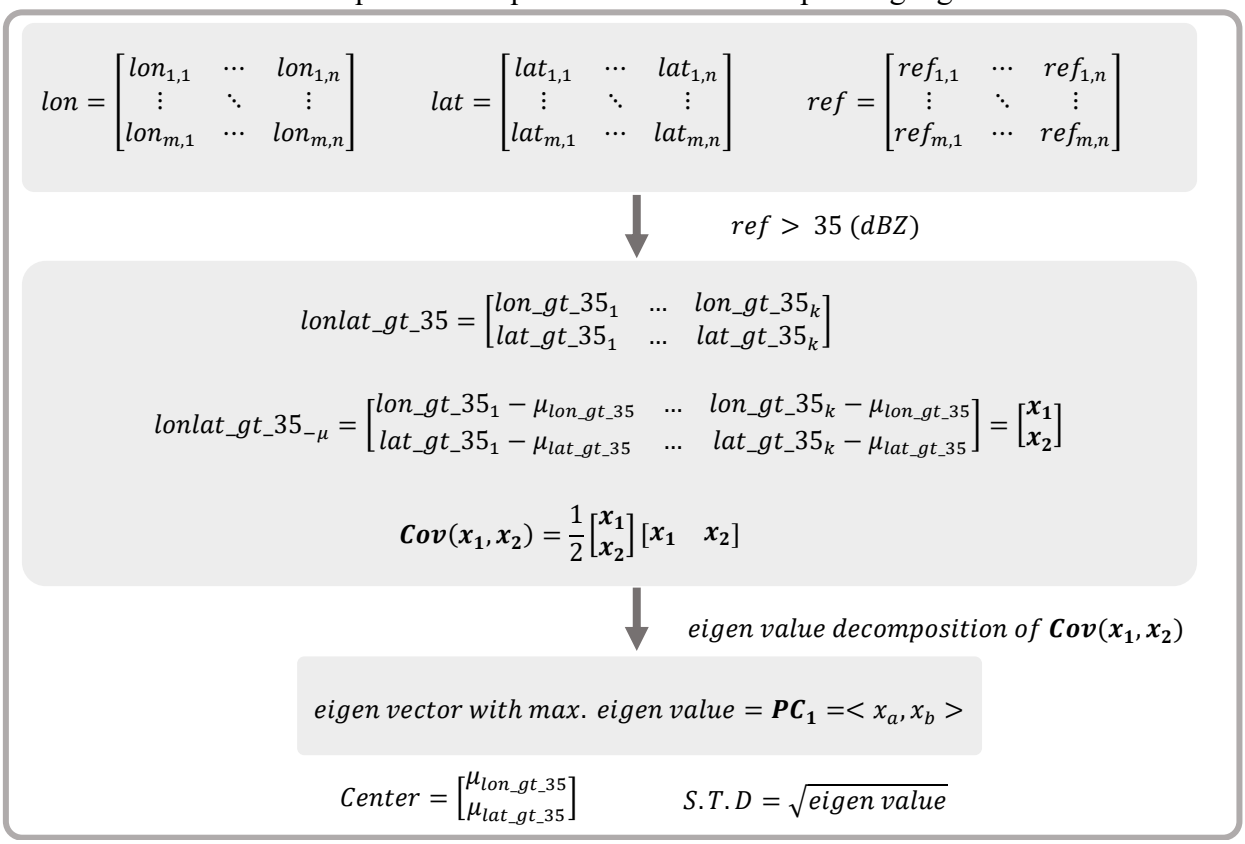

Figure B.1. The schematic illustrates the procedure for calculating the major axis using the PCA method. In this case, a reflectivity threshold of 35 dBZ is applied.

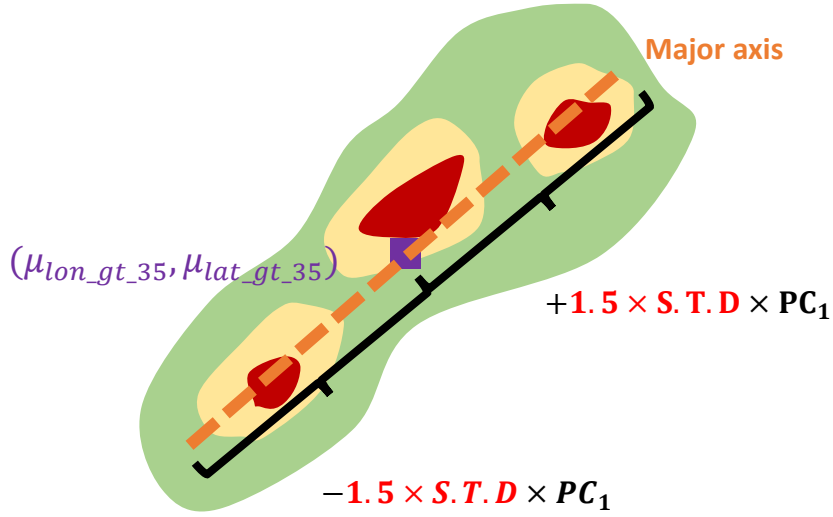

Figure B.2. Shaded colors green, yellow, and red represent reflectivity levels of 25, 35, and 45 dBZ, respectively. Purple square indicates the averaged location of longitude and latitude.

With the mean coordinates, standard deviation, and the PC1, the two endpoints of the major axis are obtained by adding and subtracting 1.5 times the standard deviation multiplied by PC1 to the mean longitude and latitude. A straight line connecting these two endpoints represents the orientation of the convective major axis, as illustrated in Fig. B.2.

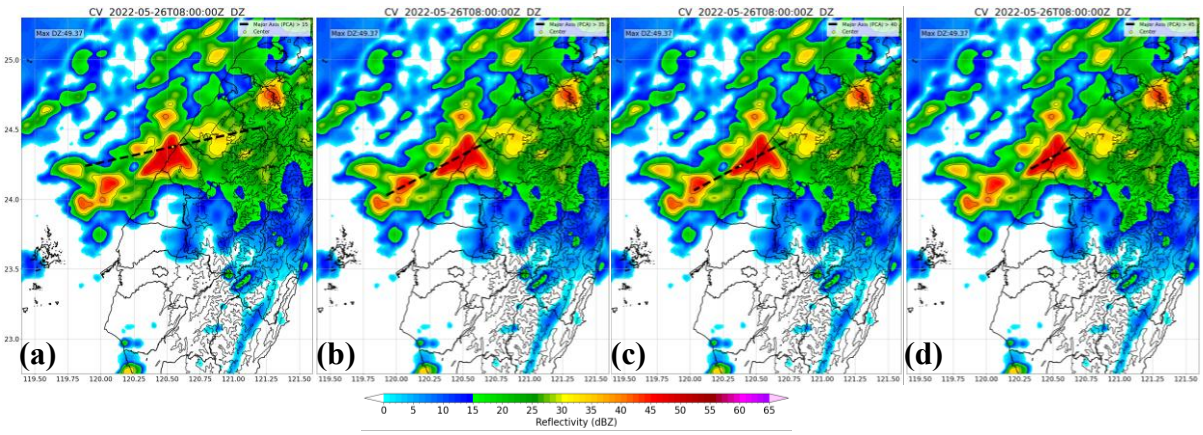

Figure B.3. Major axes corresponding to different thresholds are indicated by black dashed lines: (a) 30 dBZ, (b) 35 dBZ, (c) 40 dBZ, and (d) 45 dBZ. The contour lines represent the terrain. The contour lines represent terrain elevation, and the shading indicates reflectivity intensity.

As shown in Fig. B.3, three strong convectoins (> 40 dBZ) are located over central Taiwan, associated with wide-range stratiform regions. The major axes using thresholds of 35 and 40 dBZ could well capture the orientatoin of the convection of interset, as compared to those using

thresholds of 30 and 45 dBZ. Considering that the reflectivity derived using rainwater mixing ratio produced by IBM_VDRAS are usually underestimated in comparison with observations, we select the 30 dBZ to be the threshold in calculating the major axis of the convectoins in this study.

References

唐玉霜，2010: 2009 莫拉克颱風雷達觀測中尺度雨帶特性研究。國立中央大學大氣物理所碩士論文。[Tang, Y.-S., 2010: The mesoscale characteristics of rainband from radar analyses: typhoon Morakot(2009). *Master thesis, National Central University*.]

羅翊銓，2019：IBM_VDRAS系統功能的擴充與個案模擬- 以2017年7月7日午後對流為例。國立中央大學大氣物理所碩士論文。[Lo, Y.-C., 2019: The Extension of IBM_VDRAS System and Its Case Study-07/07/2017 Afternoon Thunderstorm Case. *Master thesis, National Central University*.]

陳如瑜、張偉裕、陳台琦（2017）。北台灣S與C波段雙偏極化雷達定量降雨估計之比較。大氣科學，45(1)，57-81。[Chen, J.-Y., W.-Y. Chang, and T.-C. Chen Wang, 2017: Comparison of Quantitative Precipitation Estimation in Northern Taiwan Using S- and C-band Dual-Polarimetric Radars. *Atmospheric Sciences,* **45(1)**, 57-81.]

繆炯恩、楊明仁（2018）。2015年6月14日台北盆地劇烈午後雷暴個案研究：對流胞合併機制與強降雨過程探討。大氣科學，46(4)，427-454。[Miao, J.-E., and M.-Y. Yang, 2017: Cell Merger and Heavy Rainfall of the Severe Afternoon Thunderstorm Event at Taipei on 14 June 2015. *Atmospheric Sciences,* **46(4)**, 427-454.]

Chang, S.-F., Y.-C. Liou, J. Sun, and S.-L. Tai, 2016: The Implementation of the Ice-Phase Microphysical Process into a Four-Dimensional Variational Doppler Radar Analysis System (VDRAS) and Its Impact on Parameter Retrieval and Quantitative Precipitation Nowcasting. *Journal of the Atmospheric Sciences*, **73**, 1015-1038.

Chappell, C. F., 1986: *Mesoscale Meteorology and Forecasting*. Boston, MA: American Meteorological Society, pp. 289-310.

Chen, G. T.-J., C.-C. Wang, and D. T.-W. Lin, 2005: Characteristics of Low-Level Jets over Northern Taiwan in Mei-Yu Season and Their Relationship to Heavy Rain Events. *Monthly Weather Review*, **133**, 20-43.

Chen, Y.-L., X. A. Chen, S. Chen, and Y.-H. Kuo, 1997: A Numerical Study of the Low-Level Jet during TAMEX IOP 5. *Monthly Weather Review*, **125**, 2583-2604.

Chen, Y.-L., X. A. Chen, and Y.-X. Zhang, 1994: A Diagnostic Study of the Low-Level Jet during TAMEX IOP 5. *Monthly Weather Review*, **122**, 2257-2284.

Chen, Y.-L., C.-C. Tu, F. Hsiao, C.-S. Chen, P.-L. Lin, and P.-H. Lin, 2022: An Overview of Low-Level Jets (LLJs) and Their Roles in Heavy Rainfall over the Taiwan Area during the Early Summer Rainy Season. *Meteorology*, **1**, 64-112.

Crook, N. A., and J. Sun, 2002: Assimilating Radar, Surface, and Profiler Data for the Sydney 2000 Forecast Demonstration Project. *Journal of Atmospheric and Oceanic Technology*, **19**, 888-898.

Crook, N. A., and J. Sun, 2004: Analysis and Forecasting of the Low-Level Wind during the

Sydney 2000 Forecast Demonstration Project. *Weather and Forecasting*, **19**, 151-167.

Doswell, C. A., H. E. Brooks, and R. A. Maddox, 1996: Flash Flood Forecasting: An Ingredients-Based Methodology. *Weather and Forecasting*, **11**, 560-581.

Franke, R., 1982: Scattered data interpolation: tests of some methods. *Mathematics of Computation*, **38**, 181-200.

Gao, T., Y.-H. Tseng, and X.-Y. Lu, 2007: An improved hybrid Cartesian/immersed boundary method for fluid–solid flows. *International Journal for Numerical Methods in Fluids*, **55**, 1189-1211.

Houze, R. A., B. F. Smull, and P. Dodge, 1990: Mesoscale Organization of Springtime Rainstorms in Oklahoma. *Monthly Weather Review*, **118**, 613-654.

Ito, J., H. Tsuguchi, S. Hayashi, and H. Niino, 2021: Idealized High-Resolution Simulations of a Back-Building Convective System that Causes Torrential Rain. *Journal of the Atmospheric Sciences*, **78**, 117-132.

Ke, C.-Y., C. Kao-Shen, C. W. Tai-Chi, and Y.-C. and Liou, 2019: Analysis of heavy rainfall and barrier-jet evolution during Mei-Yu season using multiple Doppler radar retrievals: a case study on 11 June 2012. *Tellus A: Dynamic Meteorology and Oceanography*, **71**, 1571369.

Kessler, E., 1969: *On the Distribution and Continuity of Water Substance in Atmospheric Circulations*. Boston, MA: American Meteorological Society, pp. 1-84.

Kuo, Y.-H., and G. T.-J. Chen, 1990: The Taiwan Area Mesoscale Experiment (TAMEX): An Overview. *Bulletin of the American Meteorological Society*, **71**, 488-503.

Li, J., and Y.-L. Chen, 1998: Barrier Jets during TAMEX. *Monthly Weather Review*, **126**, 959-971.

Miller, M. J., and R. P. Pearce, 1974: A three-dimensional primitive equation model of cumulonimbus convection. *Quarterly Journal of the Royal Meteorological Society*, **100**, 133-154.

Parker, M. D., and R. H. Johnson, 2000: Organizational Modes of Midlatitude Mesoscale Convective Systems. *Monthly Weather Review*, **128**, 3413-3436.

Parker, M. D., and R. H. Johnson, 2004: Structures and Dynamics of Quasi-2D Mesoscale Convective Systems. *Journal of the Atmospheric Sciences*, **61**, 545-567.

Ryzhkov, A. V., and D. S. Zrnic, 2019: Radar Polarimetry for Weather Observations. *Radar Polarimetry for Weather Observations*.

Schumacher, R. S., 2009: Mechanisms for Quasi-Stationary Behavior in Simulated Heavy-Rain-Producing Convective Systems. *Journal of the Atmospheric Sciences*, **66**, 1543-1568.

Schumacher, R. S., and R. H. Johnson, 2005: Organization and Environmental Properties of Extreme-Rain-Producing Mesoscale Convective Systems. *Monthly Weather Review*, **133**, 961-976.

Schumacher, R. S., and R. H. Johnson, 2008: Mesoscale Processes Contributing to Extreme Rainfall in a Midlatitude Warm-Season Flash Flood. *Monthly Weather Review*, **136**, 3964-3986.

Schumacher, R. S., and R. H. Johnson, 2009: Quasi-Stationary, Extreme-Rain-Producing Convective Systems Associated with Midlevel Cyclonic Circulations. *Weather and Forecasting*, **24**, 555-574.

Sun, J., 2005: Initialization and Numerical Forecasting of a Supercell Storm Observed during STEPS. *Monthly Weather Review*, **133**, 793-813.

Sun, J., and Y. Zhang, 2008: Analysis and Prediction of a Squall Line Observed during IHOP Using Multiple WSR-88D Observations. *Monthly Weather Review*, **136**, 2364-2388.

Sun, J. Z., and N. A. Crook, 1997: Dynamical and Microphysical Retrieval from Doppler Radar Observations Using a Cloud Model and Its Adjoint. Part I: Model Development and Simulated Data Experiments. *Journal of the Atmospheric Sciences*, **54**, 1642-1661.

Sun, J. Z., and N. A. Crook, 1998: Dynamical and Microphysical Retrieval from Doppler Radar Observations Using a Cloud Model and Its Adjoint. Part II: Retrieval Experiments of an Observed Florida Convective Storm. *Journal of the Atmospheric Sciences*, **55**, 835-852.

Sun, J. Z., R. M. Li, Q. H. Zhang, S. B. Trier, Z. M. Ying, and J. Xu, 2023: Mesoscale Factors Contributing to the Extreme Rainstorm on 20 July 2021 in Zhengzhou, China, as Revealed by Rapid Update 4DVar Analysis. *Monthly Weather Review*, **151**, 2153-2176.

Tai-Jen Chen, G., and C.-C. Yu, 1988: Study of Low-Level Jet and Extremely Heavy Rainfall over Northern Taiwan in the Mei-Yu Season. *Monthly Weather Review*, **116**, 884-891.

Tai, S.-L., Y.-C. Liou, J. Sun, and S.-F. Chang, 2017: The Development of a Terrain-Resolving Scheme for the Forward Model and Its Adjoint in the Four-Dimensional Variational Doppler Radar Analysis System (VDRAS). *Monthly Weather Review*, **145**, 289-306.

Tai, S.-L., Y.-C. Liou, J. Sun, S.-F. Chang, and M.-C. Kuo, 2011: Precipitation Forecasting Using Doppler Radar Data, a Cloud Model with Adjoint, and the Weather Research and Forecasting Model: Real Case Studies during SoWMEX in Taiwan. *Weather and Forecasting*, **26**, 975-992.

Tseng, Y.-H., and J. H. Ferziger, 2003: A ghost-cell immersed boundary method for flow in complex geometry. *Journal of Computational Physics*, **192**, 593-623.

Tu, C.-C., Y.-L. Chen, P.-L. Lin, and Y. Du, 2019: Characteristics of the Marine Boundary Layer Jet over the South China Sea during the Early Summer Rainy Season of Taiwan. *Monthly Weather Review*, **147**, 457-475.

Tu, C.-C., Y.-L. Chen, P.-L. Lin, and M.-Q. Huang, 2022: Analysis and Simulations of a Heavy Rainfall Event Associated with the Passage of a Shallow Front over Northern

Taiwan on 2 June 2017. *Monthly Weather Review*, **150**, 505-528.

Wang, C. C., B. K. Chiou, G. T. J. Chen, H. C. Kuo, and C. H. Liu, 2016: A numerical study of back-building process in a quasistationary rainband with extreme rainfall over northern Taiwan during 11–12 June 2012. *Atmos. Chem. Phys.*, **16**, 12359-12382.

Wang, C. C., P. Y. Chuang, S. T. Chen, D. I. Lee, and K. Tsuboki, 2022: Idealized simulations of Mei-yu rainfall in Taiwan under uniform southwesterly flow using a cloud-resolving model. *Nat. Hazards Earth Syst. Sci.*, **22**, 1795-1817.

Wu, Y.-J., Y.-C. Liou, Y.-C. Lo, S.-L. Tai, S.-F. Chang, and J. Sun, 2021: Precipitation Processes of a Thunderstorm Occurred on 19 August 2014 in Northern Taiwan Documented by Using a High Resolution 4DVar Data Assimilation System. *Journal of the Meteorological Society of Japan. Ser. II*, **99**, 1023-1044.

Xiao, X., J. Sun, L. Ji, L. Zhang, Z. Ying, Z. Chen, M. Chen, and C. Xu, 2022: A Study on Local-Scale Thermal and Dynamical Mechanisms in the Initiation of a Squall Line Under Weak Forcing. *Journal of Geophysical Research: Atmospheres*, **127**, e2021JD035561.

Yang, S.-C., S.-H. Chen, L. J.-Y. Liu, H.-L. Yeh, W.-Y. Chang, K.-S. Chung, P.-L. Chang, and W.-C. Lee, 2024: Investigating the Mechanisms of an Intense Coastal Rainfall Event during TAHOPE/PRECIP-IOP3 Using a Multiscale Radar Ensemble Data Assimilation System. *Monthly Weather Review*, **152**, 2545-2567.

Zhang, F., Q. Zhang, and J. Sun, 2021: Initiation of an Elevated Mesoscale Convective System With the Influence of Complex Terrain During Meiyu Season. *Journal of Geophysical Research: Atmospheres*, **126**, e2020JD033416.

Zhang, L., J. Sun, Z. Ying, and X. Xiao, 2021: Initiation and Development of a Squall Line Crossing Hangzhou Bay. *Journal of Geophysical Research: Atmospheres*, **126**, e2020JD032504.